I. THE CARACAS, VENEZUELA EARTHQUAKE OF 1967: A MULTIPLE SOURCE EVENT

II. SEISMIC WAVES AT THE EPICENTER'S ANTIPODE

Thesis by

José Antonio Rial M.

In Partial Fulfillment of the Requirements

For the Degree of

Doctor of Philosophy

California Institute of Technology

Pasadena, California

1979

(Submitted December 18, 1978)

ACKNOWLEDGMENTS

I owe the Consejo de Desarrollo Científico y Humanístico of the Universidad Central de Venezuela, Caracas, for all five years I have spent doing my graduate work. I have never been professionally so satisfied as during my stay at Caltech's Seismological Laboratory. D. Helmberger has been my guide and dear friend, for whom I feel a profound admiration and respect, not only for his scientific stature, but for his even taller humanism. Seismo Lab people were most exceedingly helpful at all times; I am grateful to all of them. I must acknowledge the inspiring discussions with D. Harkrider, D. Anderson, H. Kanamori, L. Ruff, V. Cormier, their advice and encouragement.

I deeply regret having to leave, and deep inside I am sure that this is not goodbye.

This research was partially supported by National Science Foundation grants EAR76-06619 and EAR78-14786.

GENERAL INTRODUCTION

This dissertation consists of two unrelated subjects. Although both deal with the construction of synthetic seismograms, the first (Chapter I) is the detailed study of a complicated earthquake source, whereas the second (Chapter II) deals with the structure of the earth's interior as seen from the antipode of a seismic wave source. The two can be classified as problems involving forward inversion of seismological data. There is, however, a significant common ground in the spirit of the approach in the sense that seismic wave interference phenomena, present in both, are used as allies in reducing the inherent non-uniqueness of the inversion process.

TABLE OF CONTENTS

CHAPTER I

The Caracas, Venezuela earthquake of 1967: A multiple source event.

ABSTRACT

A general study of Caribbean plate tectonics is first focused on the determination of fault parameters and source processes of the Caracas (Venezuela) earthquake of July 29, 1967 (m_b = 6.5, M_s = 6.7). Synthetic seismograms which closely reproduce the observed P-, SH- and Love wave seismograms were generated using generalized ray and mode theory, respectively. The results indicate a complicated faulting process, consisting of at least three separated sources aligned along a N10W-trending "en echelon" vertical left-lateral strike-slip system of three faults that ruptured from north to south, at three discrete places with an extreme separation of 90 km. The process of rupture progressed southwards with a mean velocity of 3 km/sec. The focal depths of the individual sources varied between 8 km and 27.5 km. The total dislocation was calculated as 120 cm along the direction N10W and the total average moment as 4×10^{26} dyne-cm. The multiple character of the event severely constrains the number of suitable source models that can be inferred, thus facilitating the process of inversion. Tectonic implications are briefly discussed and local geology is successfully invoked to support the source model.

I.1 INTRODUCTION

Studies on Caribbean seismotectonics are not numerous, and in general are limited to a descriptive account of seismicity, fault plane solutions or seismic-wave transmission [Sykes and Ewing, 1965; Molnar and Oliver, 1969; Molnar and Sykes, 1969; Papazachos, 1964; Tarr, 1968; Rial, 1976a,b]. In the last twenty years several major earthquakes, with surface wave magnitudes 6.5 and larger, have occurred along the eastern Caribbean seismic loop from S. Domingo to Colombia (Figure I.1). It is the purpose of this and subsequent studies to investigate in detail the focal processes, source parameters and tectonic significance of selected events of this group in the hope of obtaining a clearer picture of the seismic energy release style that characterizes the Carribean plate boundaries.

In this paper one seismic event of critical importance is analyzed in detail, the Caracas (Venezuela) earthquake of July 29, 1967 ($m_b = 6.5$, $M_s = 6.7$) which occurred on the proposed southern boundary of the plate in a region where great earthquakes of magnitude over 8 have occurred in the past [Gutenberg and Richter, 1954] and in which seismic hazards are continually increasing because of growing population and industrial expansion.

The present analysis of this event is based primarily on teleseismic records of long-period body and long- and short-period surface waves. No near-field data, including accurate aftershock locations, are available. The only seismological station in the region (CAR) recorded most aftershocks on a short-period vertical instrument, the only one left in

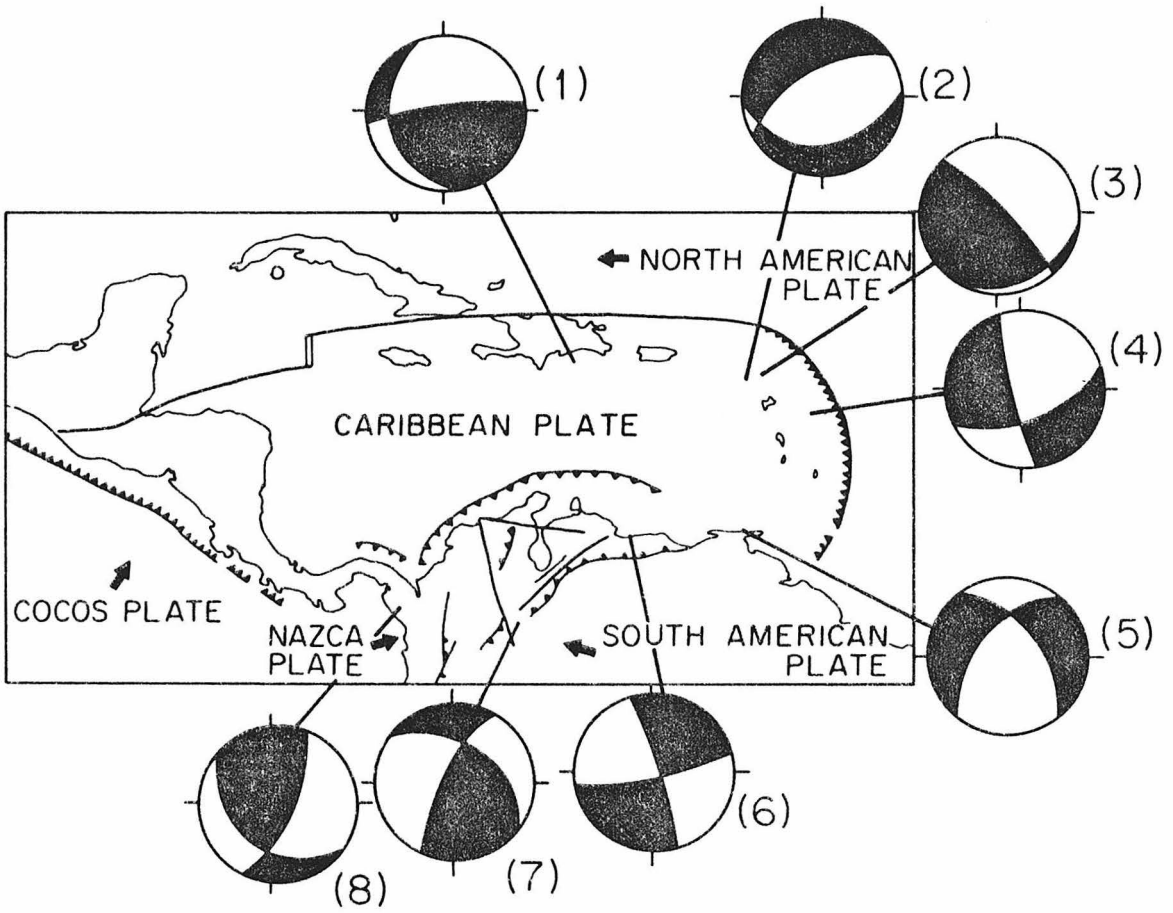

Fig. I.1 Focal mechanisms of large earthquakes along the Caribbean plate boundaries (shaded areas are compressional first motions).

1: June 11, 1971 H = 12h 56m Ms = 6.5
2: October 8, 1974 H = 09h 50m Ms = 7.1
3: December 24, 1967 H = 20h 03m Ms = 6.7
4: December 25, 1969 H = 21h 32m Ms = 7.2
5: June 12, 1974 H = 16h 25 m Ms = 6.5
6: July 30, 1967 H = 00h 00m Ms = 6.7, the Caracas earthquake
7: July 29, 1967 H = 10h 24m Ms = 6.2
8: July 13, 1974 H = 01h 18m Ms = 7.2

working condition after the main shock, whose epicenter was located 60 km to the NW of the station under the ocean [Fiedler, 1968].

The fault plane solution for the Caracas event (Figure I.2) based on first P-wave arrivals shows a typical double couple strike-slip radiation pattern with two nodal planes oriented N10W and N80E with vertical and nearly vertical dips. The closeness of the epicenter to the major east-west tectonic lineaments of northern Venezuela made Molnar and Sykes [1969] suggest the N80E plane as representing the right-lateral earthquake fault. The evidence here presented, however, shows that the rupture occurred along the N10W left-lateral strike-slip fault that ruptured from northwest to southeast in at least three separated places. The rupture process spread southward with a mean velocity of 3 km/s.

I.2 METHOD OF ANALYSIS

The determination of the source parameters for the Caracas earthquake was carried out by fitting the observed P-, SH-, and Love wave (G1) seismograms with computer synthesized ones corresponding to physically possible models. The Cagniard-deHoop formalism and generalized ray theory [Helmberger, 1974; Langston and Helmberger, 1975] are used in the construction of the body wave synthetics; the method of Harkrider [1964] is used in the generation of short-period surface wave synthetics. Finally, the directivity function defined by Ben-Menahem [1961] is calculated and compared with that observed for G2 waves recorded at stations symmetrically located with respect to the epicenter.

One major problem in the construction of synthetic seismograms is uniqueness. No matter how perfect the fits one can accomplish by

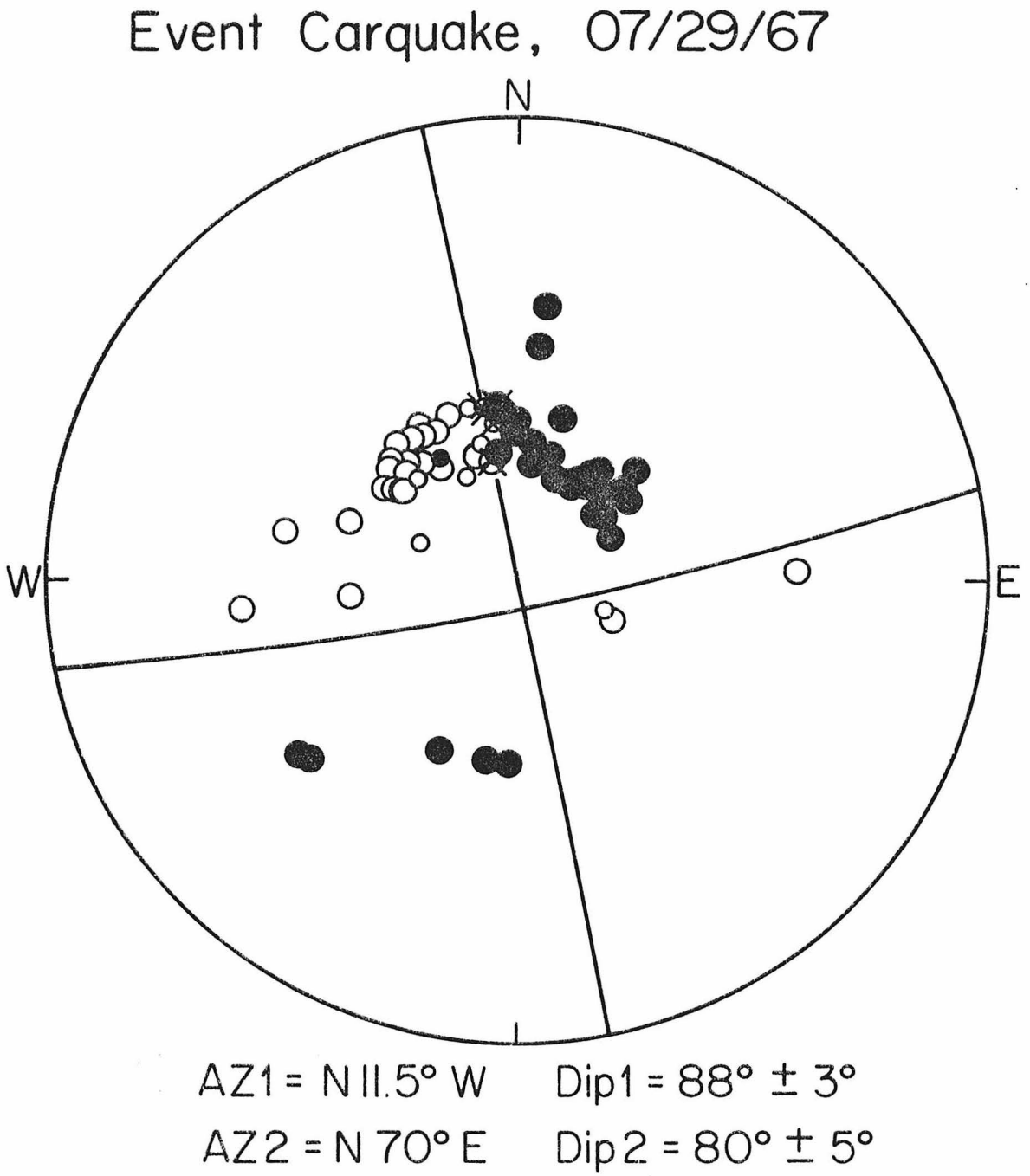

Fig. I.2 Fault-plane solution for the Caracas 1967 event from P-wave first arrivals. Open circles are dilatation, filled circles are compression.

patiently and diligently modifying the initial source model on a trial and error basis, the final model is good because it fits the data, not because it represents the physics of the source process uniquely. It is therefore quite important to look for characteristics in the whole radiated wave field that make the number of physically plausible models decrease to a minimum. Unfortunately, there are no general rules to search for uniqueness other than to hope that the source process itself contains easily identifiable (unique) characteristics. In the process of fitting the generated seismograms many parameters are involved, thus it is also desirable to check the resulting models using P-, S-, and surface waves as independent constraints. In this study long-period body waves and short- and long-period surface waves recorded at WWSSN stations have been used in the analysis. When necessary, individual phases have been digitized and rotated to separate the components of the ground motion.

I.3 BODY WAVES

P-Waves

One important feature of the Caracas earthquake is that its P-wave train indicates a multiple source (see Figure I.3). A close waveform inspection shows that for many stations the first P onset appears identical to a synthetic P-wave for a strike-slip event of focal depth between 12 and 14 km as recorded by a WWSSN station at teleseismic range as shown by Helmberger [1974]. The three initial phases (first 10 s) can thus be identified as the sequence P, pP, sP. The remarkable fact is that the trio repeats itself after about 16 s from the initial P onset, and

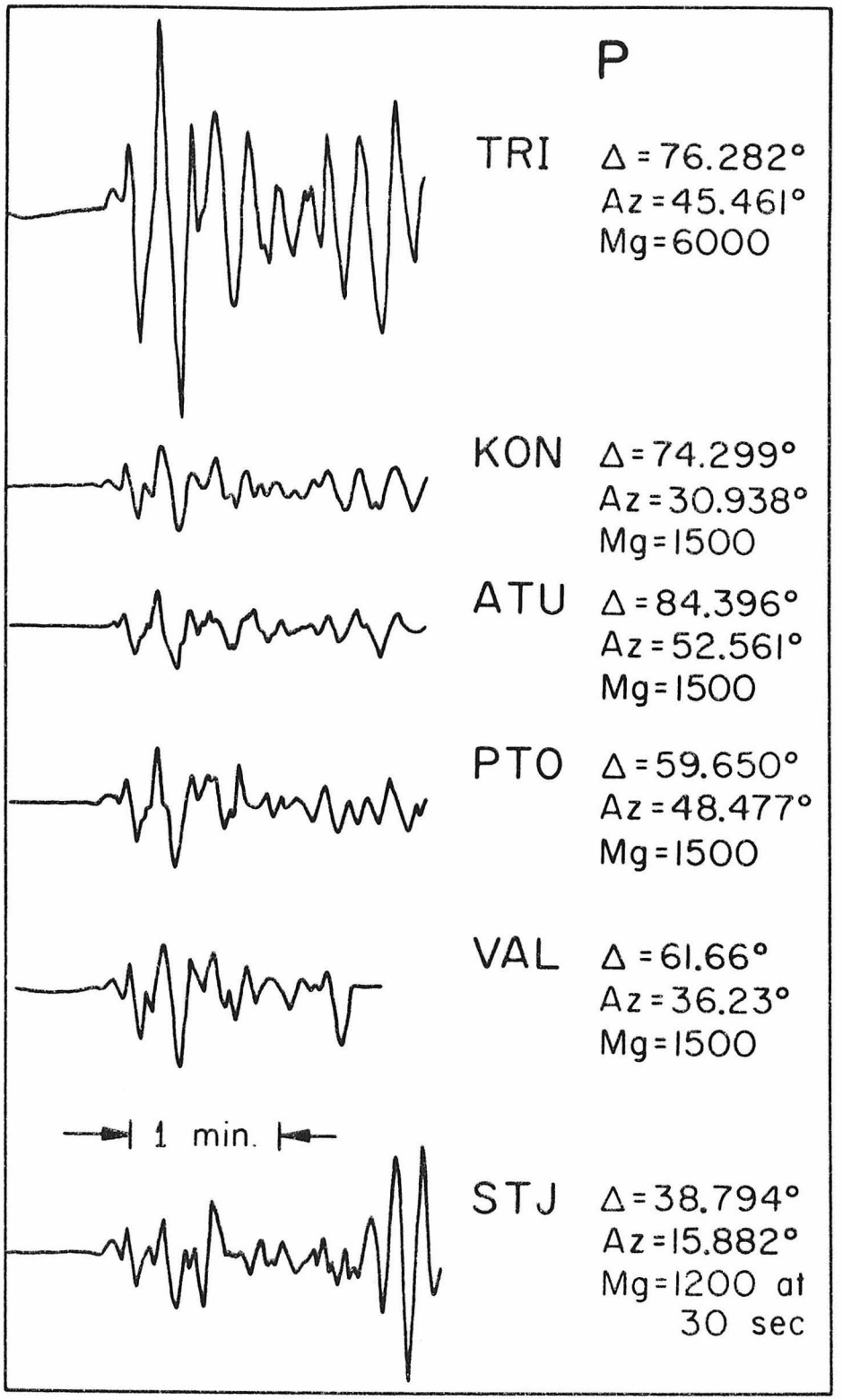

Fig. I.3 P-waves of the Caracas earthquake at several WWSSN stations

possibly again 17 s after the latter. This is most clearly seen at stations STJ, KON, and VAL (Figure I.3). After several records around the epicenter are compared, it is concluded that at least three similar sources, separated in space and time, must account for the waveforms seen. It will be shown that this multiplicity is an important factor in the previously mentioned search for uniqueness.

Body Wave Synthetic Seismograms

By using generalized ray theory and the Cagniard-deHoop formulation, the construction of synthetic seismograms is straightforward [see Langston and Helmberger, 1975]. In the present case of a triple source three seismograms lagged in space and time are constructed, each with its independent focal parameters, and then summed in the time domain. Thus for P-waves the final seismogram W(t) of the multiple shock can be represented by the expression

$$W(t) = \sum_{i=1}^{3} \omega_i(t)\, H(t-T_i) \tag{1}$$

where each $\omega_i(t)$ is the total vertical response at the far field receiver for each double couple point source, T_i are the corresponding origin time lags, H is the Heaviside step function, and

$$\omega_i(t) = R_{pz}[\dot{\phi}_i + R_{pp}\dot{\phi}_i H(t-\Delta t_1) + (R_{sp}\frac{\eta_\alpha}{\eta_\beta})\,\dot{\Omega}_i H(t-t_2)] * S(t) * I(t) * Q(t) \tag{2}$$

where the asterisks are convolution operators. The terms in brackets in (2) represent, respectively, the direct P-wave, the pP phase, and sP phase contributions to the seismogram. These terms can be visualized as the

surface-source interaction near the epicenter. R_{pz} is the receiver function (P-wave, z component) defined in Helmberger [1974]. S(t) is the far-field source time function, taken here as a trapezoid of unit area for each event, and defined by three parameters δ_1, δ_2, δ_3 which represent the rise time, rupture time, and the roll-off time histories at the source as seen at the receiver. Each trapezoid then represents the source directivity for each individual event. This directivity thus defined does not appreciably change with azimuth [Burdick and Mellman, 1976], making it necessary to appropriately modify the δ's in the case of observed azimuthally dependent directivity. Q(t) and I(t) are the Q operator [Futterman, 1962] and the instrument response respectively, R_{pp} and R_{sp} are the reflection coefficients for pP and sP respectively, t_1 and t_2 are the corresponding lags with respect to the direct P-wave, and H is the Heaviside step function. p is the usual ray parameter and $\eta_v = (1/v^2-p^2)^{1/2}$ where v is either P- or S-wave velocity. Here $\dot{\phi}$ and $\dot{\Omega}$ are the time derivatives of the P- and SV-wave potentials, respectively. For S-wave seismograms equations (1) and (2) are simply transformed by substituting in the required S-wave potentials, coefficients, time responses, and time lags.

The Three Sources

The focal mechanism for the first event is known (Figure I.2). Two three-point source models representing three consecutive seismic events separated in space and time and oriented along each of the two nodal planes were tested. In each case a preliminary timing of the individual events was determined from stations located along great circles perpendicular. to each nodal plane. One of the two sets of event-times represents

the absolute timing of the events and therefore is the most important constraint at this stage in resolving the earthquake fault plane from the nodal plane. Of the two tested models, each with a different set of event times as initial conditions, only one will hopefully satisfy them and at the same time will closely reproduce the sixteen observed seismograms. It is indeed assumed throughout this stage that the three events are aligned along or are closely parallel to one of the two nodal planes on Figure I.2. There are perhaps several justifications to assume this, but the most obvious one stems from the observed similarity in waveforms from one event to the other, independent of azimuth and distance. This coherence suggests common focal geometry and this in turn suggests common tectonic origin.

The near source structure was assumed as a simple layer over half-space, as suggested by Burdick and Langston [1977] for the Caracas region. The crustal layer is 33 km thick and a sharp transition in P- and S-wave velocities exists between crust and mantle (6.28 km/s/8.1 km/s for P-waves 3.70 km/sec / 4.68 km/s for S-waves).

The best fits thus obtained are shown in Figure I.4 with the following source parameters:

I) Far Field Source Time History (Trapezoid)

	δ_1 (s)	δ_2 (s)	δ_3 (s)	Strength
Source 1	4.0	2.0	2.	1.
Source 2	4.0	2.0	2.	2.
Source 3	3.0	2.0	2.	2.

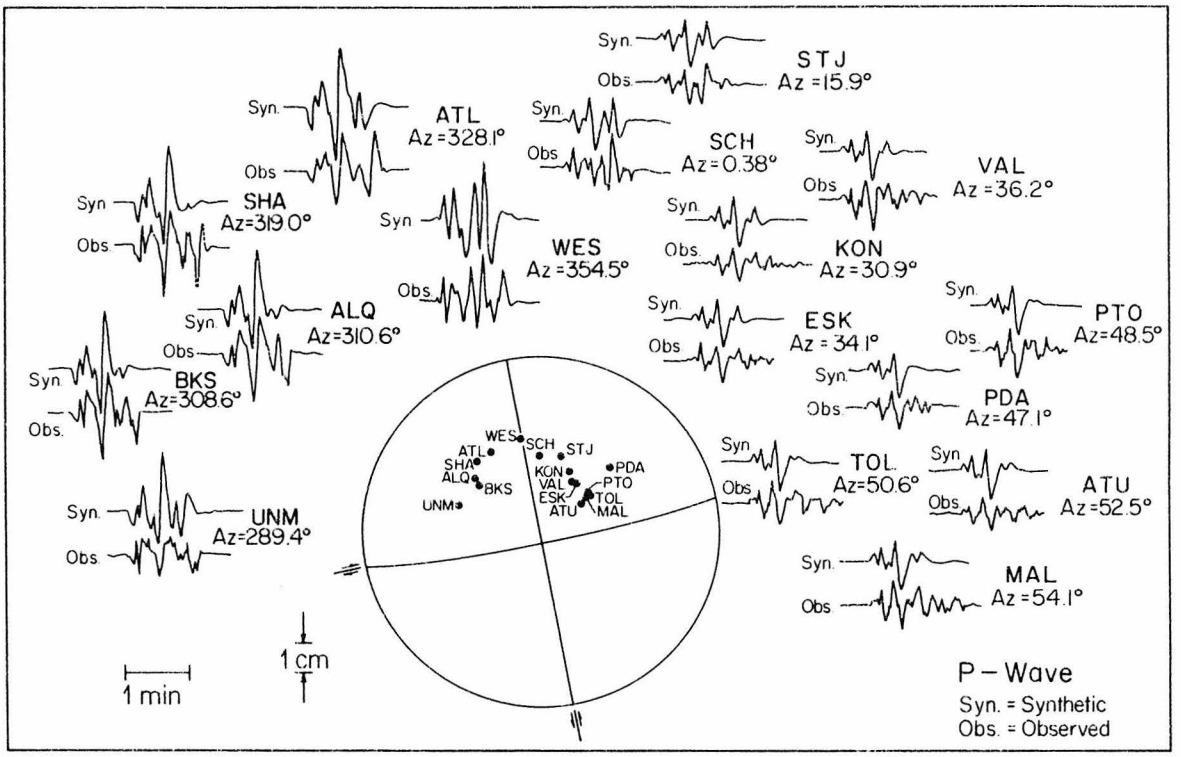

Fig. I.4 Comparison of observed and synthetic P-wave seismograms at WWSSN stations around the epicenter.

II) Time of Occurrence and Relative Locations

(X is measured in km from the first source along the fault trace. Y is measured in km perpendicularly. South is negative, East is positive.)

	Time (s)	X (km)	Y (km)	Focal Depth (km)
Source 1	0.	0.	0.	13.
Source 2	12.	-52.	25.	10.
Source 3	32.	-90.	40.	25

III) Fault Plane Solutions

(Azimuth is measured clockwise from North to the fault trace such as to define the sense of the movement of the hanging block, i.e., the reference direction of rake. See Langston and Helmberger [1975].)

	Fault Azimuth (deg)	Dip (deg)	Rake (deg)
Source 1	350	87.	0.
Source 2	350	87.	0.
Source 3	340	89.	0.

The stability of these results is good, in that small changes in fault dip, timing, or relative epicenter location (a few degrees, seconds, kilometers) can make the difference between a good fit (all stations) and a partial fit (some stations only). However, there certainly may be other combinations of parameters that, without substantially changing the picture, could produce equally good fits to the data. Our task is to make use of as many independent data as possible in order to reduce the

number of other combinations. Figure 4 shows that the above set of parameters reproduces fairly well the observed seismograms. Unfortunately, the P-waves at South American stations are not available in the distance range required ($30° \leq \Delta \leq 90°$) for P-wave arrival times coincided with the stations change of record period. Thus the model obtained may also be biased, especially latitude-wise.

The best fits (Figure I.4) require that:

(1) The first and last events have an extreme separation of about 97 km.

(2) The three shocks occurred on three parallel faults of a seemingly "en echelon" left lateral strike-slip system oriented N10W, (S10E) with the northernmost event occurring first.

(3) The sequence of events propagated south with a mean velocity close to 3 km/sec; the overall process of fracture is completed in 37 s.

(4) In propagating south the focal depth first decreased and then increased.

(5) The three sources had comparable strength, the second and third events being double in amplitude relative to the first.

A total average moment, $\overline{M}_0$, of 5.0×10^{26} dyne-cm is obtained by comparing sP amplitudes of synthetic and observed seismograms. The individual events have average moments of 1.2, 2.0, and 2×10^{26} dyne-cm. $T/\overline{Q}_\alpha = 1.1$ was used, where T is P-wave travel time and $\bar{Q}_\alpha$ is the path average quality factor for P-waves. Figure I.5 shows schematically the source model and the generalized rays included in the calculation of the synthetic seismograms. Each source generates one direct ray and two reflected rays with similar teleseismic travel times. No crustal

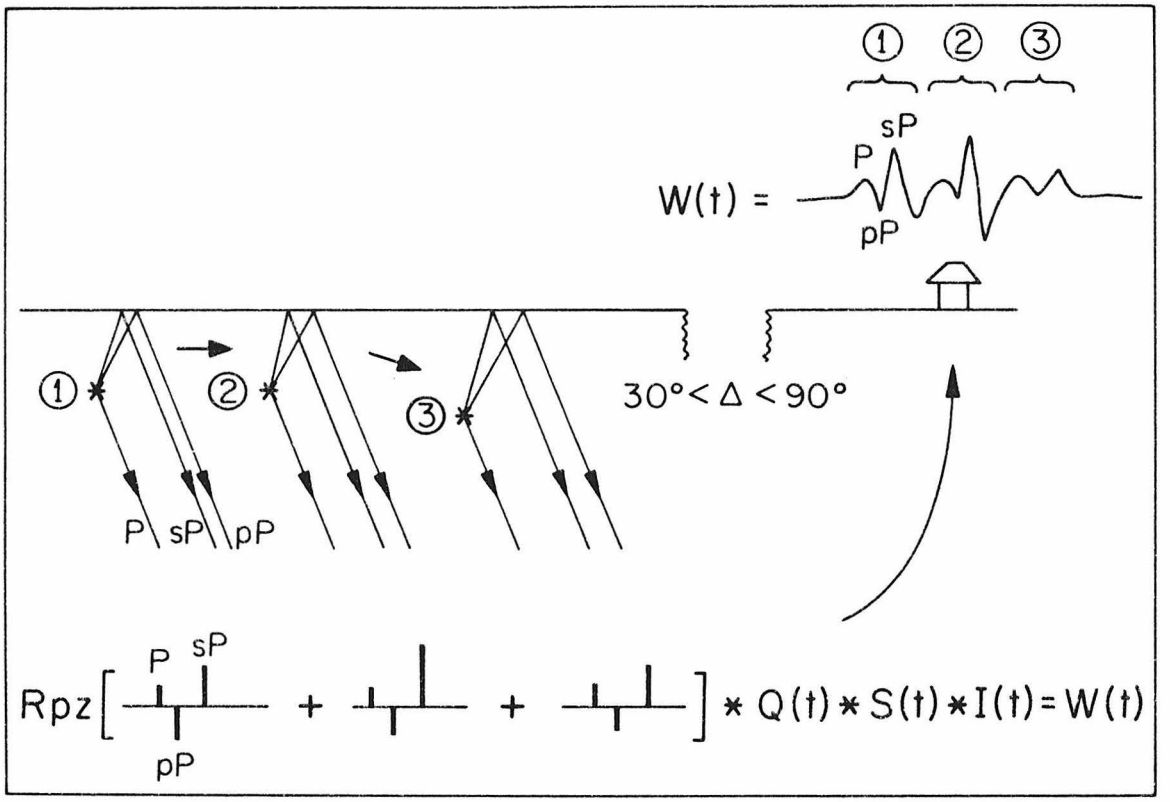

Fig. I.5 Interpretation of the focal process that generated the seismograms on Figures I.3 and I.4

reverberations were considered. The sequence of the three events was indeed such that the three trios of phases did not interfere strongly, thus providing the clue to the multiplicity of the event, facilitating the individual identification of phases. It shall be shown that stronger interference occurs, however, for the slower SH-waves, and this in turn helps considerably in the assessment of a more unique solution. In this regard P- and S-waves complement each other nicely in the process of inversion.

SH-Waves

Starting with the model already described for P-waves, SH-wave synthetic seismograms for ten WWSSN stations suitably located around the epicenter were generated. Only a few small changes in the parameters were necessary to obtain the rather remarkable fits shown in Figure I.6. This time two South American stations, ARE and LPA, provided excellent constraints, thus restricting the number of physically plausible models. It should be clear from Figure I.6 that the spatio-temporal sequence of events needed to fit all ten stations must now account for the rather obvious north-south asymmetry in wave forms observed when seismograms from CMC, SFA, or STJ, say, are compared with those recorded at LPA or ARE. Such asymmetry is best seen in detail in Figure I.7 for stations CMC and LPA, which are located within 5 degrees of the postulated direction of rupture propagation, on opposite sides of it. A simple calculation can be performed to determine the relative distance between events 1 and 2 from the relative arrivals of event 2 at CMC and LPA with respect to event 1. It is easy to show that this distance, ΔL, may be determined

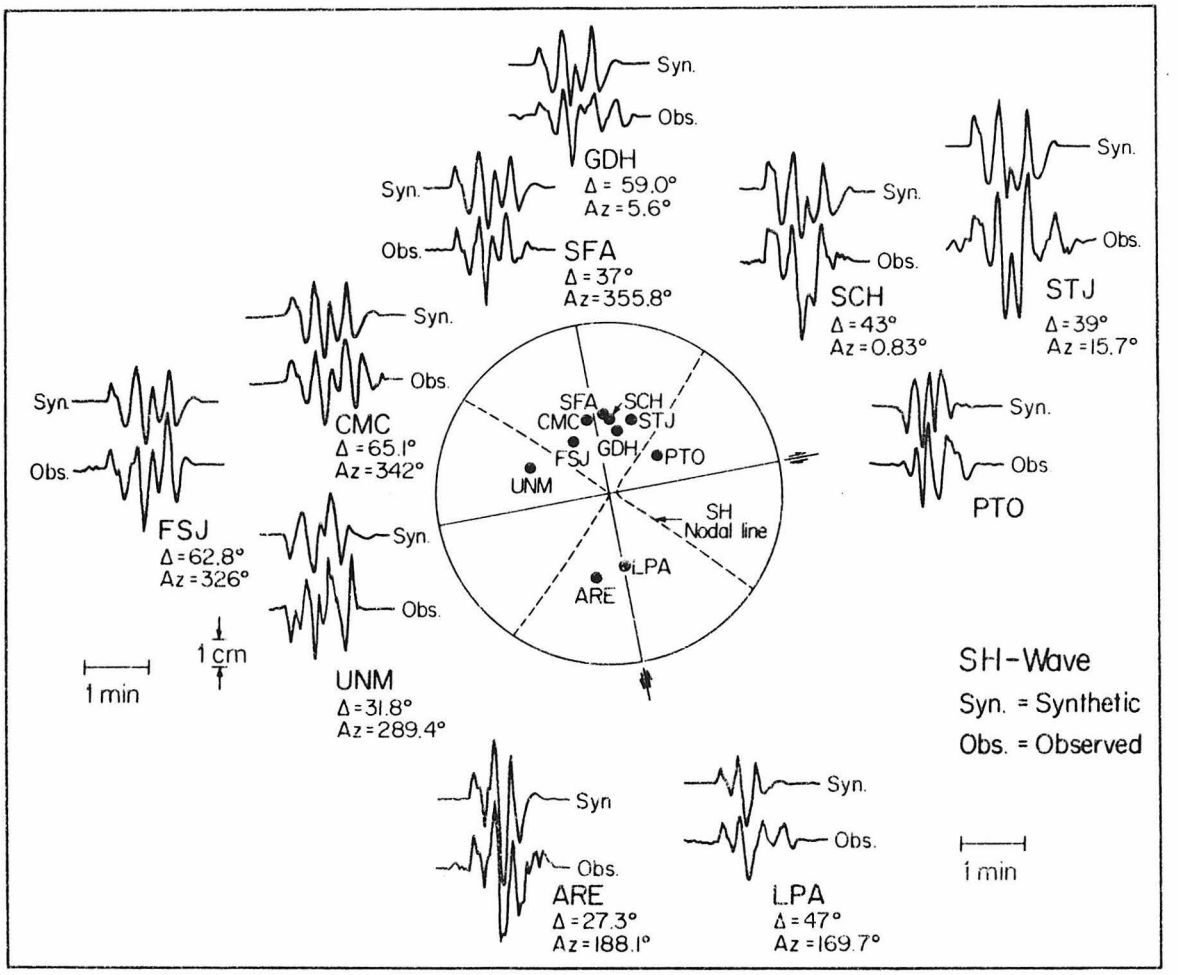

Fig. I.6 Comparison of observed and synthetic SH-wave seismograms at WWSSN stations around the epicenter. Notice the directivity effect between CMC, STJ to the north, and ARE, LPA to the south of the epicenter.

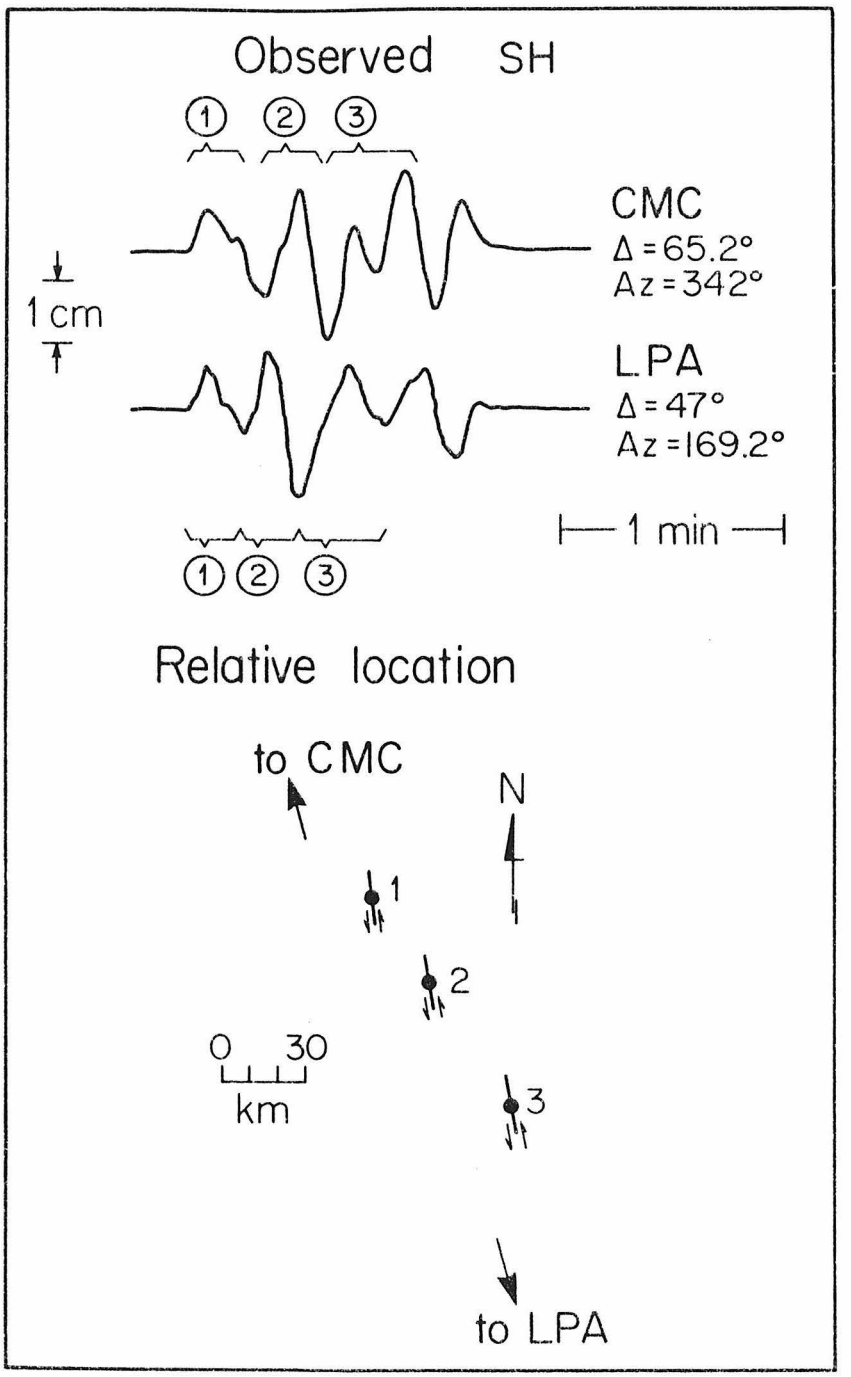

Fig. I.7 Comparison of observed seismograms at stations CMC and LPA. Notice the effect of source locations on the relative arrivals of events 1, 2, and 3 at LPA.

from the equation

$$\Delta L = \frac{\Delta^2 t}{P_{CMC} + P_{LPA}} \quad ; \quad \Delta^2 t = (t_2 - t_1)_{CMC} - (t_2 - t_1)_{LPA} \qquad (3)$$

where t_2 and t_1 are the arrival times of events 2 and 1, respectively, and P_{CMC} and P_{LPA} are the S-wave ray parameters at CMC and LPA, respectively. It is assumed that the two stations are just along the direction of the rupture, which progresses horizontally. With $\Delta^2 t = 8$ s obtained directly from the seismograms (Figure I.7) and $P_{CMC} = 0.10$, $P_{LPA} = 0.12$, we get

$$\Delta L = 36.4 \text{ km}$$

That is, the second event occurred 36.4 km to the southeast of the first, along the great circle between CMC and LPA. This result does not depend on the absolute times at which each event happened so it provides a very effective constraint on the basis of which several parameters can be fixed. In generating the SH-wave seismograms, however, this fact had been ignored; a new model was obtained by just adjusting the model previously determined for P-waves to fit the SH seismograms. The corrected new parameters were found to be:

IV) Corrected Source Parameters Using SH-Wave Seismograms

	Time (s)	X (km)	Y (km)	Focal Depth (km)
Source 1	0.	0.	0.	13.5
Source 2	15.	-30.	20.	8.0
Source 3	33.	-75.	50.	27.5

The total average moment, $\overline{M}_0$ for SH-waves is 3.0 x 10^{26}dyne-cm. The average moments for the individual events are 0.64, 1.02, and 1.3 x 10^{26}dyne-cm. This model is depicted in Figure I.7. Other parameters remain essentially the same as before. The most significant changes are that the second and third sources are now set to the north of their previous locations, making the extreme distance between sources 1 and 3 decrease to 90 km. This is indeed a direct result of the constraints imposed by the seismograms at LPA and ARE. For this model ΔL of equation (3) is seen to be 36.0 km, which agrees quite well with the above estimate. The changes in focal depth reflect the higher sensitivity of S-waves to this parameter. None of these changes affects substantially the fits shown previously on Figure I.4.

In Figure I.8 it is shown how the synthetic seismograms are constructed from three distinct point sources and how the interference of their phases (S and sS) produces the final synthetic waveform. In contrast with the P-wave seismograms, the SH slower velocity makes it possible for reflected and direct phases from two consecutive events to strongly interfere, thus producing a unique pattern which is azimuth dependent. This fact makes itself evident in the process of generating the synthetic seismograms, since parameters related to the spatio-temporal sequence of events become crucially important. As at each individual station a quite unique interference pattern appears, the closer all these patterns can be reproduced synthetically the closer the final model will be to uniqueness.

At this stage it is necessary to point out the fact that at station LPA a rather conflicting phase (dotted in Figure I.9) arrives just after the third event. This wave, however, is not an SH-wave. The particle

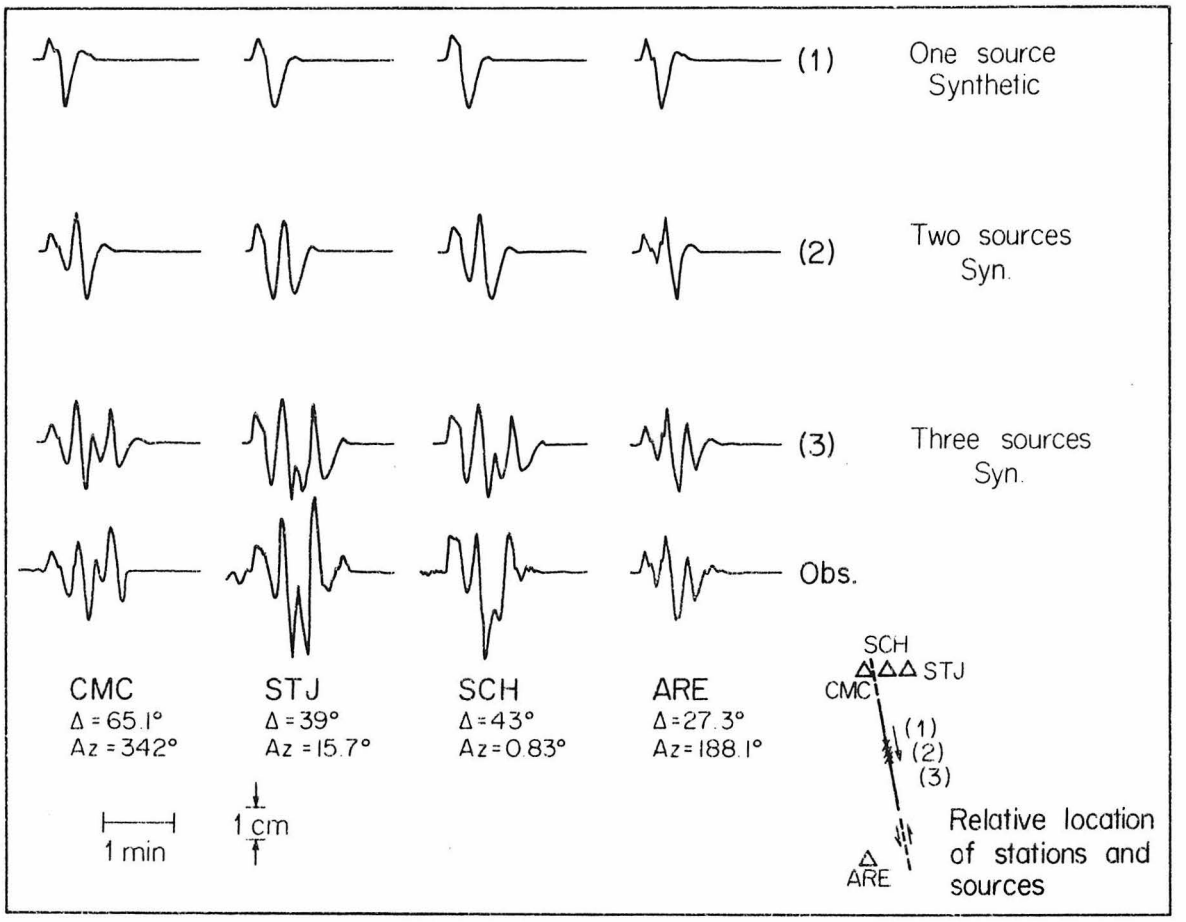

Fig. I.8 Synthetic SH waveforms for 1, 2, and 3 sources compared to selected observed seismograms. Notice the variation in interference patterns that develop in moving from northern stations CMC to STJ.

motion for this phase describes a prograde vertical ellipse, characteristic of an S-coupled PL-wave. As the phase arrives at LPA along a nongreat-circle path, its effect cannot be separated by rotation of the horizontal components, so it appears on the rotated SH seismograms of Figure I.9. The fact that a similar phase is not observed at ARE supports this interpretation.

The SH-wave seismograms have produced complementary evidence to the process of inversion. Nevertheless, there are ambiguities in the model that must be resolved. First, it is necessary to prove that the observed wave forms could have not been the result of radiation from a single fault, with a bilateral component of rupture. This indeed would produce a complex, multiple-like time function due to the extra stopping phase, thus creating the illusion of multiplicity. Various reasonable bilateral-rupture models on single faults were tried. No one could reproduce the wave forms as well as the multiple event model (see Figure I.9). Second, it is appropriate to further establish that the choice of fault planes in the direction N10W is the correct one. In Figure I.9 a refined model of the source that includes three propagating ruptures along N10W striking faults is compared with the observed seismograms at CMC and LPA. Here it is obvious that the relative duration of the first event at the two stations is well reproduced by the synthetics. The observed difference in time duration can thus be explained as a Doppler-type effect caused by a signal that propagates toward one of the stations (LPA) and away from the other. The small bilateral component shown in the model is necessary, although it may not be indispensable to achieve the best fit.

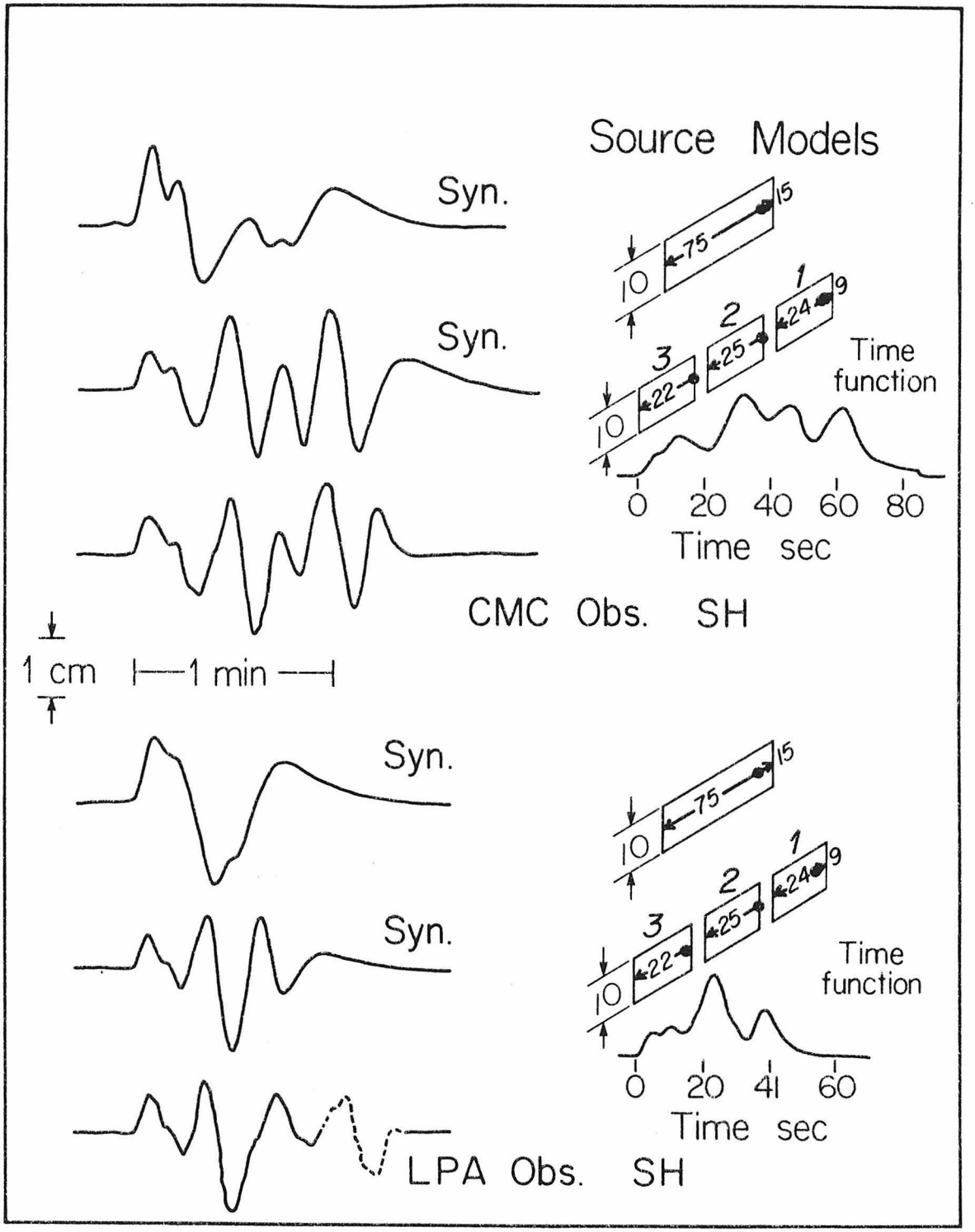

Fig. I.9 One fault source models and three fault source models for stations CMC and LPA. The dotted part of the signal at LPA is an S-coupled PL phase, not an SH phase.

The source model is now complete enough to establish the sense and direction of the rupture propagation and the fault orientation for the first event. The location and time of arrival of the second shock are reasonably well established by independent methods, and its wave form is satisfactorily reproduced in Figure I.9 by considering a 25 km long unilateral fracture propagating S10°E. As for the third event, its location and time of arrival are reasonably well established and its wave form reproduced satisfactorily by a 22 km long unilateral fracture also propagating S10°E.

Table 1 summarizes the best model obtained in generating the body wave synthetics for the Caracas 1967 earthquake. (See also Figure I.10.)

I.4 SURFACE WAVES

Synthetic Seismograms

A check on the longer period, average characteristics of the model proposed can be accomplished by generating surface waves with predominant periods between 15 and 90 s using the appropriate set of source parameters. For this purpose five records of Love (G1) waves were selected on the basis of quality and path simplicity. The comparison between synthetic and observed seismograms is shown in Figure I.11, along with the calculated values of the moment M_0 in each case. For the construction of the synthetic seismograms the theory given in Harkrider [1964] was used as it is now implemented on an interactive routine procedure for a NOVA 1200 minicomputer at the Seismological Laboratory, Caltech. The source time function was assumed triangular with an area equivalent to the sum of the three individual trapezoids previously described. To account for

TABLE 1

CARACAS 1967 EARTHQUAKE SOURCE PARAMETERS

Epicenter: 11°.0 N, 67°.25 W*	Source 1	Source 2	Source 3
1. Relative location (X,Y in km)	0., 0.,	-30., 20.	-75., 50.
2. Relative separation			
From Source 1 in km	0.	36.	90.
From Source 1 in sec	0.	15.	33.
3. Fault parameters			
Strike (°)	350	350	350
Dip (°)	87	87	87
Rake (°)	0.	0.	0.
Length (km)	33.	25.	22.
Width (km)	10.	10.	10.
Focal depth (km)	13.5	8.	27.5
4. Rupture parameters			
Rise time (sec)	2.5 (†)	2.5	2.5
Rupture vel. (km/sec)	3.5	3.0	3.0
Sense of rupture	S10E, N10W	S10E	S10E
Mode	bilateral	unilateral	unilateral
5. Avg. Moment ($\overline{M}_0$) ($\times 10^{26}$ dyne-cm)			
P-wave	1.0	2.0	2.0
S-wave	0.6	1.02	1.34

(†) 0.8 at LPA and ARE

(*) Fiedler [1968]

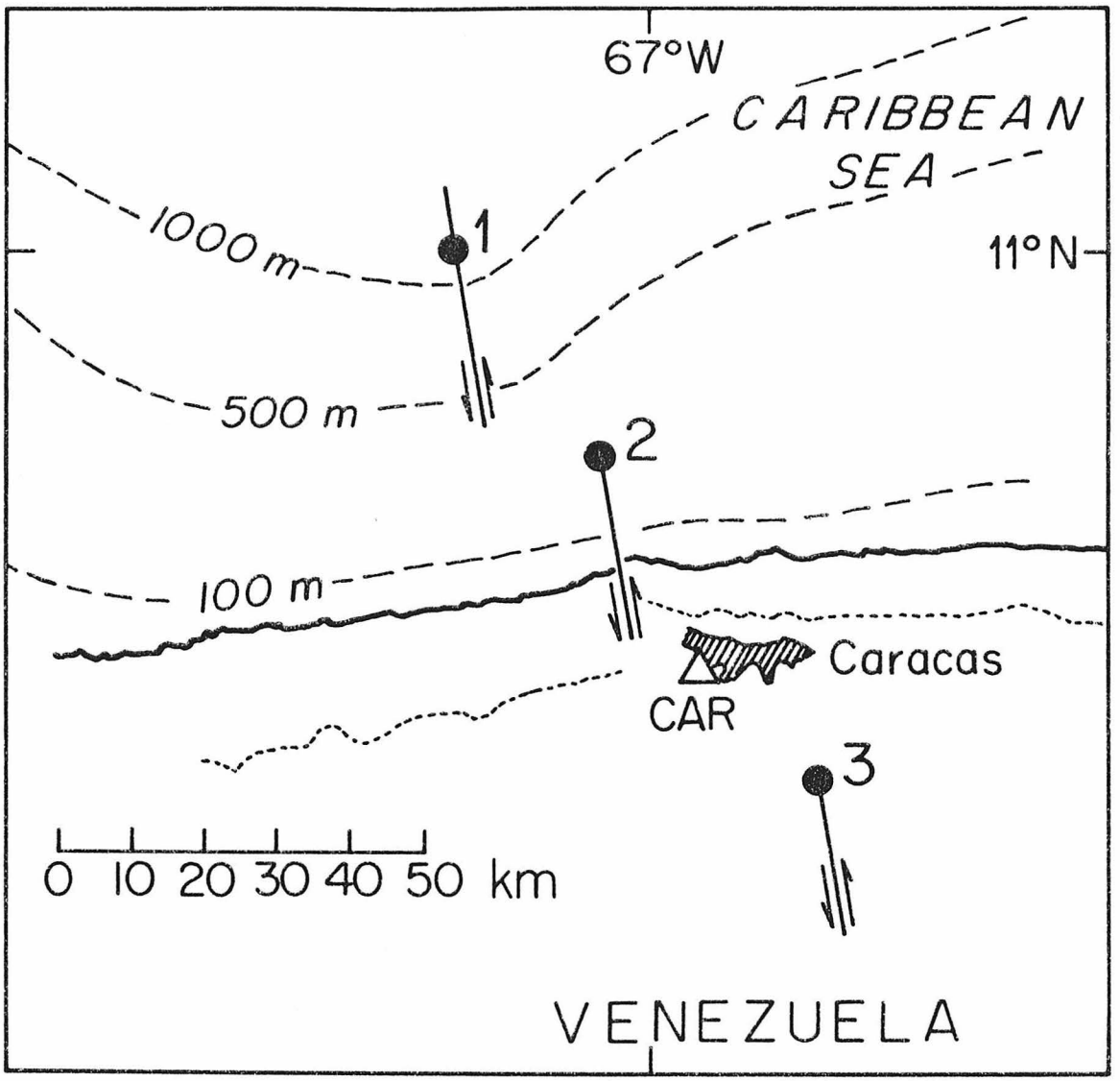

Fig. I.10 The three events in the local setting. The dotted lines on land represent the crest lines of the Coastal Ranges near Caracas.

propagation effects different rise times were used (0.8 s for LPA, 2.5 s for the other stations).

The earth structure between epicenter and station was selected from among appropriate models. As every path selected can be considered as pure-path, either oceanic (for stations GDH, KEV, NUR) or continental (LPA), a simple 40-layer ocean [Anderson, 1964] and an average continental [Gutenberg, 1951] earth models were used. The synthetic wave forms thus calculated reproduce quite accurately the observed ones. The values of M_o are in good agreement with those obtained using SH waves (Figure I.11).

Directivity Function

The directivity function for the Caracas event was calculated from the spectral ratios of the long period G2 surface waves recorded at a pair of stations located symmetrically with respect to the epicenter. The procedure has been described elsewhere [Kanamori, 1970a]. Here it consists basically in the evaluation of the amplitude spectral ratio of equalized surface waves recorded at stations RES (Canada) and ARE (Peru). The spectra are determined from the G2 Love wave windowed between group velocities 4.7 and 4.2 km/s. The seismograms are digitized every 2 s. The usual FFT algorithm is applied to obtain the spectral densities. The spectral density ratios are equalized using the values of the attenuation coefficients from Kanamori [1970c].

The theoretical directivity function was calculated using Ben-Menahem [1961] equations. For equalized seismic signals to an identical distance this is:

$$|D| = \left| \frac{D(\theta_o)}{D(\theta_o+\pi)} \right| = \left| \frac{c/v_R+\cos\ \theta_o}{c/v_R-\cos\ \theta_o} \cdot \frac{\sin \frac{\pi L f}{c} (c/v_R-\cos\ \theta_o)}{\sin \frac{\pi L f}{c} (c/v_R+\cos\ \theta_o)} \right| \qquad (4)$$

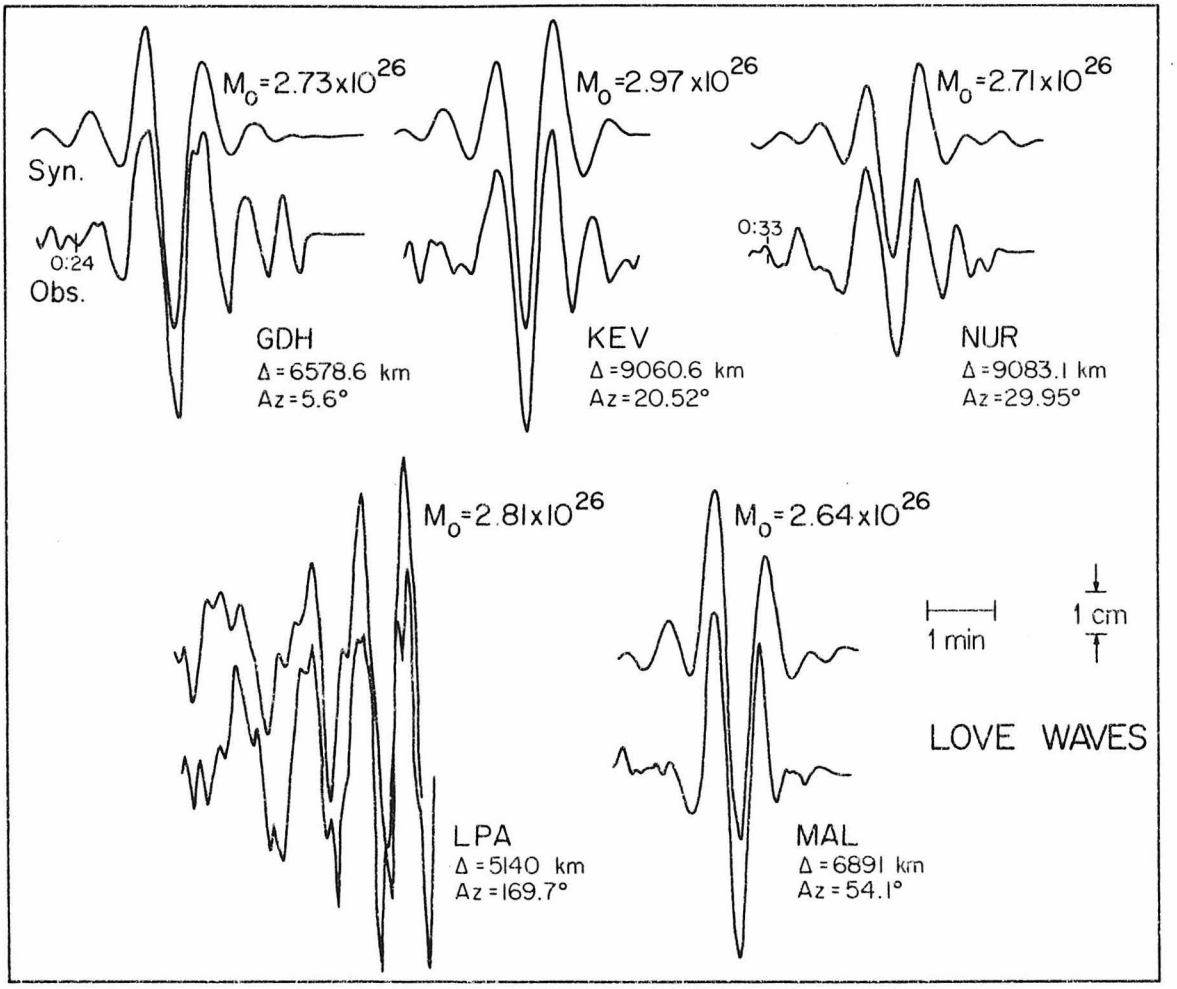

Fig. I.11 Comparison between synthetic and observed Love wave seismograms. Paths to GDH, KEV, NUR, and MAL are oceanic. Path to LPA is continental.

|D| is the directivity function magnitude, c and v_R are the phase velocity corresponding to the frequency f wave component and the rupture veolcity, respectively. θ_o is the angle with which the wave leaves the source, measured from the rupture direction, and L is the fault length. From (4) it is easy to predict, on the basis of the previous analysis, the shape of the observed directivity function. In fact, with $\theta_o = 0$, we shall have peaks in the directivity function for the ratio $G_2(\omega)\{RES\} / G2(\omega)\{ARE\}$ when

$$\frac{\pi L f}{c} (c/v_R+1) = n\pi \qquad n = 1,2 \tag{5}$$

With $n = 1$, $L = 90$ km (the distance between the first and third events), $v_R = 3.0$ km/sec and $c \simeq 4.5$ km/sec we get $T = 1/f \simeq 50$ s.

In Figure I.14 the observed directivity function is shown, and in fact a peak exists at $T = 52$ s. Working backwards from this value we obtain a fault length of 93.7 km when $v_R = 3$ km/s. Taking into account the averaging properties of long period radiation, the above numbers are remarkably close to both the distance between the extreme events (90 km) or the total length of ruptured faults (80 km) given by the model in Figure I.11. A second peak on Figure I.12 at about 100 s could be explained by rupture along a 130 km long fault and a rupture velocity of 2.1 km/s. Without more information than that of Figure I.12, one would have chosen to take the mean values115 km and 2.5 km/s as the source parameters.

The directivity function method has received severe criticism, especially when only one station is used and successive order surface waves are analyzed. From the results here reported it seems that the

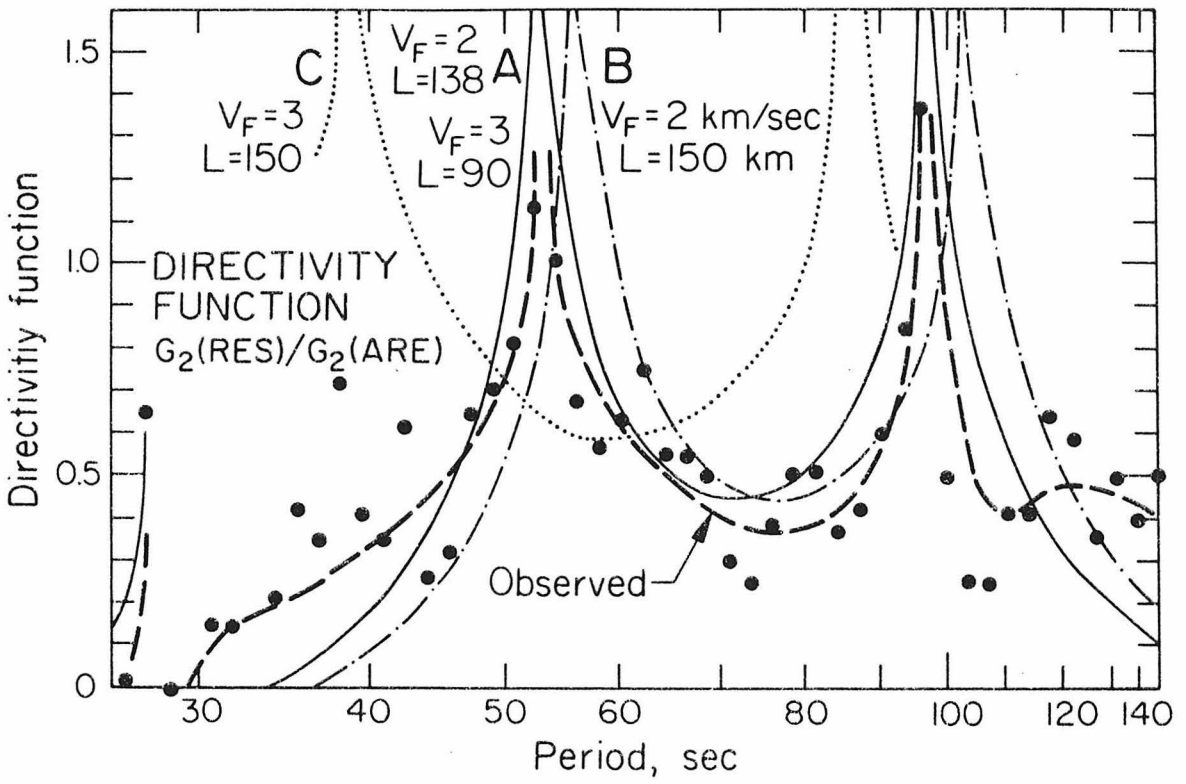

Fig. I.12 Directivity function for Love waves (G2) recorded at RES (Canada) and ARE (Peru).

stability of the method increases when two stations symmetrically located with respect to the epicenter are used and the same order wave is analyzed in both. We can conclude that the directivity function thus obtained may be useful and render accurate information, as long as other independent methods are used to check its results.

The Model

Table 1 and Figure I.10 summarize the findings of this study. The focal process is best described by considering the action of three different sources separated in space and time, occurring in succession from northwest to southeast on three seemingly "en echelon" left-lateral strike-slip faults.

The relative locations of the three sources are well resolved, especially for the first two. The third epicenter is obtained mainly on the basis of the constraints imposed by stations north and south of the epicenters, and is also reliably located. The relative location and separation figures (Table 1) are thus based upon direct seismogram measurements and P- and SH-wave synthetics. Errors are probably wihtin 10% of those figures. Fault parameters strike, dip, rake and focal depth are fairly well established from the initial trials based upon the factual knowledge of the first event's fault-plane solution (Figure I.2) and the observed P-wave azimuth independent similarity in wave forms among the three events (see Figures I.3 and I.4). These geometrical parameters by themselves are sufficient to fit closely the wave forms of each individual event. A number of models were tried in which the fault geometry of either the second or third sources were solely varied thus making it possible to estimate that errors

in these parameters are within 1% of the figures in Table 1. This and the above error estimates simply represent the particular parameter interval within which the synthetic seismograms remain stable.

These rather detailed results are indeed the fortuitous consequence of the source character, and especially of the resultant interference of SH phases which strongly constrains the model, large deviations from the model drastically changing the resulting synthetic wave form.

Other parameters such as rise time, rupture velocity and fault dimensions were last to be included in order to refine the original point-source trapezoidal far-field time function. Besides providing a closer fit to the detailed time duration of each event, a more realistic model that includes length and width of the faults is obtained.

The "en echelon" character of the three faults (Figure I.10) is needed to fit the data. Models with faults oriented otherwise (including the direction of the line joining the three sources) do not successfully fit all seismograms. As mentioned before, the P-wave seismograms show that there is little difference in the focal mechanisms of the three shocks besides the focal depth. The relative location of the individual events and their relative amplitudes become the crucial parameters where the SH seismograms are to be fitted. In Figure I.8 the delicate azimuthal dependence of SH wave forms at stations CMC, SCH, and STJ is shown. This is fairly reproduced by the synthetics only by considering the "en echelon" faulting of Figure I.10, as suggested originally by the P-wave synthetics. The best fit for the P-wave seismograms was found for a model with N10W trending fault planes while the three epicenters are on a N34W trending

line. The SH seismograms which are indeed more sensitive to azimuthal changes in the radiation pattern and relative locations and include stations that give better latitudinal control require that the epicenters be located on a N41W trending line. The difference in trending line with the P-wave model is of 7 degrees, which is not sufficient to drastically change the P wave forms. A compromise solution is depicted in Figure I.10 on which the three events are located on a N37W trending line and locations of the second and third events are closer to those which best fit the SH seismograms. With the location of the first event taken from Fiedler [1968] the modeled faults align along the well-known fault system of Tacagua on northwest Caracas, whose topographical expression is a short, narrow valley that sharply cuts the east-west trending Coastal Range (highest point 9072 feet) north of Caracas and suggestively displaces it from its west continuation by as much as 10 km in a left-lateral sense (see Figure I.10).

Tectonic Implications

The 1967 event is the only major, destructive earthquake occurring in the Caracas region since 1900 (October 29th). Instrumentally detected events have been routinely reported since 1963, when the WWSSN station CAR local bulletins report a substantial number of events between magnitudes 2.5 and 4 that occurred mainly within 20 and 60 km of the station. Precise epicenter locations, however, cannot be obtained due to the absence of other seismological stations in the region.

Tectonically, the area offshore north-central Venezuela is of critical importance in the understanding of the present and past movements of

the Caribbean plate. It has long been said that the southern boundary of the Caribbean plate runs along the inferred east-west right-lateral strike-slip San Sebastian fault, which presumably runs parallel to the coast 20 to 50 miles offshore. The major release of seismic energy in the last sixty-seven years, the Caracas 1967 earthquake, occurs nevertheless along a direction almost perpendicular, which suggests that although caused by a similar state of stress, (1) the Caracas 1967 event does not represent the current state of plate displacements, or (2) the recent plate displacements are northwest-southeast in this locality.

There exist several reports on the structure of the southern Caribbean basin and the Venezuelan borderland that point to the fact that this region is dominated by northwest-trending strike-slip faults that presumably cut the San Sebastian-El Pilar east-west trending fault system thus excluding its forming a continuous plate boundary [Peter, 1972; Bell, 1972; Rial, 1973]. It is also well known that north of the Caracas region the island chain of the Netherlands Antilles is heavily cut by northwest trending structures [Silver et al., 1975].

With the focal parameters determined in this paper, and by using the well-known relation $\overline{M}_o = \mu S \overline{D}$, where $\overline{M}_o$ is the total average moment over the fault surface S caused by the average dislocation $\overline{D}$, and $\mu = 3 \times 10^{11}$ dyne cm^{-2}, the total displacement induced by the Caracas earthquake is calculated to be 120 cm along the direction N10W. This gives an estimate of 1.8 cm/year for the local rate of tectonically accumulated displacement since the 1900 shock.

Holocene Geology of the Caracas Region

Several recent studies on Holocene sediments and structural patterns as well as seismic morphogenesis in North-Central Venezuela and the Caracas area point out quite explicitly that the modern regime of tectonic deformation in the area is associated with NW-SE faulting and differential vertical movements of large blocks of the Caribbean coastal range. Picard and Goddard [1975] in a detailed study of Central Venezuela coastal sediments and geomorphology conclude that the coastal region can be divided into two major segments, a western segment of subsided coast line with cliffs submerged as much as 600 feet, and an eastern segment associated with a wide continental platform which has emergent morphology. The region in which these two segments are in contact coincides with the NW-trending Tacagua system of faults near Caracas. It is suggestive that these coastline vertical movements occur in such a way that could well be explained in part by pivoted left lateral displacements along the NW-SE fault system.

In an excellent study of seismic morphogenesis and recent tectonics of Caracas, Singer [1977] concludes that the Holocene tectonic movements in the area occur along "en echelon" strike-slip fractures oriented N10°-15°W which disrupt and cut the east-west trending faults north and south of the Coastal Range, and that the present and recent seismicity of Caracas could well be related to the activity of the NW-SE fault system.

It is indeed quite difficult to establish along which of the faults in the NW system the Caracas 1967 earthquake occurred. There are several candidates, all of them showing indications of recent activity, and some

even aligned along the zones most heavily damaged during the 1967 earthquake such as the "Humboldt fault," a vertical N10W-trending topographically well-defined fault whose inferred trace crosses the 1967 heavily damaged sites of Los Palos Grandes (Caracas) and the town of Caraballeda on the coast. According to Singer (1977) large, chaotic deposits of identifiably avalanche-type induced by large seismic events in the years 1100 to 1500 are found within the alluvial sediments brought down by the "Quebrada Chacaito," the steep canyoned creek that runs along the Humboldt fault trace.

In a geological time scale, however, the Caracas earthquake might well represent a minor episode in the secular displacement of the Caribbean plate. It is easy to show that a large east-west trending fault "locked" in the vicinity of Caracas can alter the local shear stress pattern so that the present eastward movement of the Caribbean plate induces displacement along the northwest left lateral faults. If the Sebastian fault is secularly active and is presently locked, the results of this study may indicate that the Caracas event represents a minor break and that future large earthquakes in the region might well occur along the east-west fault zone.

REFERENCES

Anderson, D. L., Universal dispersion tables. 1. Love waves across oceans and continents on a spherical earth, Bull. Seism. Soc. Am., 54 681-726, 1964.

Bell, J. S., Geotectonic evolution of the southern Caribbean area, Geol. Soc. Amer. Mem., 132, 369-386, 1972.

Ben-Menahem, A., Radiation of seismic surface waves from finite moving sources, Bull. Seism. Soc. of Am., 51, 401, 1961.

Burdick, L. J., and C. A. Langston, Modeling crustal structure through the use of converted phases in teleseismic body wave forms, Bull. Seism. Soc. of Am., 67, 677-692, 1977

Burdick, L. J., and G. Mellman, Inversion of the body waves from the Borrego Mountain earthquake to the source mechanism, Bull. Seism. Soc. of Am., 66, 1485-1499, 1976.

Fiedler, G., Estudio sismológico de la región de Caracas con relación al terremoto del 29-7-1967, Bol. I.M.M.E., Universidad Central, Caracas año VI, Nos. 23-24, 1968.

Futterman, W. I., Dispersive body waves, J. Geophys. Res., 67, 5279-5291, 1962.

Gutenberg, B., ed., Internal Constitution of the Earth, Dover Publishers, 1951.

Gutenberg, B., and C. Richter, Seismicity of the Earth and Associated Phenomena, 2nd ed., Princeton University Press, 1954.

Harkrider, D., Surface waves in multilayered elastic media. I. Rayleigh and Love waves from buried sources in a multilayered elastic half-space, Bull. Seism. Soc. of Am., 54, 627-679, 1964.

Helmberger, D. V., Generalized ray theory for shear dislocations, Bull. Seism. Soc. of Am., 64, 45-64, 1974.

Jordan, T. H., The present-day motions of the Caribbean plate, Jour. Geophys. Res., 80, 4433-4439, 1975.

Kanamori, H., Synthesis of long-period surface waves and its application to earthquake source studies--Kurile Is. earthquake of October 13, 1963, Journ. Geophys. Res., 75, 5011, 5027, 1970a.

Kanamori, H., The Alaska earthquake of 1964: Radiation of long period surface waves and source mechanism, Journ. Geophys. Res., 75, 5029-5040, 1970b.

Kanamori, H., Velocity and Q of mantle waves, Phys. Earth. Planet. Int., 3, 1970c.

Langston, C. A., and D. Helmberger, A procedure for modeling shallow dislocation sources, Geophys. J., R.A.S., 42, 117-130, 1975.

Molnar, P., and J. Oliver, Lateral variations of attenuation in the upper mantle and discontinuities in the lithosphere, J. Geophys. Res., 74, 2648-2682, 1969.

Molnar, P., and L. Sykes, Tectonics of the Caribbean and Middle America regions from focal mechanisms and seismicity, Bull. Geol. Soc. of Am., 80, 1639-1670, 1969.

Papazachos, B. C., Dispersion of Rayleigh waves in the Gulf of Mexico and Caribbean Sea, Bull. Seism. Soc. of Am., 54, 909-926, 1964.

Peter, G., Geologic structure offshore north-central Venezuela, Trans. Caribbean Geol. Conf. 6th, 283-294, 1972.

Picard, X. and D. Goddard, Geomorfologia y sedimentación de la Costa entre Cabo Codera y Puerto Cabello, Bol. AVGMP, Caracas, 18, 1, 39-106, 1975.

Rial, J. A., La fosa tectónica de Tacagua y su relación con la sismicidad de la region de Caracas, Bol. Asoc. Ven. Geol., Caracas, 8, 3, 49-54, 1973.

Rial, J. A., Implications of the focal processes of northern Venezuela earthquakes in Caribbean tectonics, EOS, 57, 954, 1976a (abstract).

Rial, J. A. Seismic-wave transmission across the Caribbean plate: High attenuation on concave side of Lesser Antilles island arc, Bull. Seism. Soc. of Am., 66, 1905-1920, 1976b.

Silver, E. A., J. E. Case, and J. H. MacGillary, Geophysical study of the Venezuelan Borderland, Geol. Soc. Amer. Bull., 86, 213-226, 1975.

Singer, A., Tectónica reciente, morfogenesis sismica y riesgo geológico en el graben de Caracas, Venezuela, Div. Geotecnia, Ministerio de Minas y Energia, Caracas, 1977.

Sykes, L. R., and M. Ewing, The seismicity of the Caribbean region, J. Geophys. Res., 70, 5065-5074, 1965.

Tarr, A. C., The dispersion of Rayleigh waves in the crust and upper mantle under the Western North Atlantic Ocean, Gulf of Mexico and Caribbean Sea, Ph.D. thesis (unpublished), University of Pittsburgh, 1968.

CHAPTER II

Seismic waves at the epicentre's antipode

ABSTRACT

The antipodal region ($178° \leq \Delta \leq 180°$) of a seismic wave source is investigated in detail and shown to provide a new set of remarkable data to use in the exploration of the earth's interior. Body and surface waves converge individually at antipodal distances after having sampled laterally the totality of the planet. The waves are focused and strongly amplified up to one order of magnitude with respect to the normal phase recorded two or more degrees away. The delicate interference patterns thus formed yield information on departures from lateral homogeneity and sphericity of the core and mantle, the structure of the inner core, global dissipation characteristics of the upper mantle, and provide strong constraints on earth models.

Synthetic seismograms have been generated that closely reproduce the phases P_{diff}, PKIKP, PKIIKP, PKP(BC), PKP, and PP observed at WWSSN long period instruments located within 5 degrees from the antipode of the New Zealand (Inangahua) earthquake of May 23, 1968. Preliminary results indicate that the lower mantle and upper core are laterally homogeneous as seen by 15 s waves but the core-mantle boundary region is probably laterally inhomogeneous. The inner core–outer core boundary appears to be a sharp transition with a P-wave velocity jump of the order of 0.8 km/s. The resolution of the long period data is poor, but the potential richness of the method when better data sets are available strongly motivated the investigation. Analysis of surface Rayleigh waves at a single antipodal station indicates that the average dissipation of seismic energy in the upper mantle is higher than previously thought.

Ray theory underlies the computation of body wave seismograms. The mathematical approach and necessary corrections to geometrical optical solutions are thoroughly explained. The amplification phenomena and interference patterns produced by focusing of rays is successfully described by the uniform asymptotic forms of the Legendre function in terms of Bessel functions of order zero and one. Langer's approximation of the WKBJ radial eigenfunctions correctly quantifies the interaction of finite frequency rays with curved boundaries at grazing incidence.

Suggested future lines of research using antipodal observations include monitoring of inner core phases, study of focal processes of large earthquakes and the exploration of planetary interiors.

II.1 INTRODUCTION

Most of the current and past research on the structure and composition of the earth's interior is based upon observations of seismic waves at the surface and their interpretation in terms of appropriate models. The investigation requires different combinations of source-receiver locations according to what particular region is to be explored. All such possible combinations have already been used except that in which the receiver is located at or near the source's antipode [Rial, 1977, 1978].

It is the purpose of this work to show that the antipodal region ($\Delta \sim 180°$) of a seismic wave source can be used to extract valuable information about the earth's interior. Due to the spherically symmetric seismic velocity structure of the earth and the existence of a low velocity fluid core, many different families of seismic rays are focused at the antipode of a source creating the seismic analogue of a convergent optical lens image (Figure II.1). The unique ability of antipodal seismic stations to sample an infinite number of rays makes it possible to discuss the homogeneity or inhomogeneity of portions of the earth which would otherwise require a large number of observations.

The antipode acts as a collector of seismic body and surface wave information, thus providing the investigator with a global view of the earth concentrated in a very reduced area. Body waves such as PKP, PP, PcPPKP, PPP, SS, SKS, etc. arriving at the antipode produce delicate interference patterns whose stability, form, and extent strongly depend on the existence of deviations from a perfect radial symmetry of the structure sampled by the rays. Most of the P waves arriving at the

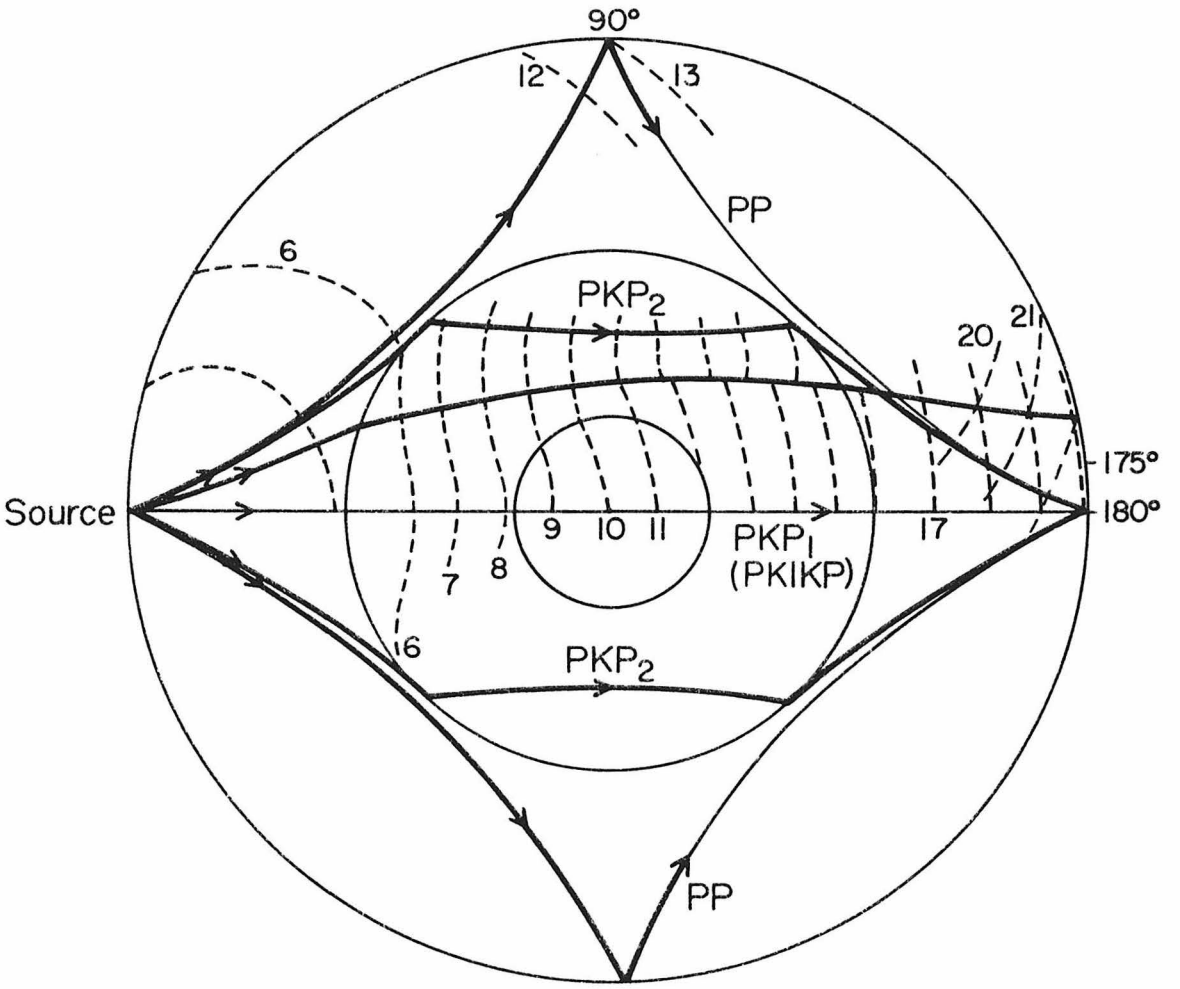

Figure II.1 The focusing of rays PP and PKP_2 (branch AB of PKP) at the antipode. Dashed lines represent selected wavefronts with propagation time in minutes.

antipode strongly interact with the outer and inner boundaries of the core, and some sample the structure in the neighborhood of the earth's center (a region accessible only from antipodal observations). Furthermore, multiple surface waves from large earthquakes recorded at a single antipodal station can be used to determine azimuthally-independent, global averages of the anaelastic dissipation of seismic energy as a function of depth in the mantle.

Observations show that most body wave phases are strongly amplified up to one order of magnitude with respect to the normal phase recorded two or more degrees away from the antipode. Since the signal/noise ratio is enhanced in the same proportion, the seismograms provide clear and strong arrivals of otherwise weak signals, and perhaps of other seismic phases not yet observed elsewhere.

These phenomena have received little attention in the seismological literature since it is quite a fortuitous occurrence that a seismological station is located within one or two degrees from the antipode of a regular size earthquake with axisymmetric radiation pattern. Brief accounts on the possible focusing of seismic energy at antipodal distances are found in Gutenberg and Richter [1934], although no attempt is made to analyze the phenomena, nor are observations reported. Other indirect references are found in Bolt and O'Neill [1964] who suggested the possibility, confirmed in the present work, that very weak signals like PKIIKP can be amplified strongly enough at the antipode to be observable. Burridge [1963] computed time domain antipodal amplitudes of body waves reflected from the surface of a homogeneous solid sphere and Alterman and Loewenthal [1972] discussed briefly the amplification effect

for simplified homogeneous earth models. Antipodal radio waves have, by contrast, received repeated attention since the times of Van der Pol and Bremmer (1937), but in seismology they have even been regarded as unimportant (Chapman, 1969).

In the present work only WWSSN records at few locations around the antipode of three earthquakes were available. The study deals mainly with body and surface waves recorded on the long period (T_g = 100 s, T_s = 15 s) instruments, so the resolution is limited and the conclusions drawn regarded as preliminary. Short period signals were subjected to some scrutiny, but the highly complex nature of the earthquakes' sources impeded a similar treatment. The ideal sources for experiments of this nature are, of course, underground nuclear explosions and the ideal receiver is an array of seismometers centered at the proper antipode.

The simplest way to show how antipodal observations may be used is by comparing and matching observed seismograms with theoretically generated ones. In this dissertation synthetic seismograms of body waves are computed in two stages. First, since only natural earthquake records are available, it becomes necessary to determine the source geometry and time functions of the events to be studied. To this end we apply the Cagnard-deHoop method as developed by Helmberger (1968), Langston and Helmberger (1975), and Langston (1978) to reproduce teleseismic P waves recorded by the WWSS network at distances between 30 and 90 degrees from the epicenter. The source time function is modeled as that corresponding to a propagating finite dislocation imbedded in a layered medium containing a free surface. Second, following results of Friedman (1951) for the eigenfunctions of the radial form of the Helmholtz

equation, Langer (1949) uniform asymptotic expansions of Bessel functions of large order near turning points, and accounting for the focusing effect at the antipode by appropriate representations of the Legendre functions, we calculate the Green's functions for realistic earth models with radially varying elastic and anaelastic properties. Computationally we use the method developed by Richards (1970, 1973, 1976) and Cormier and Richards (1977), to generate impulse responses that include the effects of frequency dependent transmission-reflection-conversion coefficients. The theoretical development is a high frequency approximation that allows the displacement equations to uncouple into P, SV, and SH independent displacement potentials that solve canonical forms of the Helmholtz equation. The convolution of the source time functions with the impulse responses results in the synthetic seismogram. The selection of Richards' method as opposed to that of Gilbert and Helmberger (1972) is due to the fact that the Cagniard-deHoop scheme as it is developed presently for a spherically layered earth does not easily lend itself to the computation of the effect of frequency dependent transmission coefficients nor to the antipodal focusing.

Surface wave synthetic seismograms can be computed using the method developed by Saito (1967) and Kanamori and Cipar (1974), after a suitable representation of the Legendre polynomials in terms of Bessel functions is made to account for the antipodal focusing (Rial and Chael, 1978, in preparation).

The order of subjects to be presented is as follows. In Section II.2 we discuss the observed seismograms; the emphasis is on the first twelve minutes of long period records that include P_{diff}, PKIKP, PKIIKP,

PKP, PP, PcPPKP, and PPP. In Section II.3 we describe the basic theory underlying the computation of the synthetic seismograms in a rather heuristic manner, which relies more on physical motivation than on mathematical formality. None of the results are new to mathematics, and with the exception of the focusing effect treatment at the antipode, they are not new to seismology. The approach used in developing the theory is meant to be uniform, in the sense that wave propagation problems are solved by the introduction of solutions to the wave equation in terms of infinite series in the inverse powers of the frequency. Such series may have restricted domains of validity, so when a solution is required out of those domains, a new, more general series is developed from mathematical and physical arguments and successfully applied.

In Section II.4 synthetic and observed seismograms are compared, results are discussed, and in II.5 we show how surface waves recorded at antipodal distances are used to determine Q for the mantle.

II.2 DATA SET

The Inangahua earthquake of May 23, 1968 (M_s = 7.1) that occurred in New Zealand with epicentral coordinates 41.72S, 172.03E and a focal depth of 21 km (ISC) is one of the three shallow seismic events recorded by an adequate number of stations situated within 5 degrees of the epicenter's antipode in the last 20 years. On the basis of record quality and symmetry of the fault plane solution this event was selected as the subject of this research. The shock was recorded at MAL(Δ = 175°), TOL(Δ = 176.5°), and PTO(Δ179.25°) as shown in the long period vertical seismograms of Figs. II.2 and II.3. Figure II.2 shows the remarkable

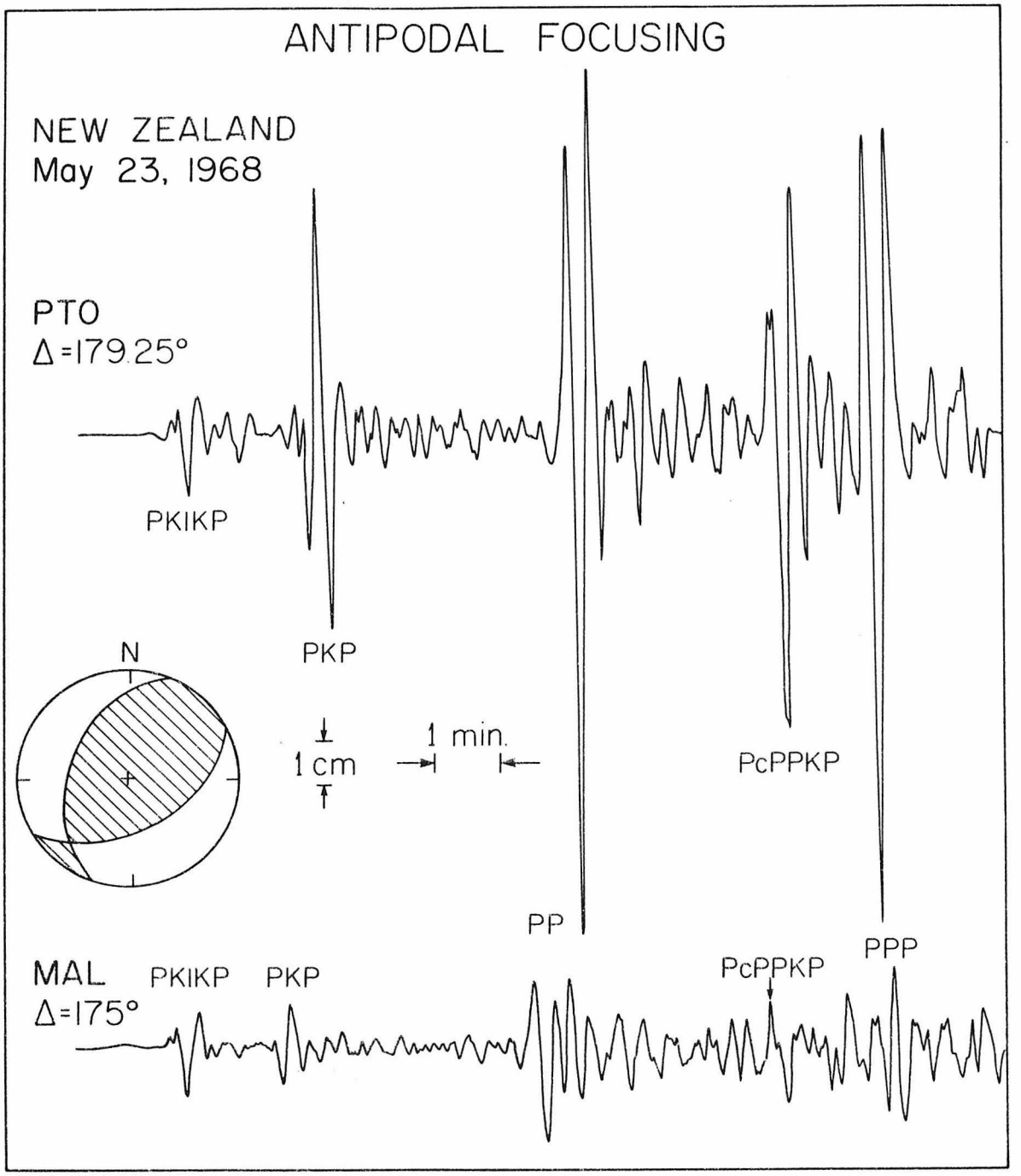

Figure II.2 The focusing effect strongly amplifies the signals up to one order of magnitude with respect to the normal phase recorded 2 or more degrees away. (Inangahua earthquake of May 1968). WWSSN long period vertical.

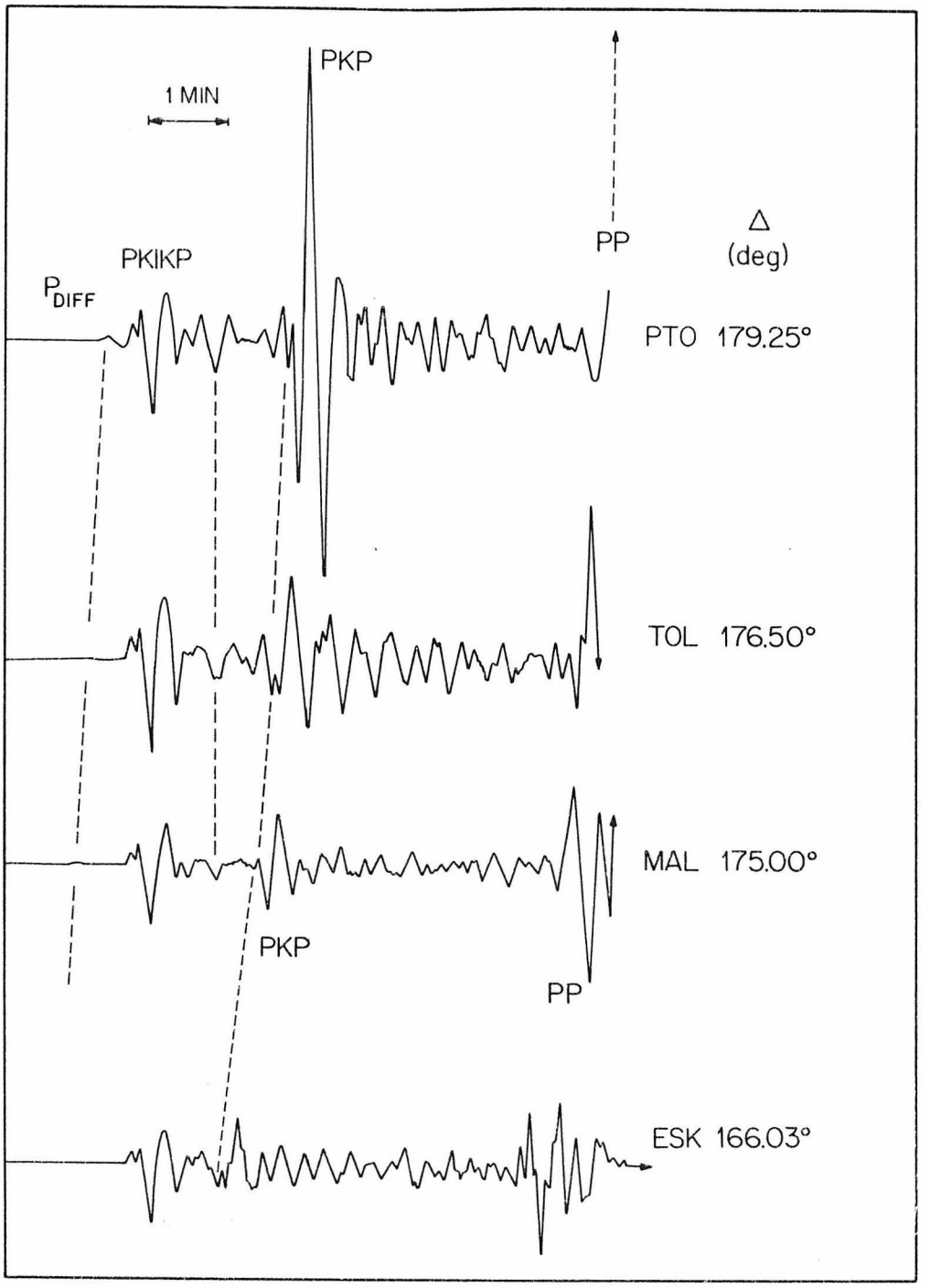

Figure II.3 The Inangahua event at four antipodal stations. Note the arrival between PKIKP and PKP. WWSSN long period vertical.

focusing effect that occurs as a consequence of the constructive interference of coherent seismic pulses arriving almost simultaneously to the receiver. All but the direct PKIKP phases are strongly amplified. The first arrival at both stations is the P-wave diffracted by the core, and the first optical arrival is the direct P wave transmitted close to the axis source-receiver. Figure II.3 shows the Inangahua event as recorded at four stations close to the antipode. The interference of PKP is nicely demonstrated and the focusing effect clearly seen. Between PKIKP and PKP a rather unexpected phase, which also shows amplification, is recorded. Its travel time coincides approximately with PKIIKP and its subsidiary branches (Fig. II.4), that is, multiple reflections from the inner side of the inner core. It is shown below that this phase can be generated synthetically by the interference of PKIIKP and PKP(BC), the long period diffracted energy off the tip of the BC branch of PKP.

In this dissertation synthetic seismograms have been generated for the first seven minutes of the record, that is, including up to PP, at distances ranging from $\Delta = 175°$ to the antipode itself. In the analysis of surface waves the data set consisted of the vertical component of the long period instrument at PTO which includes multiple Rayleigh wave arrivals up to R6.

II.3 THEORETICAL DEVELOPMENT

The propagation of seismic waves through the earth is one of the basic problems of theoretical seismology. Scholte (1956), following closely the mathematical theory of high frequency radio waves propagating around the earth derived analogous results for several distinct seismic

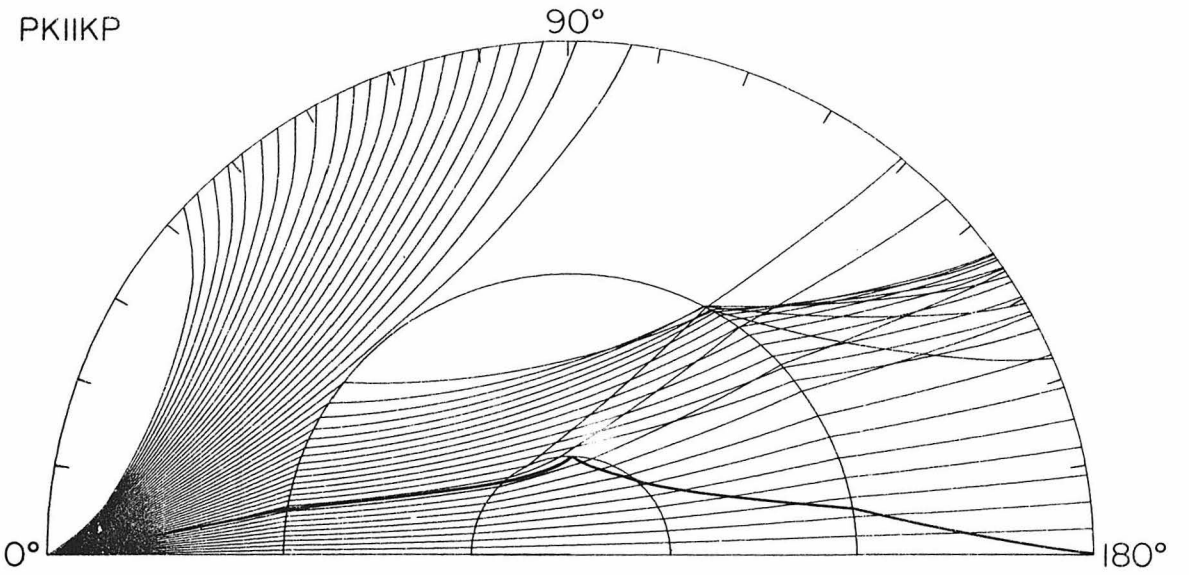

Figure II.4 The PKIIKP rays converge at the antipode after being reflected from the inner side of the inner core.

body wave phases in a homogeneous two-layered earth with a fluid core. Although most of Scholte's work is limited to the geometrical optics of body waves, some of his results include the field at the PKP caustic and diffracted P in the shadow zone. The mathematical theory hinges on two basic tools of the analysis, the Watson transformation (Watson, 1918; Van der Pol and Bremmer, 1937) and the Debye (rainbow) expansion of the incident field into an infinite series of interactions with the core boundary, analogous to the multiple internal reflection treatment of the Fabry-Perot interferometer. In the homogeneous earth case the Watson transform is applied to each individual term of the Debye expansion. The asymptotic behavior of each term is usually dominated by contributions of two types: (1) saddle point contributions associated with geometrical optic rays, corresponding to the first term of the WKBJ solutions to both the radial and tangential forms of the wave equation in spherical coordinates of cylindrical symmetry, and (2) residue series contributions, associated to surface waves diffracted along major interfaces of the medium. Contributions from higher order saddle points associated to caustics, cusps and focusing can also be evaluated by suitable manipulations of the integral responses.

The general case of high frequency seismic waves propagating through an inhomogeneous (radially varying) earth has been developed only recently in the seismological literature, although the basic equations and mathematical theory had long been available from the works of Karal and Keller (1959), Babich and Alekseyev (1958), Chekin (1959), Friedman (1951), Bremmer (1949), Langer (1931, 1934, 1949), Budden (1961), etc. The availability of a large amount of seismic wave data and high-

speed computers in the last decade has been a decisive incentive for seismologists to pursue the computation of synthetic seismograms for realistic earth models as a means of modeling the interior of the earth on the basis of observations at the surface. Chapman (1969), Richards (1970), Fuchs and Muller (1971), Gilbert and Helmberger (1972), Richards (1973, 1976), Cormier and Richards (1977), and others have developed such theoretical-computational techniques.

The present work deals basically with antipodal observations of body waves and the construction of appropriate synthetic seismograms for realistic earth models. For this purpose two major features of antipodal rays must be brought into consideration: (1) Most of the observed phases graze the boundaries of the outer and inner cores, and (2) most of them are focused in the antipodal region. In order to correctly describe these effects in the theory, it is necessary to use high frequency approximations to the solutions of the elastodynamic equations that remain valid for grazing incidence and give finite amplitudes at focal points of rays. The mathematical theory to be used has been applied by Richards (1973, 1976) following results of Friedman (1951) and Langer (1949) and will be slightly modified to account for the focusing effect. The computational method consists essentially in numerical integration along suitable contours on the complex ray parameter plane to obtain the frequency domain response of a realistic earth model to a point source whose time history may be represented by a Dirac delta function. After applying the inverse Fourier transformation a Green's function in the time domain is obtained for each particular seismic ray. For a given seismic event the source time function is modeled by

using Cagniard-deHoop first motion approximation technique as explained by Langston and Helmberger (1975); the convolution of these two functions results in the synthetic seismogram. It is desirable for antipodal observations that the radiation pattern of the event to synthesize be axisymmetric. If this is not the case, an expression for it in terms of ray parameter must be included in the response integral before performing the contour integration.

The Method: The physical problem to solve is that of point source generated high frequency elastic waves, propagating in a perfectly elastic*, radially inhomogeneous earth, which after interacting with major internal discontinuities at grazing or nearly grazing incidence, converge and focus at the antipode of the source point. The mathematical description of high frequency electromagnetic waves in radially varying inhomogeneous media has been given in detail by Friedman (1951) and applied to body wave propagation in the earth by Richards (1973). The earth is assumed to be a sphere centered at the origin of a system of spherical polar coordinates r,θ,ϕ where r is the distance from the center, θ the colatitude, and ϕ the longitude. The differential equations satisfied by the wave displacement potentials generated at a point source of coordinates $(b,0,0)$ are

$$\nabla^2\phi + \frac{\omega^2}{\alpha^2(r)}\phi = -\frac{\delta(r-b)\,\delta(\theta)}{2\pi r \sin\theta} + \mathcal{O}\left(\frac{\tilde{u}}{\omega}\right)$$

$$\nabla^2\psi + \frac{\omega^2}{\beta^2(r)}\psi = 0 + \mathcal{O}\left(\frac{\tilde{u}}{\omega^2}\right) \qquad (1)$$

*We shall assume perfect elasticity at this moment for simplicity's sake.

where ϕ and ψ are azimuthally independent scalar functions that represent the P-SV displacement potentials for the high frequency uncoupled wave motions. ω is the angular frequency, $\alpha(r)$ and $\beta(r)$ are the P- and S-wave velocities in the medium. ϕ and ψ are related to the elastic wave displacement vector $\underset{\sim}{u}$ by the expression

$$\underset{\sim}{u}(r,\theta,\omega) = \frac{1}{\rho^{1/2}} [\text{grad}\,\phi + \text{curl}(0,0,-\frac{\partial\psi}{\partial\theta})] + \mathcal{O}(\frac{\underset{\sim}{u}}{\omega})$$

where ρ is the density at the source.

The solution $\phi(r,\omega,\theta)$ to the first of equations (1) is given by a series expansion of the form (Friedman, 1951)

$$\phi(r,\omega,\theta) = \sum_{n=0}^{\infty} (n+\frac{1}{2})\, u_n(r)\, P_n(\cos\,\theta) \qquad (2)$$

where $u_n(r)$ satisfies the radial form of the wave equation

$$\frac{d^2(ru_n)}{dr^2} + [K^2(r) - \frac{n(n+1)}{r^2}](ru_n) = -\frac{\delta(r-b)}{2\pi r} \qquad (3)$$

$$K(r) = \omega/\alpha(r)$$

The radiation condition applies on both ϕ and $u_n(r)$, such that

$$\lim_{r\to\infty} r\left|\frac{\partial\phi}{\partial r} - iK_o\phi\right| = 0$$

$$\lim_{r\to\infty} r\left|\frac{d(ru_n)}{dr} - iK_o r\, u_n\right| = 0$$

where K_o is an assumed constant value of $K(r)$ at $r = \infty$. The Legendre polynomial $P_n(\cos\,\theta)$ satisfies the equation

$$\frac{1}{\sin\theta}\frac{d}{d\theta}\left(\sin\theta\frac{dP_n}{d\theta}\right) + n(n+1)P_n = 0 \qquad (4)$$

Our basic interest here resides on the high frequency representations of the solutions to equations (3) and (4). As mentioned above, body wave rays arriving at antipodal distances have their turning points in the neighborhood of the major discontinuities of the earth, the outer and inner boundaries of the liquid core. In order to solve for the displacements associated with those rays, boundary conditions must be satisfied at those discontinuities. It will be shown that the amplitudes associated with the geometrical optical rays represented by the WKBJ solution of equation (3) are unbounded at the turning point, and thus a better approximation must be sought. In much the same way, the asymptotic (WKBJ) forms of the Legendre polynomials result in unbounded amplitudes at the antipode ($\theta = \pi$) which analogously is a turning point for the high frequency latitudinal component of the wave displacement. In order to solve equation (3) we must determine the solution of

$$\frac{d^2\psi}{dr^2} + \omega^2\left[\frac{1}{\alpha^2(r)} - \frac{n(n+1)}{\omega^2 r^2}\right]\psi = 0$$
$$\psi = r\,R(r) \qquad (5)$$

We can obtain an asymptotic form of the eigenfunctions $\psi_n(r)$, valid for ω large by assuming an infinite series solution in the inverse powers of frequency, so it will be useful at high frequencies. In fact, the leading term is just the solution which one would construct according to the principles of geometrical optics, and the subsequent terms are corrections to it. To this end we follow Karal and Keller (1959) and use the following ansatz:

$$\psi_n(r) \sim e^{i\omega S(r)} \sum_{j=0}^{\infty} (i\omega)^{-j} A_j(r) \tag{6}$$

(For a time-harmonic solution we append the factor $e^{-i\omega t}$ to (6)). The expansion (6) is called a ray series. $S(r)$ and $A_j(r)$ are ω-independent functions to be determined. $S(r)$ is the phase function, and the A_j's are the amplitude coefficients of the ray series.

Inserting (6) into (5) we have,

$$i\omega S''(r) \sum_j (i\omega)^{-j} A_j(r) - \omega^2 [S'(r)]^2 \sum_j (i\omega)^{-j} A_j(r)$$

$$+ i\omega S'(r) \sum_j (i\omega)^{-j} A_j'(r) + i\omega\, S'(r) \sum_j (i\omega)^{-j} A_j'(r)$$

$$+ \sum_j (i\omega)^{-j} A_j''(r) + \omega^2 \left[\frac{1}{\alpha^2(r)} - \frac{n(n+1)}{\alpha^2 r^2}\right] \sum_j (i\omega)^{-j} A_j(r) \equiv 0$$

where

$$S'(r) \equiv \frac{dS(r)}{dr} \quad , \qquad A_j'(r) \equiv \frac{dA_j(r)}{dr}$$

By retaining the highest power of ω we find that

$$S(r) = \pm \int_{r_p}^{r} \left[\frac{1}{\alpha^2(\xi)} - \frac{n(n+1)}{\omega^2 \xi^2}\right]^{1/2} d\xi \tag{7}$$

where r_p is that value of r for which the integrand vanishes. The following recurrence relations are found:

$$2S'(r)\, A_j'(r) + S''(r)\, A_j(r) = -(A_{j-1})'', \quad j = 0,1,\cdots$$

where we define $A_{-1} \equiv 0$. Thus, we have the result

$$A_j(r) = \left[\frac{1}{\alpha^2(r)} - \frac{(n+1)n}{\omega^2 r^2}\right]^{-1/4} \left\{ b_j - \frac{1}{2} \int_{r_p}^{r} \left[\frac{1}{\alpha^2} - \frac{n(n+1)}{\omega^2 r^2}\right]^{-1/4} (A_{j-1})'' dr' \right\}$$

$j = 0,1,\cdots$, $A_{-1}'' \equiv 0$

Considering only the term with $j = 0$, we get

$$A_o(r) = \left[\frac{1}{\alpha^2(r)} - \frac{n(n+1)}{\omega^2 r^2}\right]^{-1/4} b_o$$

and $S(r)$ is given by (7). b_o is a constant to be determined. Substituting these results back into (6) we obtain

$$\begin{matrix}(1)\\(2)\end{matrix} R(r) \quad \frac{b_o}{r\left(\frac{1}{\alpha^2(r)} - \frac{n(n+1)}{\omega^2 r^2}\right)^{1/4}} \exp\left[\pm i\omega \int_{r_p}^{r} \left(\frac{1}{\alpha^2} - \frac{n(n+1)}{\omega^2 r^2}\right)^{1/2} dr'\right] \quad (8)$$

In a homogeneous medium $\alpha(r) = \alpha = \alpha_s$ and (8) must have the form of Hankel functions, $H_n^{(i)}(kr)$ with $i = 1$ representing outgoing waves and $i = 2$ ingoing waves (from the center of the sphere.) We use the conventional Fourier transform pair given by

$$F(\omega) = \int_{-\infty}^{\infty} f(t)\, e^{i\omega t}\, dt$$

$$f(t) = \frac{1}{2\pi} \int_{-\infty}^{\infty} F(\omega)\, e^{-i\omega t}\, d\omega$$

Then, by using the Debye asymptotic forms (Watson, 1966) for $H_n^{(i)}(kr)$ we find that

$$b_o = \alpha_s^{1/2} \frac{e^{\pm i\pi/4}}{\omega}$$

We see that (8) coincides with Richards' (1973) radial eigenfunctions for $\omega r > (n + \frac{1}{2})\, \alpha(r)$. The approximation (8) neglects terms of order $1/\omega$. It is easy to see the failure of expression (8) when $1/\alpha^2 = \frac{n(n+1)}{\omega^2 r^2} = p^2/r^2$ where p is the ray parameter whose value at the turning point of the ray is precisely $r_p/\alpha(r_p)$.

The Langer Approximation. The behavior of solutions like (8) near the turning point is easy to infer from (5). If we represent equation (5) as $\psi'' + \omega^2 s^2(r)\psi = 0$, where ω is large and positive and $S = S(r)$ is such that $S^2(r)$ is a monotonically increasing function of r and has a zero (turning point) at $r = r_p$, we have that

$$\psi(r) = \frac{A}{S^{1/2}(r)} \exp[i\omega \int_{r_p}^{r} S(r')dr'] + \frac{B}{S^{1/2}(r)} \exp[-i\omega \int_{r_p}^{r} S(r')dr']$$

for $r > r_p$ (above the turning point), and

$$\psi(r) = \frac{C}{(-s^2)^{1/4}} \exp[\omega \int_{r}^{r_p} (-s^2)^{1/2}\, dr'] + \frac{D}{(-s^2)^{1/4}} \exp[-\omega \int_{r}^{r_p} (-s^2)^{1/2} dr']$$

for $r < r_p$ (below the turning point). These forms show that the solution is oscillatory above the turning point and exponential below it (A,B,C,D are integration constants). This behavior suggests the possibility of representing the solution of (5) in terms of functions that reproduce the oscillatory and exponential characters and are bounded at the turning point. The suggestion by Rayleigh (1912) to use such functions was formally developed by Langer (1931) who shows that associated with a given equation of the type (5) there may be a certain "related" equation whose solutions asymptotically reproduce those given above. The Airy functions $A_i(z)$ have the adequate behavior, and in order to represent solutions of (5) it is easy to show that their argument must be proportional to $-\omega^{2/3}$ (see, for instance, Olver, 1974). Operating as in the previous case we try a new ansatz for equation (5) in the form

$$\psi \sim W[-\omega^{2/3}S(r)] \sum_{j=0}^{\infty} \omega^{-2j} B_j(r)$$

$$+ \omega^{-4/3} \dot{W}[-\omega^{2/3} S(r)] \sum_{j=0}^{\infty} \omega^{-2j} C_j(r) \qquad (9)$$

where $\ddot{W} - tW = 0$ is the equation satisfied by the Airy functions Ai(t), Bi(t). It is easy to show that the first series on the R.H.S. of (9) is sufficient by itself as a solution of equations of the form (5). The more general form (9) is needed for equations of more general type (Olver, 1974). Substituting the first series of (9) into (5) we obtain, after retaining terms in powers of ω^2:

$$-S(S')^2 + [\frac{1}{\alpha^2} - \frac{n(n+1)}{\omega^2 r^2}] = 0 \qquad (10)$$

and with terms of order $\omega^{2/3}$,

$$S''B_o + 2S'B_o' = 0 \qquad (11)$$

Conditions (10) and (11) are sufficient for our purposes. From (10) we get

$$S(r) = \{\frac{3}{2} \int_{r_p}^{r} [\frac{1}{\alpha^2} - \frac{n(n+1)}{\omega^2 \xi^2}]^{1/2} \, d\xi\}^{2/3}$$

and from (11)

$$B_o = \frac{1}{[S'(r)]^{1/2}}$$

Therefore, we can write

$$rR(r) \equiv \psi_n(r) \simeq K \frac{\left\{\frac{3}{2}\int_{r_p}^{r} \left[\frac{1}{\alpha^2} - \frac{(n+1)n}{\omega^2 r'^2}\right]^{1/2} dr'\right\}^{1/6}}{\left[\frac{1}{\alpha^2} - \frac{n(n+1)}{\omega^2 r^2}\right]^{1/4}} \quad Ai(-\omega^{2/3} S(r)) \qquad (12)$$

where Ai is the Airy function and K is a constant to be determined. Using the identity

$$Ai(t) = \exp(2\pi i/3)(-\pi t/3)^{1/2} H_{1/3}^{(1)/(2)}\left[\frac{2}{3}(-t)^{3/2}\right]$$

where $H_{1/3}$ is the Hankel function of order 1/3, and making

$$S(r) = \left\{\frac{3}{2}\int_{r_p}^{r} \left[\frac{1}{\alpha^2(\xi)} - \frac{n(n+1)}{\omega^2 \xi^2}\right] d\xi\right\}^{2/3} \equiv \left(\frac{3}{2}\zeta\right)^{2/3}$$

we have

$$Ai\left[-\left(\omega \frac{3}{2} \zeta\right)^{2/3}\right] = e^{\pm i2\pi/3} \left(\frac{\pi}{3}\right)^{1/2} \left(\frac{3}{2}\omega\zeta\right)^{1/3} H_{1/3}^{(1)/(2)}(\omega\zeta)$$

Thence (12) is given by

$$R(r) \sim \frac{K\zeta^{1/2}}{r\left[\frac{1}{\alpha^2} - \frac{p^2}{r^2}\right]^{1/4}} \exp(\pm 2\pi i/3)\left(\frac{\pi}{3}\right)^{1/2} \left(\frac{3}{2}\omega\right)^{1/3} H_{1/3}^{(1)/(2)}(\omega\zeta) \qquad (13)$$

where we made the usual change valid for n large, $\frac{n(n+1)}{2} \sim p^2 = \frac{(n+1/2)^2}{\omega^2}$. To determine K explicitly we compare (13) with the solution of (5) for $\alpha(r) = \alpha_s$ = constant and obtain

$$K = \alpha_s^{1/2}\left(\frac{3}{2}\right)^{1/6} \omega^{-5/6} e^{-\pi/2i}$$

and finally,

$$R(r) \sim \left(\frac{\alpha_s \pi}{2}\right)^{1/2} \frac{1}{r\omega^{1/2}} \zeta^{1/2} Q^{-1/2} e^{\pm i\pi/6} H_{1/3}^{(1)/(2)}(\omega\zeta) \qquad (14)$$

with $$Q = \left[\frac{1}{\alpha^2} - p^2/r^2\right]^{1/2} \quad , \quad \zeta = \int_{r_p}^{r} Q \, dr'$$

Equation (14) is identical to equation (12) of Richards (1976). The Langer approximation of the radial eigenfunctions includes terms of order down to $\omega^{2/3}$. By using the uniform asymptotic expansion (14) in the description of the radial functions we obtain a bounded value of the amplitude at the turning point and correct for the fact that the transmission, reflection, and conversion coefficients at grazing incidence become frequency dependent functions.

The Focusing Effect at the Antipode: As mentioned before, the WKBJ solution to the Legendre equation fails at the antipode of the source ($\pi=\theta$), which in analogy to the previous considerations represents a turning point for the waves propagating in the θ-direction. The breakdown of the WKBJ solution comes from the simple geometrical fact that a spherical Legendre polynomial is represented by a linear cosine function.

Legendre's equation can be written for $n \to \infty$ and $m = 0$ as

$$\frac{1}{\sin\theta} \frac{d}{d\theta}\left(\sin\theta \frac{dP_n}{d\theta}\right) + \left(n+\frac{1}{2}\right)^2 P_n = 0 \qquad (15)$$

Following the same method as in previous pages, we use the ansatz:

$$P_{\nu - 1/2}(\cos\theta) \sim e^{i\nu S(\theta)} \sum_{j=0}^{\infty} (i\nu)^{-j} A_j(\theta) \quad , \quad \nu = n + 1/2$$

to find

$$P_n(\cos\theta) \sim \left(\frac{2}{\pi n \sin\theta}\right)^{1/2} \cos\left\{(n+1/2)\theta - \frac{\pi}{4}\right\} \qquad (16)$$

$$0 < \theta < \pi$$

Equation (16) can of course be determined by the saddle point approximation of the integral representation of $P_n(\cos\theta)$ (Copson, 1965).

The failure of (16) at $\theta = 0$ or π requires a search for a "related" equation of (15) and the introduction of a more general ansatz.

From (15), when $\theta \to 0$ and $n \to \infty$ such that $n\theta$ remains bounded, we get, with $\eta = n\theta$

$$\frac{1}{\eta}\frac{d}{d\eta}\left(\eta \frac{dP_n}{d\eta}\right) + P_n = 0 \qquad (17)$$

Since P_n is finite at $\theta = 0$, the only permissible solution of (17) is the Bessel function J_0. Since it is evident that equation (15) is not altered by changing θ by $\pi-\theta = \theta'$, we can, in the spirit of Langer's work, assume the following form of $P_n(\cos\theta')$

$$P_n(\cos\theta') \sim J_0[\nu S(\theta')] \sum_{j=0}^{\infty} A_j(\theta') (\nu)^{-2j}$$

$$+ \nu^{-1} \dot{J}_0[\nu S(\theta')] \sum_{j=0}^{\infty} B_j(\theta') \nu^{-2j} \qquad (18)$$

with

$$\ddot{J}_0 + \frac{1}{t}\dot{J}_0 + J_0 = 0 \qquad \dot{J}_0 \equiv \frac{dJ_0}{dt}$$

It is found by inspection that the two series in (18) are necessary to obtain uncoupled recurrence relations for the A_j and B_j coefficients. By inserting (18) into (15) and proceeding as before, we find

$$S(\theta') = \pm\theta' \qquad A_0 = \left(\frac{\theta'}{\sin\theta'}\right)^{1/2}$$

and retaining terms down to ν^0

$$B_0 = \left(\frac{\theta'}{\sin\theta'}\right)^{1/2} \left\{b_0 + \frac{1}{2}\int^{\theta'} \left(\frac{\sin\xi}{\xi}\right)^{1/2} (A_0'' + \cot\xi\, A_0')d\xi\right\} \qquad (19)$$

More general expressions can of course be obtained, but for the purpose of this work, and without loss of generality, we get, with $\theta' = \pi-\theta$

$$P_{\nu-1/2}(\cos\theta') \sim \left(\frac{\theta'}{\sin\theta'}\right)^{1/2} \left\{J_0[\nu\theta'] - \frac{1}{8}(\theta'\cot\theta'-1)\frac{J_1(\nu\theta')}{\nu\theta'}\right\}$$

$$+\mathcal{O}(\nu^{-2}) \qquad (20)$$

The asymptotic expansion (20) was obtained by Szegö (1934), and is uniform in an interval containing the antipode and gives a finite result for $\nu \to \infty$ and $\theta' \to 0$. The focusing effect created by rays converging to a point is correctly described by the Bessel function $J_0[\nu\theta']$ in a first approximation as it is evident that the term $\frac{1}{8}(\theta'\cot\theta'-1)\frac{J_1(\nu\theta')}{\nu\theta'}$ tends to zero very rapidly in the neighborhood of the focal point. The zeros of the Bessel function represent, for a given value of the frequency ω and fixed ray parameter, the spectral holes induced by destructive interference of rays arriving at a point with phases differing by π, thus forming alternate "light and shadow" annular regions around the antipode of high and low intensity of the wave field. These annuli are controlled in extent and number by the argument $\nu(\pi-\theta)$ of the Bessel function of order zero. It is instructive to observe that in the frame of reference of the antipode the function $J_0[\nu(\pi-\theta)]$ becomes $J_0(kr)$, where now r is the horizontal distance measured from the antipode, and k is the horizontal wave number, since for high frequencies the expression $(n+1/2) = \omega p$ is valid with $p = \frac{R\sin\phi}{V_0}$. (p is the usual ray

parameter, R is the earth's radius, ϕ the angle of incidence at the antipodal receiver, and V_o the seismic wave velocity at the surface.) Physically, the Bessel function represents standing waves generated by the interference of converging axisymmetric travelling waves. Computationally, expressions (16) and (20) have been compared within the ranges of distance and frequency adequate to the present study. For $178° \leq \theta \leq 180°$,* the asymptotic form (20) is used in full, whereas for $\theta < 178°$, representation (20) is substituted by (16). At $\theta = 178°$ both representations are identical for all practical purposes.

The Response Integrals. Even though the synthetic seismograms shown below have been generated for an inhomogeneous earth with radially varying elastic constants, it is instructive to start the description of the theoretical manipulations for the simpler case of a two-layered homogeneous perfectly elastic earth with a fluid core. In order to reduce complexity we shall describe the mathematical representation of PKP only.

PKP Potential. For a homogeneous earth, it is shown in Appendix A that the displacement potential associated with the PKP ray can be represented by

$$\phi_{PKP} = \sum_{n=0}^{\infty} (n+1/2)\ g(n)\ P_n(\cos\theta) \tag{21}$$

where

$$g(n) = T_{12}T_{21} \left\{\frac{\zeta_n^{(1)}(k_2a)}{\zeta_n^{(2)}(k_2a)}\right\} \left\{\frac{\zeta_n^{(2)}(k_1a)}{\zeta_n^{(1)}(k_1a)}\right\} \zeta_n^{(1)}(k_1b)\ \zeta_n^{(1)}(k_1r) \tag{22}$$

*Heretofore defined as the antipodal region.

after the general solution of (1) for a homogeneous mantle and core has been resolved into an infinite series (Debye or rainbow expansion). The PKP ray corresponds to the second term of such series, the rays PK^nP with $n > 1$ correspond to the subsequent terms and the direct and reflected rays (P and PcP) are identified with the first term of the rainbow expansion. The caustic of PKKP at about 240° from the source is in fact the seismological analogue of the rainbow produced by light interacting with suspended raindrops.

In (22) T_{12} and T_{21} are the (optical) plane wave transmission coefficients for waves entering and leaving the core. $\zeta_n^{(j)}(ka)$ are spherical Bessel functions that represent outgoing waves ($i = 1$) or ingoing waves ($i = 2$) from the center of the earth. k_2 and k_1 are the local wave numbers in the core and mantle respectively, the core radius is a, b the source radius, and r the distance measured from the origin of coordinates. θ is the epicentral distance measured from the source axis.

The Watson transformation (Watson, 1918) permits (22) to be rearranged into a contour integral, giving

$$\phi_{PKP} = \frac{1}{2i} \int_C \frac{\nu \, d\nu}{\cos \nu\pi} \, g(\nu - 1/2) \, P_{\nu - 1/2}(-\cos \theta) \qquad (23)$$

where C is the contour indicated in Figure II.5, taken around the zeros of $\cos \nu\pi$ on the positive real axis, in the clockwise direction, on the complex ν-plane. Following Van der Pol and Bremmer (1937), expression (23) is equivalent to

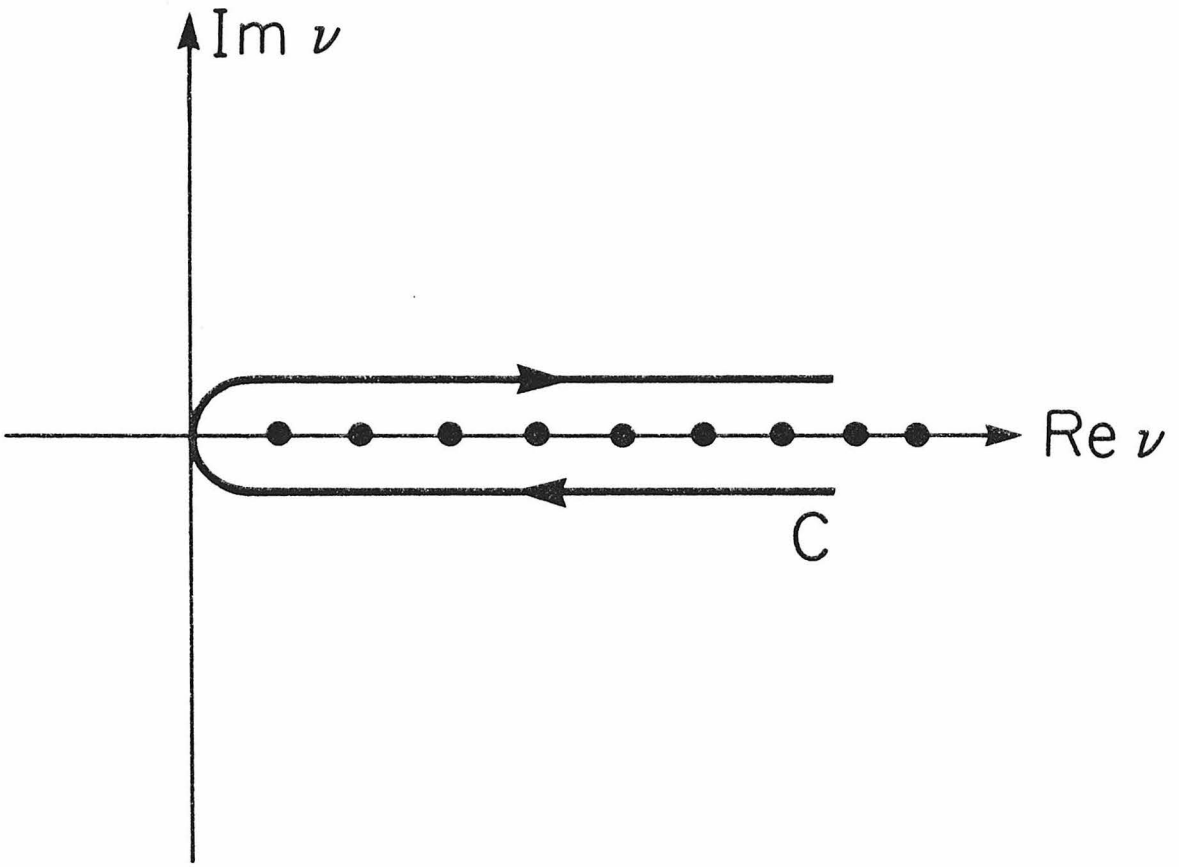

Figure II.5 Contour C in the complex ν-plane.

$$\phi_{PKP} = 2\pi i \sum \text{Residues} +$$

$$+ \frac{1}{2i} \int_0^{i\infty} \frac{\nu \, d\nu}{\cos \nu\pi} [g(\nu - 1/2) - g(-\nu - 1/2)] \, P_{\nu - 1/2}(-\cos \theta) \qquad (24)$$

where $\sum$ Residues is a general term detailed in Appendix B.

If $g(\nu - 1/2)$ is an even function of ν, (24) gives a non-optical field that represents only diffracted waves around the core. For waves like PcP observed in the shadow region $g(\nu - 1/2)$ is in fact an even function and its contribution is entirely determined by the residue series of (23) evaluated at the poles of $g(\nu - 1/2)$. In the lit zone, however, since $g(\nu - 1/2)$ is even, the original contour C is deformed to run across the saddle points of the integrand, whereas the Legendre function is split into terms representing travelling waves.

On the other hand, for PKP we have, since

$$\zeta^{(1)}_{\nu - 1/2}(ka) = \zeta^{(1)}_{-\nu - 1/2}(ka) \cdot e^{i\pi\nu} \quad \text{(Watson, 1966)}$$

that equation (24) gives

$$\phi_{PKP} = 2\pi i \sum \text{Residues} +$$

$$+ \frac{1}{i} \int_0^{\infty} \nu \, d\nu \, e^{i\pi\nu} \, P_{\nu - 1/2}(-\cos \theta) \, g(\nu - 1/2) \qquad (25)$$

(see Appendix B), where we have used

$$g(\nu - 1/2) - g(-\nu - 1/2) = -2i\, e^{i\pi\nu} \sin \nu\pi\, g(\nu - 1/2)$$

$$\frac{1}{2 \cos \nu\pi} = \sum_{m=0}^{\infty} (-1)^m \exp[i(2m+1)\nu\pi] \qquad \text{Im } \nu > 0$$

and

$$\tan(\pi\nu) \sim i \qquad \text{Im } \nu > 0$$

and a new contour deformation (Appendix B). The integral in (25) contains the optical rays we sought. In order to obtain their contributions the contour must be deformed to one Γ say, which runs across the PKP saddle points on the real ν axis. Thence, the ray contributions are given by

$$\phi_{PKP} = \frac{1}{i} \int_{\Gamma} \nu\, d\nu\, e^{i\pi\nu}\, g(\nu - 1/2)\, P_{\nu - 1/2}(-\cos\theta) \tag{26}$$

It is instructive to see that the factor $e^{i\pi\nu} P_{\nu - 1/2}(-\cos\theta)$ represents waves arriving at the receiver from the two opposite directions on the sphere. In fact,

$$e^{i\pi\nu} P_{\nu - 1/2}(-\cos\theta) = e^{i\pi\nu}[-i\, e^{i\pi\nu} Q^{(1)}_{\nu - 1/2}(\cos\theta) + i\, e^{-i\pi\nu} Q^{(2)}_{\nu - 1/2}(\cos\theta)] \tag{27}$$

(Nussenzveig, 1965)

Using the asymptotic expansions of the Legendre functions of the second kind

$$Q^{(1)}_{\nu - 1/2}(\cos\theta) \sim \frac{e^{\pm i(\nu\theta - \pi/4)}}{(2\pi\nu \sin\theta)^{1/2}}$$

(Abramowitz and Stegun, 1965)

we see that

$$e^{i\pi\nu} P_{\nu-1/2}(-\cos\theta) = \frac{1}{(2\pi\nu \sin\theta)^{1/2}} [e^{i\nu(2\pi-\theta) - i\pi/4} + e^{i\nu\theta + i\pi/4}]$$

The two terms in brackets represent travelling waves propagating in the negative and positive directions of θ respectively, with a constant phase difference of $\pi/2$ between them due to the passage through tne antipode of one of them (Fig. II.6).

At and near the antipode the uniform asymptotic expansion (20) must be used to give

$$\phi_{PKP}(\text{antipode}) \sim \frac{1}{i} \left(\frac{\theta'}{\sin\theta'}\right)^{1/2} \int_\Gamma \nu\, d\nu\, e^{i\pi\nu}\, g(\nu-1/2) \{J_0(\nu\theta') - \frac{1}{8}(\theta'\cot\theta' - 1)\frac{J_1(\nu\theta')}{\nu\theta'}\}, \quad \theta' = \pi-\theta \qquad (28)$$

$$g(\nu-1/2) = T_{12}T_{21}\left[\frac{\zeta^{(1)}_{\nu-1/2}(k_2a)}{\zeta^{(2)}_{\nu-1/2}(k_2a)}\right]\left[\frac{\zeta^{(2)}_{\nu-1/2}(k_1a)}{\zeta^{(1)}_{\nu-1/2}(k_1a)}\right]\zeta^{(1)}_{\nu-1/2}(k_1b)\zeta^{(1)}_{\nu-1/2}(k_1r)$$

Expression (28) is quite general and can be used for most antipodal phases with the appropriate form of $g(\nu-1/2)$.

We also see from (26) and (27) that if we wish to evaluate the direct ray of PKP at distances not near the antipode, we get

$$\phi_{PKP}(\text{direct}) \sim \int_\Gamma \nu\, d\nu\, g(\nu-1/2)\, Q^{(2)}_{\nu-1/2}(\cos\theta)$$

that is,

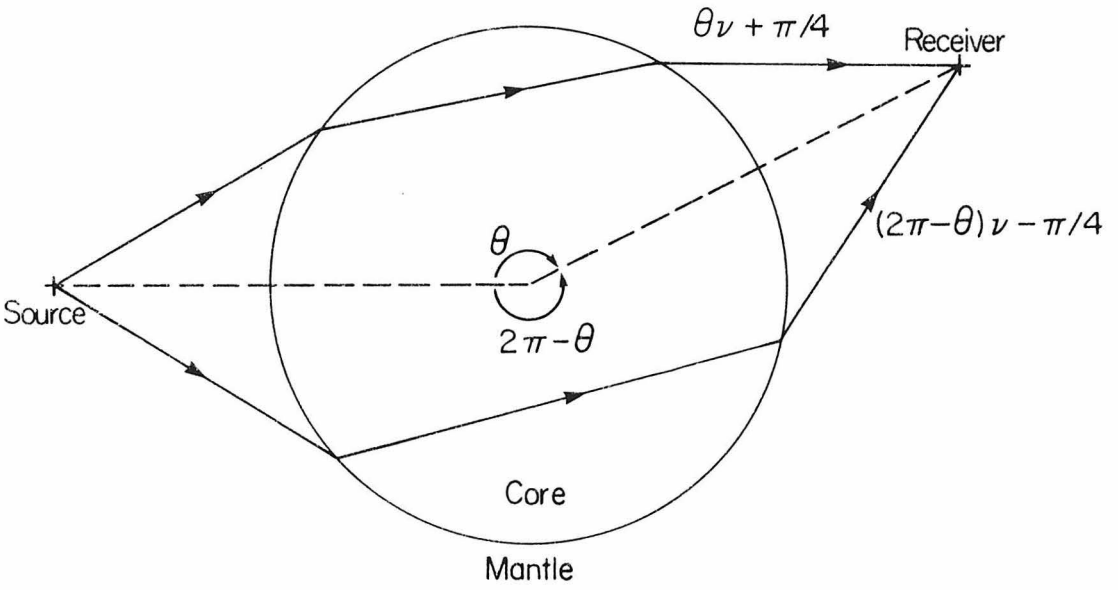

Figure II.6 Two PKP rays propagating in opposite directions.

$$\phi_{PKP}(\text{direct}) \sim \int_{\Gamma} \nu \, d\nu \, \zeta^{(1)}_{\nu-1/2}(k_1 b)\zeta^{(1)}_{\nu-1/2}(k_1 r)T_{12}T_{21}G(\nu-1/2) \times Q^{(2)}_{\nu-1/2}(\cos\theta) \tag{29}$$

with

$$G(\nu-1/2) = \{\frac{\zeta^{(1)}_{\nu-1/2}(k_2 a)}{\zeta^{(2)}_{\nu-1/2}(k_2 a)}\}\{\frac{\zeta^{(2)}_{\nu-1/2}(k_1 a)}{\zeta^{(1)}_{\nu-1/2}(k_1 a)}\}$$

Explicit expressions for T_{12} and T_{21} are given by Scholte (1956), Chapman (1969), Richards (1970,1973), etc. To compute the radial PKP displacements in (29) we first substitute all transcendental functions by their WKBJ asymptotic forms, compute $\frac{1}{\rho^{1/2}}\frac{\partial\phi}{\partial r}$ and retain the highest powers of ω, substitute $\nu = \omega p$ and obtain

$$u_r^{PKP}(\text{direct}) \sim \frac{e^{-i\pi/4}}{rr_s}\alpha_s(\frac{\omega}{2\pi\rho\sin\theta})^{1/2}\int_{\Gamma'} p^{1/2}\, T_{12}T_{21}\, e^{i\omega J(r,p)} \tag{30}$$

which for simplicity we have evaluated when the source and receiver are at the same radius r_s. Using the fact that

$$\int (1-\frac{a^2}{x^2})^{1/2}\,dx = (x^2-a^2)^{1/2} - a\cos^{-1}(\frac{a}{x})$$

we get:

$$J(r,p) = \frac{2}{\alpha_1}\left[\int_{r_p}^{r_s}(1-\frac{\alpha_1^2 p^2}{r^2})^{1/2}dr - \int_{r_p}^{a}(1-\frac{\alpha_1^2 p^2}{r^2})^{1/2}dr\right] + \frac{2}{\alpha_2}\int_{r_k}^{a}(1-\frac{\alpha_2^2 p^2}{r^2})^{1/2}dr + p\theta \tag{31}$$

Now Γ' is a scaled down contour in the complex p-plane, ω is real, and r_p and r_k are the turning points of the PKP ray extension into the core

and the core leg respectively, i.e., those points at which the respective integrands vanish. The term within brackets in (31) gives the phase along the straight ray in the mantle leg and the next integral gives the phase along the straight core leg. Comparing (30) and (31) with equation (16) of Richards (1973) we see that the only difference between the two expressions (accounting for the fact that Richards' expression is for PKKP and not for PKP) is that for the inhomogeneous case the phase $J(r,p)$ contains integrals in which the wave velocity α is not a constant, but an analytic function of the radius. Otherwise, (30) above and (16) of Richards (1973) are identical.

Therefore, it appears that the generalization from the homogeneous case to the inhomogeneous case can be made by careful inspection of the integral responses. This fact is not surprising since the expressions above are geometrical optics approximations. Therefore, in passing from the homogeneous to the inhomogeneous case, for high enough frequencies we just substitute in (29) say, the WKBJ Hankel functions for their inhomogeneous counterparts given by (8). Equation (30) however will fail to give the right displacement if the rays graze at the core boundary, since in that case the product of plane wave coefficients ($T_{12}T_{21}$) is zero. The remedy is to incorporate in $T_{12}T_{21}$ the generalized cosines of incidence that are computed from Langer's uniform asymptotic radial eigenfunctions given by (14). Thus the transmission coefficients will account for tunneling and the frequency dependent interaction with the boundary. Since representation (14) is uniformly asymptotic and reproduces (8) far from the turning points, the most general expression for the PKP displacement should be obtained by

replacing in (29) all Hankel functions with the corresponding radial eigenfunctions given in (14); however, mantle and core rays far from their interaction with discontinuities can safely be represented by forms (8).

PKP at the Antipode. Starting from expression (28) and following the previous reasoning we easily find, at and near the antipode, (using only the first term of (20) and approximating $(\frac{\theta'}{\sin\theta})^{1/2}$ to 1):

$$u_r^{PKP}(\theta,\omega,r) \sim \frac{\alpha_s \omega}{r r_s} \left(\frac{\alpha_s}{\alpha\rho}\right)^{1/2} e^{-i\pi/2} \int_{\Gamma'} p\left(\frac{\cos i}{\cos i_s}\right)^{1/2} f(p,\omega,\theta) e^{i\omega \hat{J}(r,p)} dp \qquad (32)$$

$$178° \leq \theta \leq 180°$$

and

$$f(p,\omega,\theta) = T_{PK}\left[\frac{m^{(2)}_{\omega p-1/2}(r_m)}{k^{(2)}_{\omega p-1/2}(r_m)}\right] T_{KP}\left[\frac{k^{(1)}_{\omega p-1/2}(r_m)}{m^{(1)}_{\omega p-1/2}(r_m)}\right] J_o[\omega p(\pi-\theta)]$$

(see Appendix B)

$$\hat{J}(r,p) = \int_{r_p}^{r} \frac{\cos i}{\alpha} dr + \int_{r_p}^{r_s} \frac{\cos i}{\alpha} dr + \pi p$$

where now T_{PK} and T_{KP} are generalized transmission coefficients, $m^{(2)}_{\omega p-1/2}(r_m)$ and $k^{(1)}_{\omega p-1/2}(r_m)$ are the radial eigenfunctions (14) in the mantle and core, respectively (analogous to $G(\nu-1/2)$ in (29)) with (1) and (2) referring to outgoing and ingoing waves respectively. The transmission coefficients are given by

$$T_{PK} = \rho_m \alpha_c [C^{(1)} + C^{(2)}] \cos^2 j_m / D$$

$$T_{KP} = 2\rho_c \alpha_m \cos i_c \cos 2j_m / D$$

$$D = \rho_c \alpha_c C^{(1)} + p_m[\alpha_m \cos^2 2j_m + 4s^2\beta_m^2 C^{(1)} \cos j_m] \cos i_c$$

where $C^{(1)}$ and $C^{(2)}$ are the generalized cosines defined by Richards (1976), the suffix m refers to the bottom of the mantle, c to the top of the core, and

$$\cos i_x = (1 - p^2\alpha_x^2/r^2)^{1/2} \qquad (x = m,c) , \quad s = p/r$$

$$\cos j_m = (1 - p^2\beta_m^2/r^2)^{1/2} \qquad \cos 2j_m = 1 - 2p^2\beta_m^2/r^2 \qquad r = r_m$$

Equation (32) is given by Rial (1978), with L_s there being an appropriate source strength factor. Finally, the time-domain synthetic seismogram for PKP for a point source delta function is given by

$$U_r^{PKP}(\theta,r,t) = \frac{1}{\pi}\int_0^\infty \omega \, \mathrm{Re}\left\{\int_{\Gamma'} g(p,\omega,\theta)\, e^{i\omega\hat{J}}\, dp\, e^{-i\omega t}\right\} d\omega \qquad (33)$$

with

$$g(p,\omega,\theta) = \frac{\alpha_s}{\gamma r_s}\left(\frac{\alpha_s}{\alpha\rho}\right)^{1/2} e^{-i\pi/2}\, p\left(\frac{\cos i}{\cos i_s}\right)^{1/2} f(p,\omega,\theta) \qquad (34)$$

In the actual computations the velocity profile $\alpha = \alpha(r)$ is described as a complex polynomial in r whose imaginary part takes into account the anaelastic dissipation of the earth. Equation (33) may include the source strength, the radiation pattern as a function of p and the source time function either as a convolution integral with (33) or as a frequency domain function multiplying $g(p,\omega,\theta)$.

For long enough periods the inner core may have an effect on the PKP energy even for antipodal distances. In that case, $f(p,\omega,\theta)$ in (32) must be multiplied by

$$\overset{\nearrow}{R}_i \left[\frac{k^{(2)}_{\omega p-1/2}(r_i)}{k^{(1)}_{\omega p-1/2}(r_i)} \right] \tag{35}$$

where $\overset{\nearrow}{R}_i$ is the generalized reflection coefficient from the outside of the inner core. (The inclusion of (35) into (32) improves the convergence of the integrand for the long period waves.) More direct interactions with the inner core, as in the case of PKIIKP and subsequent branches are computed by including the factor

$$T_{KI} T_{IK} \left[\frac{k^{(2)}_{\omega p-1/2}(r_i)}{k^{(1)}_{\omega p-1/2}(r_i)} \right] \left[\frac{i^{(1)}_{\omega p-1/2}(r_i)}{i^{(2)}_{\omega p-1/2}(r_i)} \right] \Big/ (1 - M) \tag{36}$$

with

$$M = \overset{\nwarrow}{R}_I \left[\frac{i^{(1)}_{\omega p-1/2}(r_i)}{i^{(2)}_{\omega p-1/2}(r_i)} \right]$$

where $\overset{\nwarrow}{R}_I$ is the generalized reflection coefficient at the underside of the inner core, and the radial eigenfunctions have obvious meaning. r_i is the inner core radius. T_{KI} and T_{IK} are the transmission coefficients in and out of the inner core. (See Cormier and Richards (1977) for a detailed description. Explicit expressions for T_{KI}, T_{IK}, $\overset{\nearrow}{R}_I$, and $\overset{\nwarrow}{R}_I$ are given in their appendix.)

Introduction of (35) or (36) in (32) involves careful definition of the general complex contour Γ' because new strings of poles are now present. Analytically it is a rather difficult problem to determine accurately the position of poles in the complex p-plane associated with all the earth's discontinuities. It is simpler indeed to numerically

compute the integrand in (32) along appropriate contours and check for convergence by suitably plotting the values of its real and imaginary parts. All the computational work here reported has been checked for convergence in such a fashion.

II.4 SYNTHETIC SEISMOGRAMS

Computation of synthetic seismograms is straightforward with the use of expressions of the form (32). For each particular body wave ray to be generated a typical procedure consists of (a) selection of a suitable integration contour on the complex ray parameter plane in agreement with the guidelines of the previous section (see Appendix B), (b) checking for integrand convergence, stability and adequate sampling rates within the selected frequency and epicentral distance ranges (the same integration contour is in general valid for a substantially broad range of epicentral distances), (c) inversion of the resulting response to the time domain, (d) convolution with the instrument time response.

Procedures (a) through (d) provide synthetic seismograms for a point source with a Dirac delta as time function. As explained in the previous section, several alternatives are possible when an earthquake source is considered. The general procedure calls for the inclusion of source parameters (radiation pattern, far-field source time function) into the integrands at some adequate stage of the computation.

An important factor to consider is, of course, the earth model to be used. We have found that for the range of frequencies considered (0.00781 Hz to 0.5 Hz) smooth earth models PEM (Dziewonski et al., 1975)

and 1066B are sufficiently accurate. An extension of model MM8 (Anderson and Hart, 1978) for Q_α and Q_β that includes $Q_\alpha \sim 10000$ for the outer core and 500 for the inner core was highly adequate. These models are not desirable, however, if higher frequency signals are to be generated. In fact they may not be accurate enough in the high frequency end of the above mentioned window. Nevertheless, the earthquake source time function of the event selected for this study is peaked near 0.08 Hz, thus the resulting synthetics are hardly sensitive to changes in the high frequency end of the spectrum. This indeed results in lack of model discriminating power for frequencies higher than perhaps 0.15 Hz. The results presented here do not claim greater resolution. This is not a problem of the analytic method, of course, but of the scarcity of analyzable data. It is very encouraging that even with such limited resolution the antipodal observations allow the investigator to draw significant conclusions about the earth; a consequence of extremely delicate interaction of the large number of rays that converge at the antipode after having thoroughly sampled the earth's core and mantle. As will be seen later, the long time function and the relatively large magnitude of the Inangahua earthquake provide, by contrast, an excellent data set to determine world average values of Q for mantle Rayleigh waves.

Results. Synthetic seismograms were generated at epicentral distances ranging between 175° and 180° for the phases P_{diff}, PKIKP, PKP(BC), PKIIKP, PKP, and PP. This corresponds to a 7-minute time window that starts with the first arrival of seismic energy at the receiver

(P_{diff}). Figure II.7 shows examples of the computed amplitude spectra for PKP and PP at distances of 175°, 176.5°, 178.34°, 179.25°, and 180°; all except the last selected according to the data available. (The sharp terminations on both sides of the frequency windows are artificially induced to indicate their size.) Except for the antipode signals all others show the effect of interfering signals in the form of spectral holes separated in frequency by an amount inversely proportional to the differential arrival times of the interfering pulses. Since neither the effect of the event far field time function, or the instrument are included, the resultant amplitude spectra must resemble that of either pure or interfering delta functions, the effect of attenuation reflected on the negative average slope of all curves. The focusing effect on the spectral content is clearly evident, especially for distances within two degrees of the antipode. The amplification is seen to be frequency dependent, reaching a maximum of about one order of magnitude at about 0.5 Hz. At the lowest frequencies spectral amplitudes are comparable. The clear difference in overall values of spectral amplitudes between PP and PKP is a consequence of the diverging character of the spreading coefficient of PKP in the distance range. More subtle differences in the frequency content of PKP and PP can better be noticed at Δ = 180°: A relatively stronger amplitude decrease with frequency for PP beyond 0.15 Hz may be caused by the extra path of this phase in the upper mantle, and the rapid relative decrease of the amplitude from that point to the low frequency end is suggestively in agreement with the expected tunneling of the long period PP energy into the core, which eventually becomes part of the PKP phase.

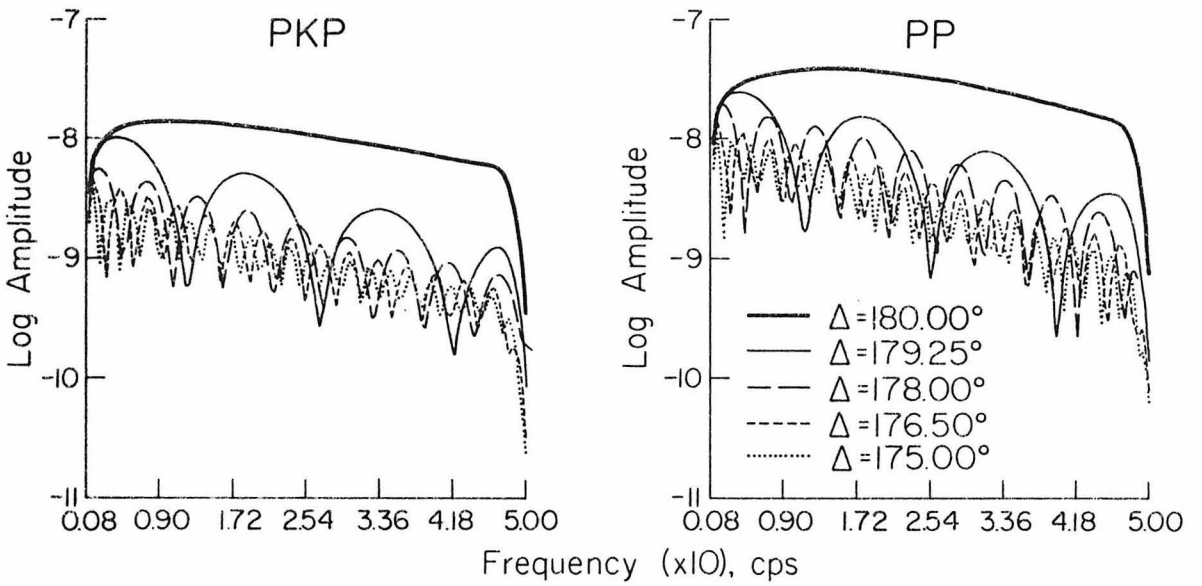

Figure II.7 Synthetic spectra for PKP and PP vertical components at several antipodal distances. (Attenuation is included. The source is a delta function. The effect of the instrument is not included.)

The focusing effect alone appears then as the major contributor to the overall changes in spectral amplitude with distance from the antipode for both PKP and PP. As shown below, this seems also to be the case for P_{diff}, PKP(BC) and PKIIKP. A perhaps more descriptive account of the focusing effect as a function of distance and frequency is shown in Figure II.8. Here the amplitude spectra correspond to the approximate (saddle point) evaluation of the PP phase for a simple homogeneous mantle and core earth model without attenuation. The functional form of the amplitude in that case is proportional to the product of a Bessel function of zero order times the square root of the inverse of the wavelength (Rial, 1978).

Figures II.9 and II.10 show the basic results of this study in the form of time-domain Green's functions for a point source in a PEM earth model with attenuation. As discussed before, phases that have interacted with the inner core–outer core boundary region have been included. It is instructive to examine Figure II.9 closely. The most obvious feature is the remarkable effect of the interfering phases PP and PKP arriving along opposite directions first as two least-time rays contained in the great circle plane of incidence, and finally at $\Delta = 180°$ the focusing of an infinity of rays arriving from every direction around the receiver, producing a clear ten-fold amplification. As discussed above, PKP amplitudes are consistently lower than those of PP. PKIKP, the direct wave, is of course not amplified in the process. An interesting result is that in fact the inner core phases PKIIKP and PKP(BC) show substantially large amplitudes within one degree of the antipode (see Figure II.10) suggesting that at antipodal distances their effect is

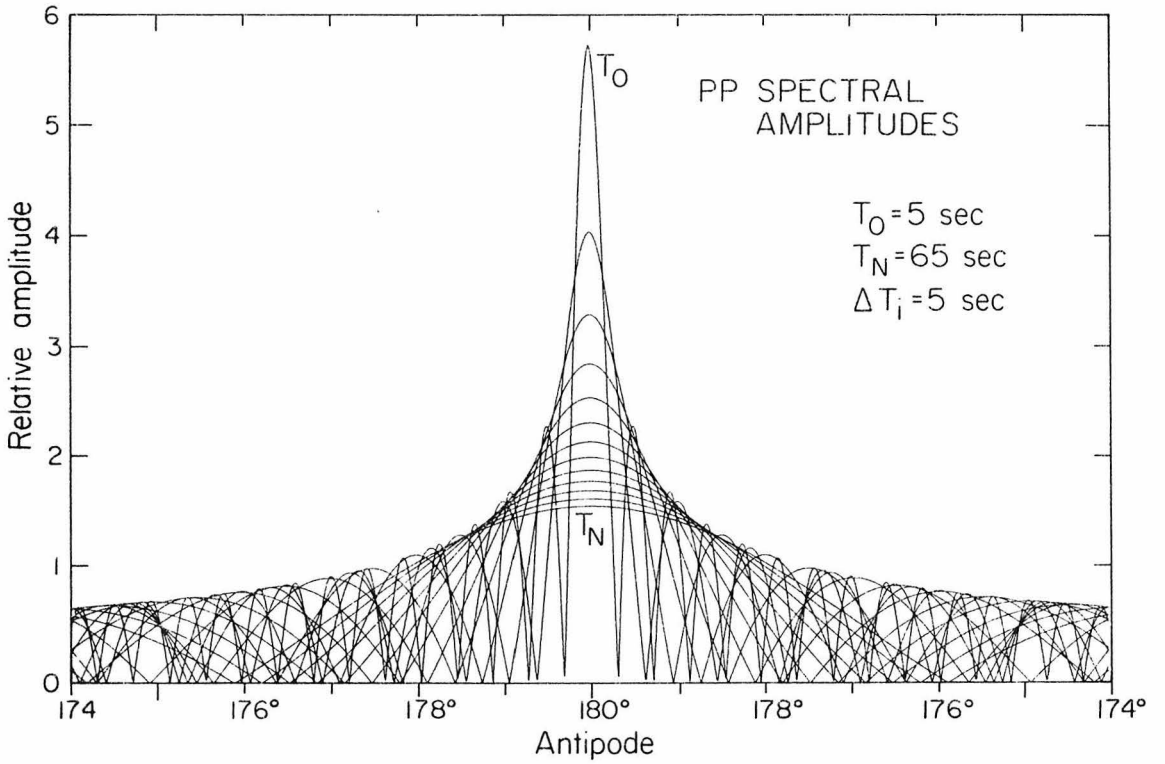

Figure II.8 Theoretical variation of the PP spectral amplitudes with distance from the antipode as a function of period.

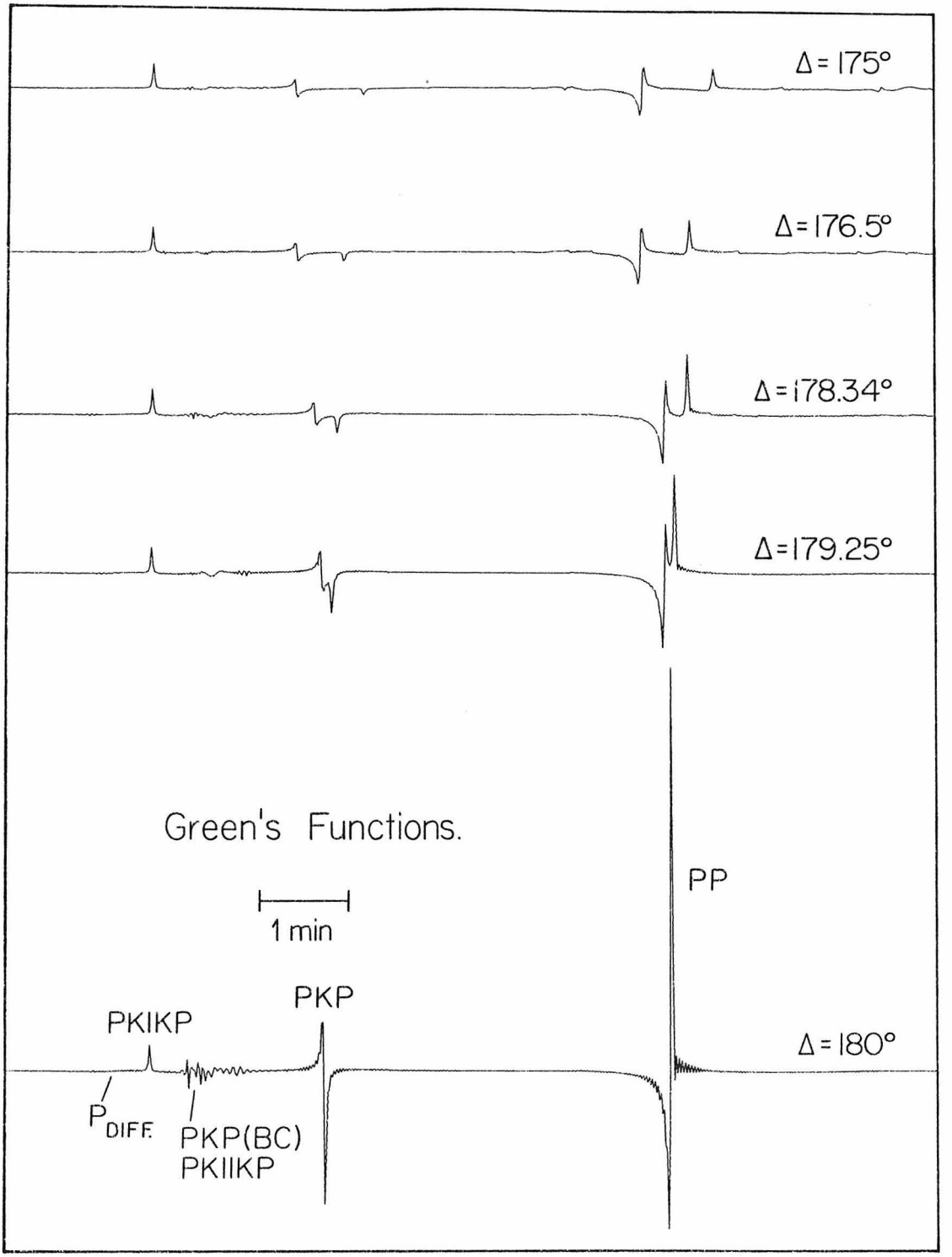

Figure II.9 Green functions for the vertical components of P_{diff}, PKIIKP, PkP(BC), PKP and PP at antipodal distances. Note the strong arrivals between PKIKP and PKP due to inner core phases.

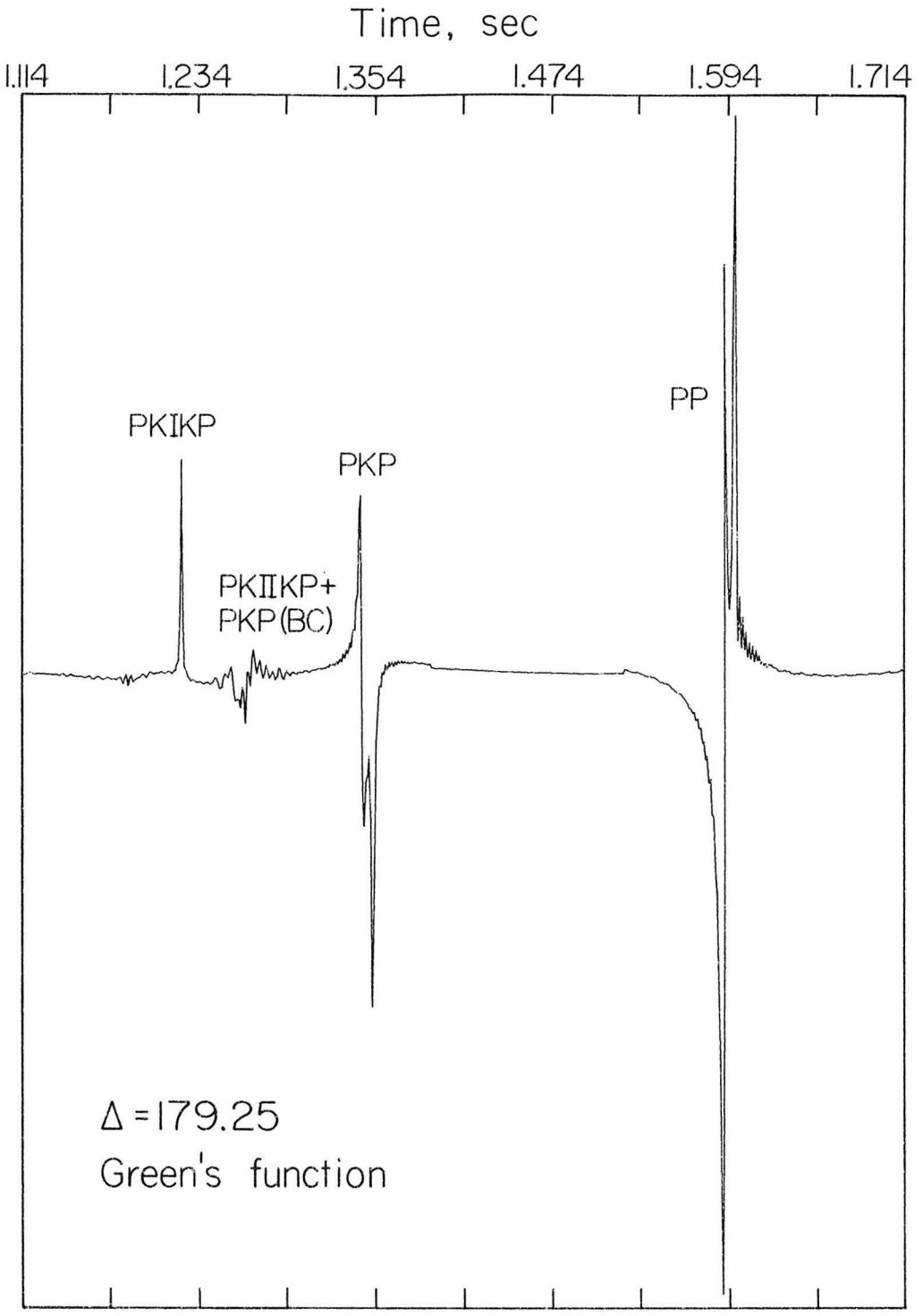

Figure II.10 Detail of Figure II.9 for Δ = 179.25°. Note the phase relationships between rays arriving in opposite directions.

large enough to provide valuable information on the constitution and structure of the inner core–outer core boundary region. Their amplitudes and waveforms are highly sensitive to seismic velocity gradients above and below the top of the inner core, the velocity and density contrasts at the boundary, and the sphericity of the inner core. The study of these phases by themselves and relative to the direct ray PKIKP will constitute a highly rewarding research when seismograms of these phases for highly impulsive earthquake sources or nuclear detonations are recorded at antipodal seismic arrays.

It is instructive to observe in Figures II.9 and II.10 the relative phase shifts of the different waveforms. PKIKP is, as expected, a simple pulse that resembles a Dirac delta function and retains the source original phase. The two PKP arrivals, however, show the waveform distortion produced when the rays touch internal caustics. The first PKP arrival corresponds to the direct ray travelling the shorter path. Its waveform shows a $\pi/2$ phase shift advance relative to the source, as a consequence of its crossing of the caustic near the top of the outer core, a result of the rapid P-wave velocity increase below the core-mantle boundary. The second PKP arrival has crossed the axial caustic before reaching the receiver and therefore shows an extra $\pi/2$ phase advance which results in an inverted version of the direct PKIKP waveform. The same relationship can be observed to exist between the first and second arrivals of PP with an extra phase advance of π, due to the surface bounce. This results in a wave form that is the inverted version of the PKP pair. Since the synthetics in Figure II.9 are computed for a surface source, the focal point of the rays is itself at the surface,

thus at $\theta = 180°$ an extra phase advance of $\pi/4$ occurs for all focused rays (see Appendix C).

Synthetic and Observed Seismograms. In order to be able to compare with the observed seismograms, the Green's functions are convolved with the far-field time function of the Inangahua shock. The event is found to be a sequence of three thrust fault shocks of almost identical fault plane geometry, at depths that vary between 30 km and 10 km. The second event occurs 4 s after the first and the third 20 s after the second shock. Some of its P waveforms are shown in Figure II.11. The source time function is obtained by a procedure entirely similar to that described in Chapter I of this dissertation. Figure II.12 shows that the model satisfactorily reproduces the observed record at PTO. The first arrival is the diffracted P wave around the outer core. This phase is amplified and presents an interesting experimental demonstration of the well known Poisson spot effect predicted by physical optics (Sommerfeld, 1964). Besides this anecdotal feature, the diffracted P wave can be of importance in recovering properties of the average seismic velocity structure near the base of the mantle. Although this wave is predominantly long period, it is sensitive to changes in the P-wave velocity gradient in the neighborhood of the core-mantle boundary. The interference pattern of this phase recorded by an antipodal array would provide an excellent data set to study lateral deviations from homogeneity in the velocity structure by applying simple optical arguments that relate the form, dimensions, and symmetry of Fraunhofer interference patterns to the structure and geometry of the object causing the diffracted field.

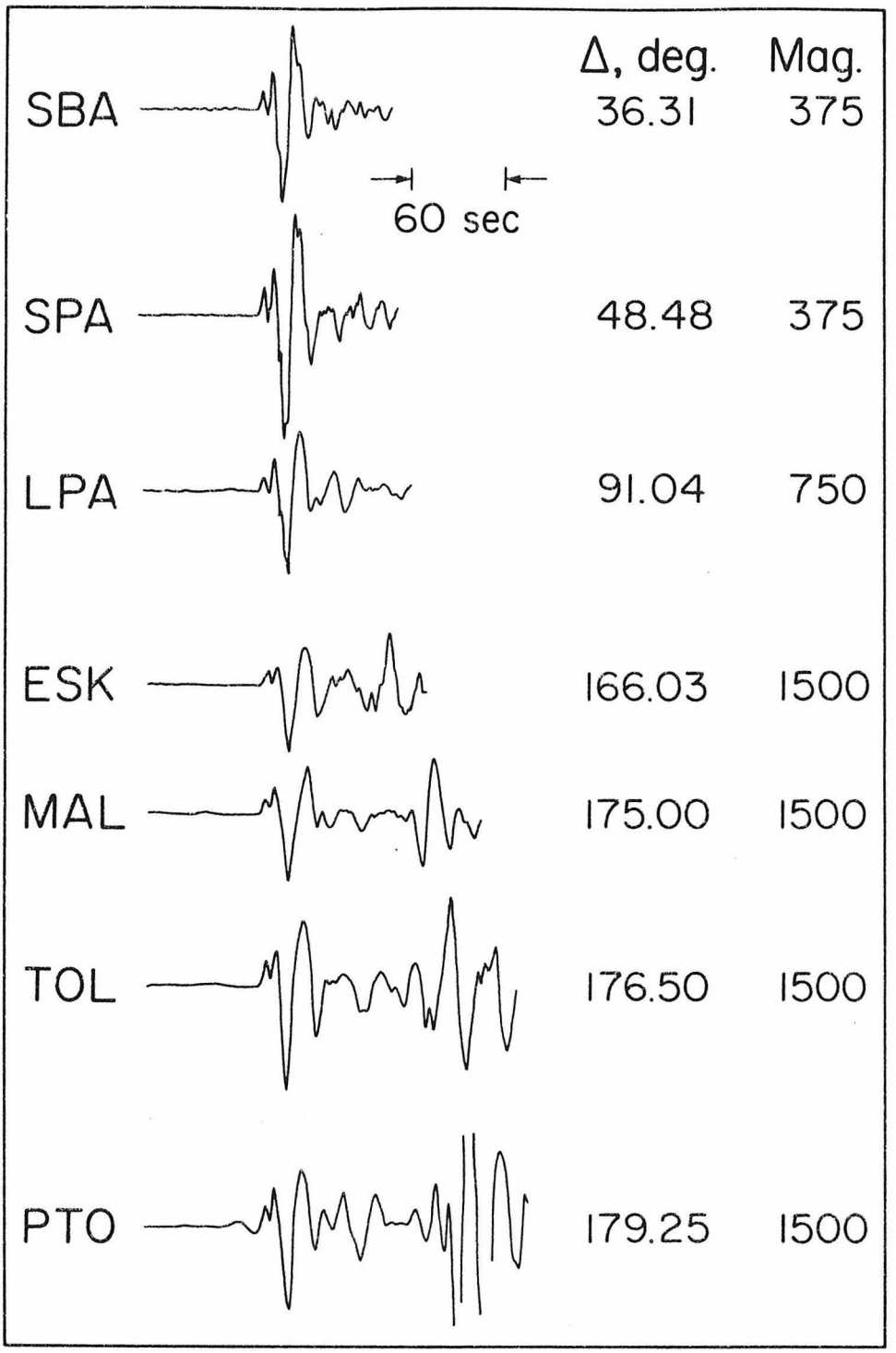

Figure II.11 First arrivals of P waves of the Inangahua earthquake. (WWSSN, long period vertical).

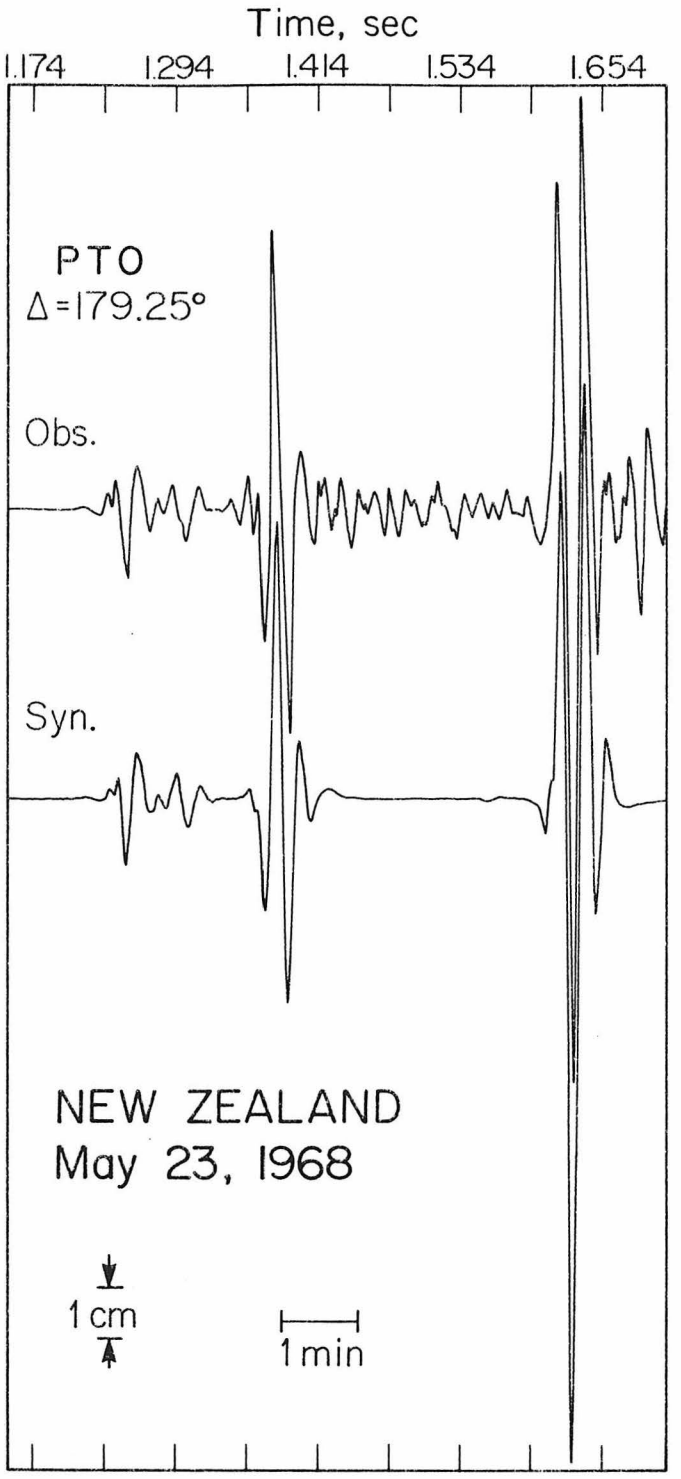

Figure II.12 Comparison of observed and synthetic seismograms at $\Delta = 179.25°$. The synthetic includes P_{diff}, PKIKP, PKIIKP, PKP(BC), PKP and PP.

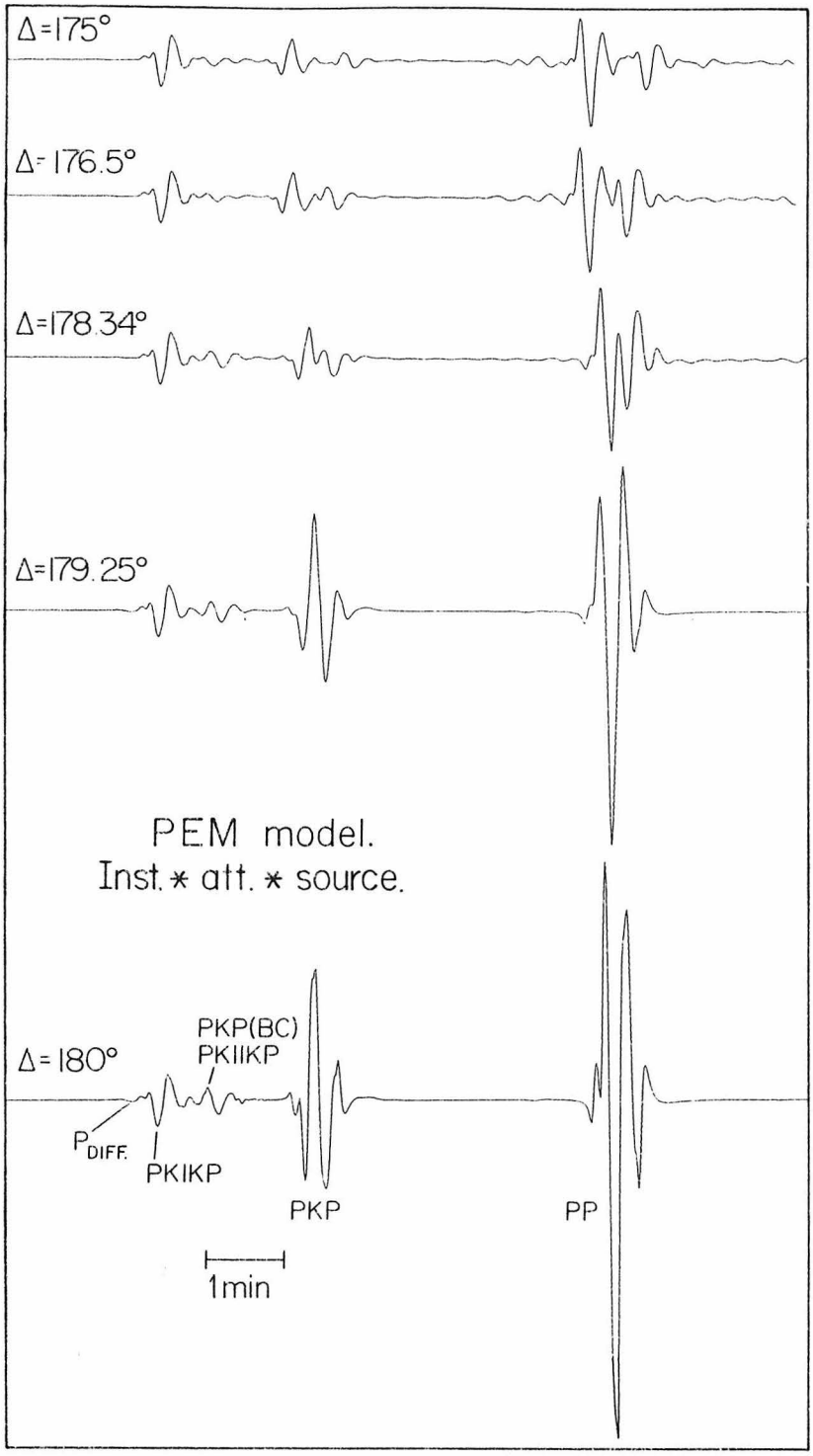

Figure II.13 Synthetic seismograms obtained for various antipodal distances.

Although in Figure II.12 the synthetic seismogram reproduces the $P_{(diff)}$ waveform satisfactorily, its amplitude is less than the observed. We used model PEM in this case and although model 1066B was also tested, it did not improve what is shown. The lack of a more extensive set of data does not allow us to draw any conclusions at this stage.

As seen in the Green's function (Figure II.10) the arrival after PKIKP in the synthetic of Figure II.12 has been generated by the interference of PKIIKP and PKP(BC); this latter phase is the long period diffraction that occurs in the shadow zone of the totally reflected rays off the outer surface of the inner core. In the travel time curves it corresponds to the prolongation of the BC branch of PKP off the tip of the triplication. PKIIKP is generated as a sum of multiply reflected rays at the inner side of the inner core boundary. It is an interference head wave (Červený and Ravindra, 1971), also known as a "whispering gallery" series. The interaction of the PKP(BC) and PKIIKP whose arrival times are similar for most earth models, creates a waveform similar to what is observed. The observed phase is, however, only partially reproduced by the synthetics at 175° and 176.5° (Figure II.14). The identification as PKIIKP + PKP(BC) is at best uncertain. Effects of earth structure near the source cannot be ruled out completely, although it is not evident from our analysis of all recorded seismograms for this event that such interpretation can be given to it.

Two earth models were tested in generating these two phases, PEM (Dziewonski et al., 1975) and 1066B. The first contains a 0.83 km/s jump in P-wave velocity and of 0.6 g/cm^3 in density, and successfully

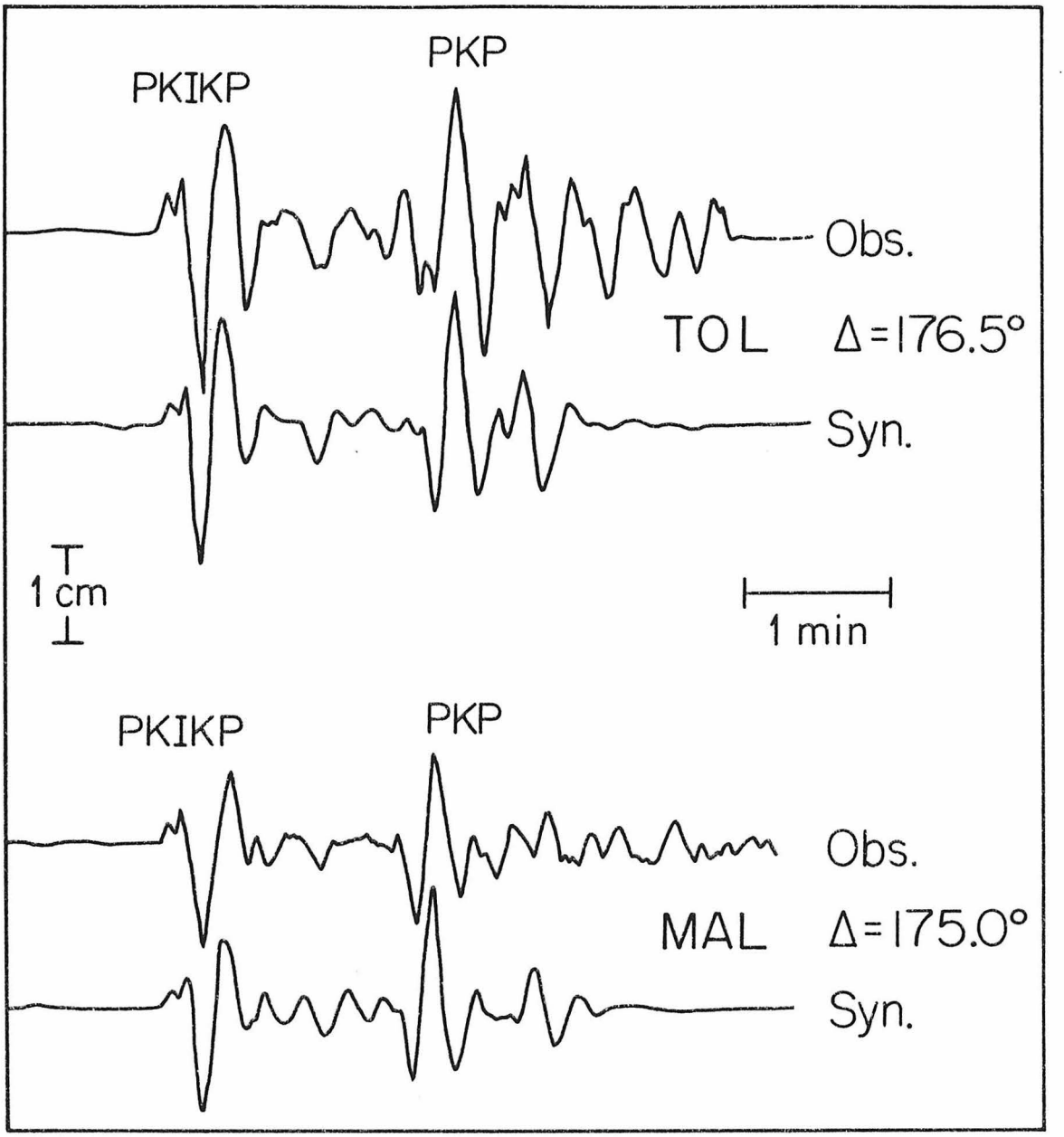

Figure II.14 Comparison of observed and synthetic seismograms at Δ = 175° and 176.5°. Observe the long period coda in the record at TOL, not reproduced by the synthetic.

reproduces the observed. The 1066B model includes discontinuities 20 to 25% less pronounced, and does reproduce the waveforms, but the amplitudes are too small and the amplification develops poorly. This assertion favors an inner core with sharp P and density contrasts as long as our identification of the phases is correct. The motivation, however, is to show that antipodal observations within the time arrival window of PKIIKP can offer conclusive evidence about the structure of the inner core, if known sources are available. Again, it is the highly delicate interference phenomena that occur now between two different seismic waves that reduces the inherent non-uniqueness of the inversion of seismic wave data. The rays PKP and PP are satisfactorily reproduced in waveform, absolute and relative amplitudes for the station PTO at 179.25°. As the predominant periods of both phases are centered near 15 s, it can be concluded that there are no major lateral heterogeneities in the lower mantle and upper core of the earth with characteristic dimensions longer than perhaps 200 km. Otherwise, the interference of PKP and PP could not have been so closely reproduced. Lateral inhomogeneities in the elastic constants with such dimensions would have caused local focusing and/or defocusing of rays resulting in different interference phenomena than those observed. Relative amplitudes between PP and PKP, relative and absolute phase content, and overall waveforms can be easily altered if the individual rays do not converge coherently, as they appear to do judging by the similarity between the observed and the synthetics. At shorter distances (θ = 176.5°, 175°), however, the observed interference cannot be modeled as successfully, mainly because the short and long paths of the rays now interact differently with the

core boundary and thus the interference becomes more complex, and in fact more sensitive to even smaller lateral inhomogeneities. PKP at TOL (θ = 176.5°) shows a long period coda that cannot be reproduced by the synthetics. This effect could be caused by guided seismic energy travelling short paths along the base of the mantle, originated by the ray that travels 183.5° before arriving at the receiver. This ray stays in contact with the core-mantle boundary longer than possibly any other ray. A less pronounced coda can also be observed at MAL (θ = 175°). No evidence of it is clear at PTO. These features do not allow any other conclusion but the reinforcement of the view that antipodal observations using seismic arrays are potentially useful in the investigation of the structure of the core-mantle boundary.

Figure II.15 is shown for close comparison of the observed PKP at 179.25° and the predicted at 180°. From this figure it is seen that there is some precursory energy to PKP that could not be reproduced. The nature of this precursor is not known.

II.5 SURFACE WAVES AT THE ANTIPODE

Introduction. The anaelasticity of the earth's upper mantle controls the amplitude decay of long period surface waves in the period range from 100 to 350 s. If Q is assumed independent of frequency within this range it is possible to obtain an estimate of its value as a function of depth in the mantle from the study of mantle Love and Rayleigh waves by computing the relative amplitude decays of surface wave groups that have travelled a number of times around the earth. If the seismological station is located at the antipode (or at the source) of a large earthquake with an appropriate radiation pattern, multiple

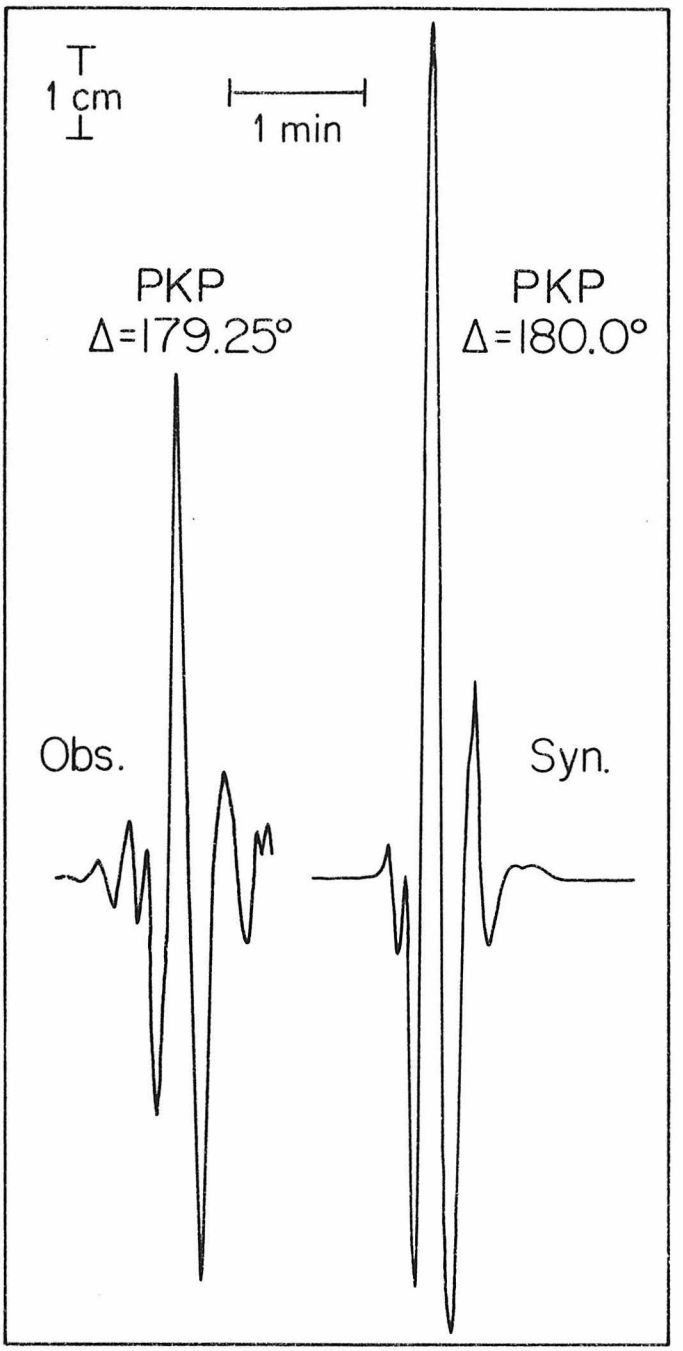

Figure II.15 The phase PKP observed at 179.25° as it would have been recorded at 180°.

arrivals of surface waves can be used to explore large portions of the mantle with a minimum effort. The Inangahua earthquake recorded at PTO (Δ = 179.25°) provides an excellent example of this situation. Figure II.16 shows the locations of the pair epicenter-station for this event and the approximate regions sampled by Rayleigh waves. Information from over half of the earth is focused at the antipode of this event where pairs of Rayleigh wave trains R_1R_2, R_3R_4, R_5R_6, etc. arrive in succession after having travelled 1/2, 3/2, 5/2 times around the earth. The vertical component of these arrivals at a single seismological station is all that is needed to obtain a world average value of Q for Rayleigh waves within a frequency range for which the individual groups can be considered to be at their source's antipode. In the frequency domain, a single surface travelling wave group arriving at a seismological station can be schematically represented by the expression

$$\chi_1 = e^{-ik\theta}\, e^{-\gamma\theta}$$

where k is the wave number, θ the epicentral distance and γ is given by

$$\gamma = \omega/2QU$$

where ω is the angular frequency and U the group velocity. At the antipode, successive wave trains can be represented by

$$e^{-ik(\pi+2n\pi)}\, e^{-\frac{\omega}{2QU}(\pi+2n\pi)}$$

with $n = 1,2,3,\cdots$. By taking the spectral amplitude ratios of two successive groups one obtains

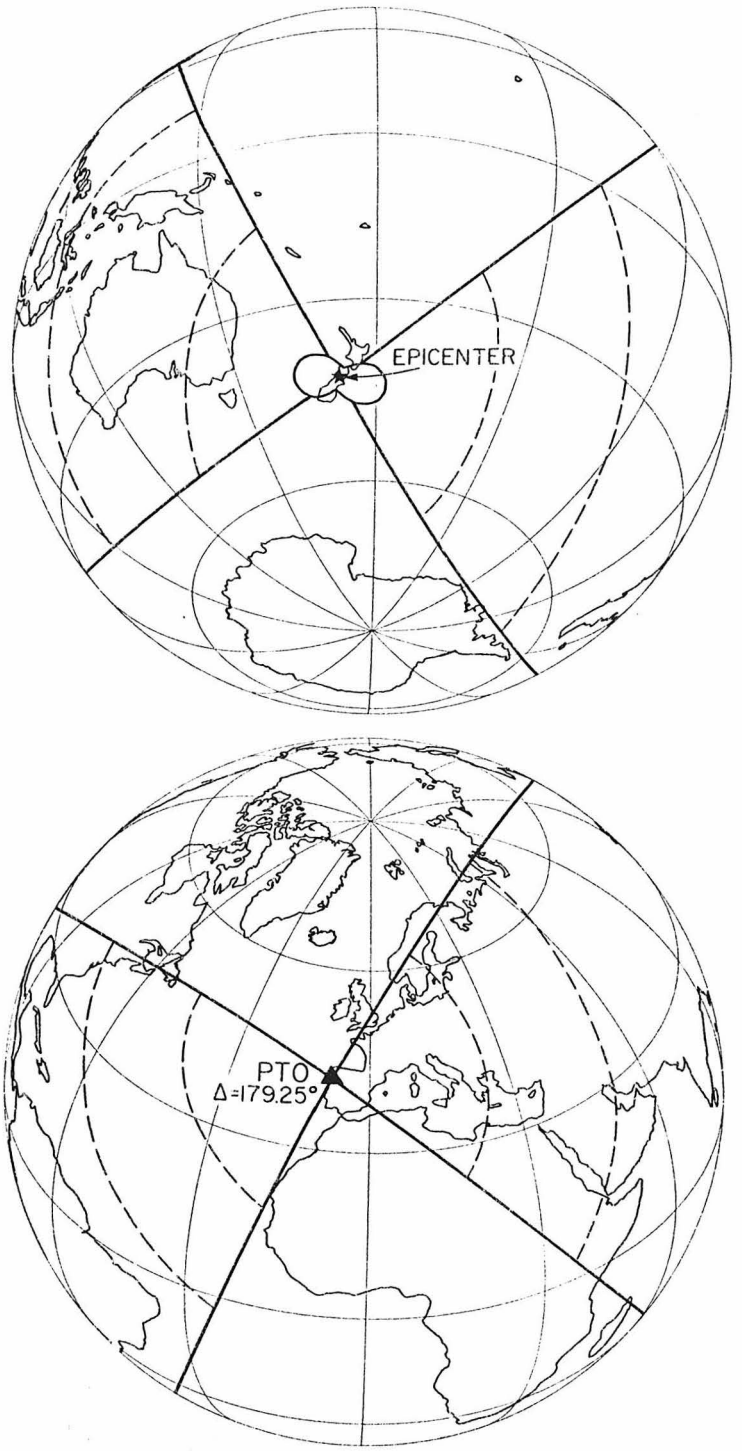

Figure II.16 Global projection of the Rayleigh wave radiation pattern of the Inangahua earthquake. Dashed lines on regions sampled by the waves.

$$\left|\frac{\chi_1(\omega)}{\chi_2(\omega)}\right| = e^{\frac{\omega}{QU}\pi}$$

and thus

$$\log\left|\frac{\chi_1(\omega)}{\chi_2(\omega)}\right| = 2\pi\gamma$$

The R.H.S. of the last expression is obtained experimentally, so that if $U(\omega)$ is known, Q can be determined for each value of ω.

The group velocities were obtained by a bandpass filtering technique (Kanamori, 1970). In this method the group velocity is determined from the arrival time of a wave train on a sharply bandpass filtered record at prescribed frequencies. The results are shown in Figure II.17 and compared to those obtained by Mills and Hales (1977). The comparison with the work of the above mentioned authors is significant, since both results are supposed to represent global averages. The agreement of both results fortifies our belief that the method is viable and potentially useful. Figure II.18 shows the γ values obtained by the spectral ratios of successive wave train arrivals $(R_1R_2)/(R_3R_4)$ and $(R_1R_2)/(R_5R_6)$. The results are stable, showing only minor deviations from a well defined trend. The agreement with Mills and Hales' results is only partial, however, and shows maximum discrepancies for periods less than 200 s. The vertical bars in Mills and Hales' results are an indication of the general scattering of values that is obtained where dissimilar great circle paths are investigated. In our case, however, this circumstance is avoided, and the results represent a time average of the dissipation character of the mantle in the regions depicted in

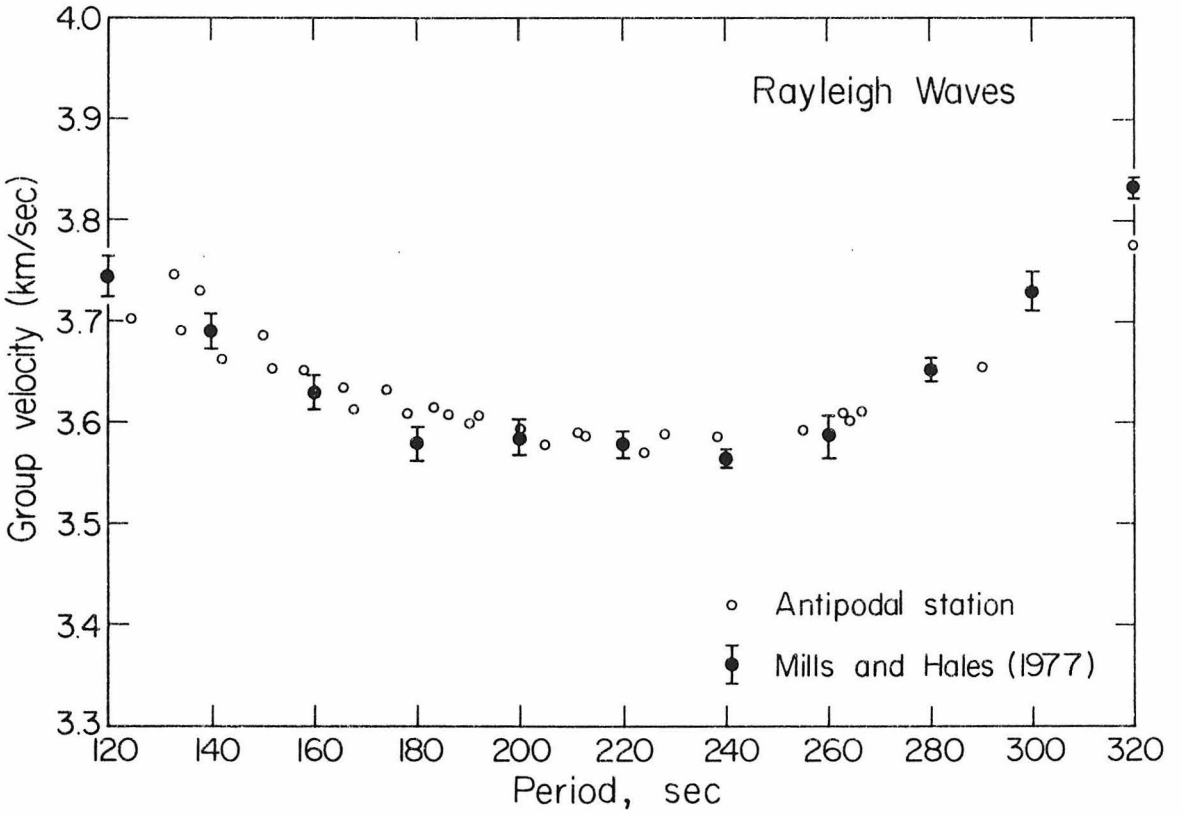

Figure II.17 Dispersion curve for Rayleigh waves obtained by the analysis of a single antipodal record.

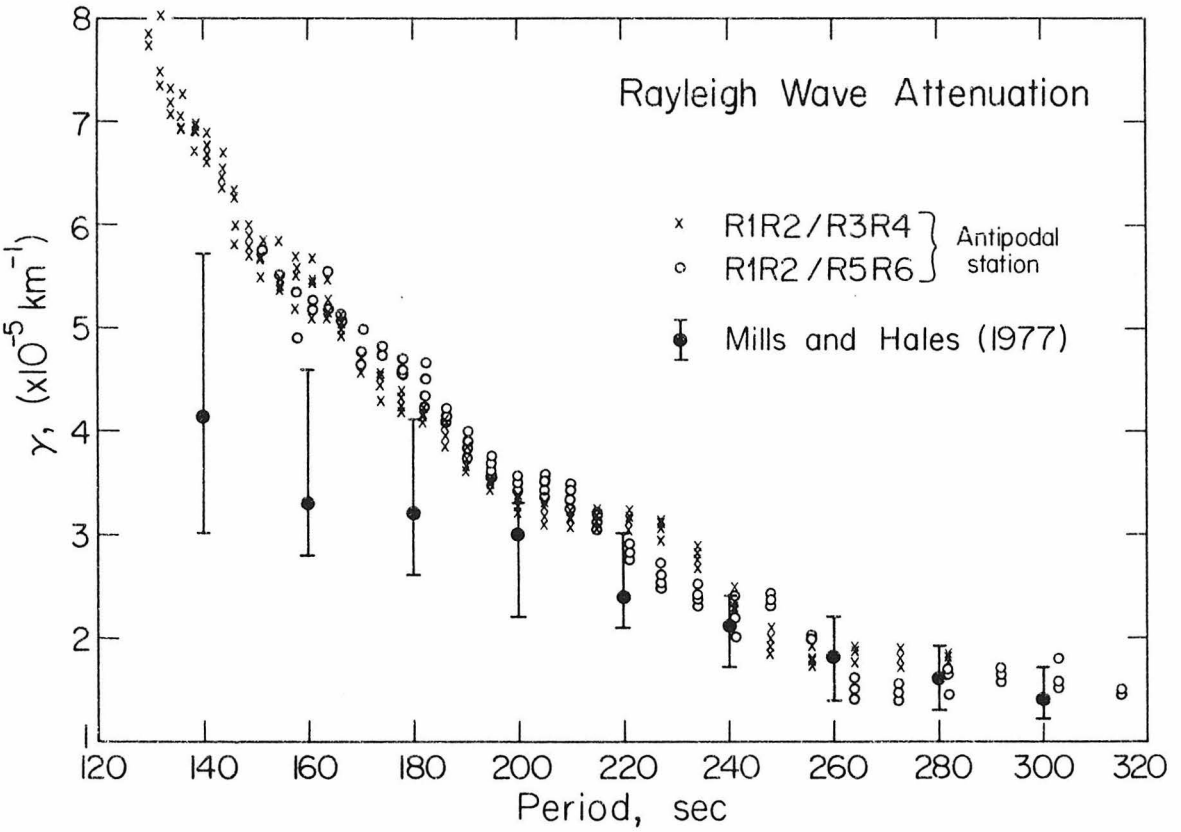

Figure II.18 Values of γ as a function of period obtained by the analysis of a single antipodal record.

Figure II.16. For periods shorter than 200 s our values indicate that attenuation in the upper mantle above 200 km is consistently higher than Mills and Hales' results suggest. The explanation of this discrepancy is clear. Antipodal observations in this case allow us to sample uniformly a region 240° wide around the epicenter, whereas the method of the above mentioned authors samples a region not wider than 140°. This simply implies that the waves arriving at the antipode sample the low velocity layer more extensively in a region of the earth which, as shown in Figure II.16, contains a fair proportion of continental, oceanic and tectonic areas. However, if the effect of lateral inhomogeneities along the wave paths is significant within the frequency band, the results in Figure II.18 might be slightly biased toward low values of Q. No attempt has been made to correct for those effects here, although a preliminary quantification shows that in the worst case they should indeed be minor.

II.6 DISCUSSION AND CONCLUSIONS

Antipodal monitoring of seismic waves provides a global view of the earth's interior concentrated in a very reduced area. The unique ability of antipodal stations to sample an infinity of rays whose paths cover the entire earth laterally allows the investigator to discuss the homogeneity or inhomogeneity of portions of the earth which would otherwise require a large number of observations. The study of these "seismic images" generated at the antipode can be compared to the determination of aberrations of optical lenses by the analysis of the images they produce. At their focal points seismic signals generate delicate interference patterns of Fraunhofer type whose form, extent and regularity

strongly depend on the coherency of the interfering signals. At an antipodal array of seismic stations lateral inhomogeneities associated with a given family of rays will be mapped as deformed, asymmetric interference patterns of anomalous amplitudes, thus providing direct evidence of localized anomalies.

Antipodal observations unfortunately require source-receiver combinations not frequently found. Nevertheless, Fiji-Kermadec and Indonesian earthquake active zones are within antipodal distance from Algeria and Northern South America, where an appropriate density of receivers could offer an excellent prospect. The ideal experiment, designed to collect the maximum amount of rigidly controlled data would require an array of broadband seismometers located within two degrees of the antipode of a large underground nuclear detonation.

Several conclusions, some of preliminary character, can be derived from the results presented in this study. Seismic waves at the antipode of their source are amplified as much as ten times with respect to the normal phase observed two or more degrees away, in agreement with theoretical calculations. Since the signal/noise ratio is enhanced in the same proportion, very weak waves interacting with the inner core like PKIIKP and PKP(BC) are rendered visible. If our identification of inner core phases is correct, the inner core–outer core boundary must be sharply defined, with a P wave velocity contrast of the order of 0.8 km/s. The true structure of the boundary cannot be resolved, however, until appropriate, short-period sources are available. The lower mantle and upper core of the earth are homogeneous laterally as seen by waves as short as 15 s in period. The core-mantle

boundary region, however, is probably laterally inhomogeneous.

In the construction of synthetic seismograms the strong amplification due to the focusing of rays is successfully represented mathematically by the high frequency, uniform asymptotic representation of the Legendre function in terms of Bessel functions of order zero and one. Langer's approximation to the WKBJ solutions of the wave equation successfully quantifies the tunneling effect of long period P waves interacting with the core/mantle boundary.

The analysis of surface Rayleigh waves at a single antipodal station provided a global, stable average of Q values for the upper mantle that indicates higher dissipation between periods of 120 and 200 s than previously thought.

Antipodal observations have a much wider potential use than what could be concluded from an analysis of the results here presented. In fact, perhaps the most exciting prospect of antipodal observations is that they could produce unique constraints on the structure, velocity, and attenuation of the inner core. Previous investigators have studied the inner core from generally weak phases (recorded between 110° and the PKP-B caustic) whose paths interact near critical angle with its surface and do not provide unambiguous results. The inner core can be explored thoroughly from about 155° to the antipode by noting the behavior of PKIKP and the development of the interference between PKIIKP and PKP(BC).

Source parameters of large earthquakes can be constrained by antipodal observations. The direct P arrival of shallow focus events is not

contaminated by converted phases like sP; local heterogeneities near the source affect only marginally rays travelling at zero parameter; near receiver effects are equally minimized and very large first arrivals are indeed smallest at the antipode. These facts suggest that modelling of large earthquakes with complicated source time functions is greatly simplified and possibly less ambiguous at the antipode than anywhere else. Furthermore, it is easy to show that surface waves generated by a point source double couple produce zero amplitude on the horizontal component of an antipodal (or a near-source) receiver, so that any horizontal wave movement that is detected in the long period surface waves must represent the effect of source finiteness.

At this point it is natural to conclude by saying that antipodal observations are simple, economical and powerful enough to be applied to the exploration of planetary interiors when the technology is adequate.

As a common corollary to both chapters of this dissertation, we infer that interference phenomena associated with seismic waves help to decrease the inherent non-uniqueness of certain inversion problems in seismology.

REFERENCES

Abramowitz, M. and I. A. Stegun, Handbook of Mathematical Functions, U.S. National Bureau of Standards, 1965.

Alterman, Z. and D. Loewenthal, Computer generated seismograms, in Methods of Computational Physics, ed. B. Bolt, v. 12, Academic Press, 1972.

Anderson, D. L. and R. S. Hart, Attenuation models of the earth, Phys. Earth. Planet. Int. 16, 289-306, 1978.

Ansell, J. H., On the scattering of SH waves from a point source by a sphere, Geophys. J. Roy. Astr. Soc. 54, 349-387, 1978.

Babich, V. M. and A. S. Alekseyev, A ray method of computing wavefront intensities, Bull. (Izv) Acad. Sci. USSR, Geophys. Ser. no. 1, 9-15, 1958.

Bolt, B. A. and M. E. O'Neill, Times and amplitudes of the phases PKiKP and PKIIKP, Geophys. J. Roy. Astr. Soc. 9, 223-231, 1964.

Born, M. and E. Wolf, Principles of Optics, Pergamon Press, New York, 1959.

Bremmer, H., Terrestrial Radio Waves, Elsevier Pub. Co., 1949.

Brune, J. N., J. E. Nafe, and L. E. Alsop, The polar phase shift of surface waves on a sphere, Bull. Seism. Soc. Am. 51, 247-257, 1961.

Budden, K. G., Radio Waves in the Ionosphere, Cambridge University Press, 1961.

Burridge, R., The reflection of a pulse in a solid sphere, Proc. Roy. Soc. London, series A 276, 367-400, 1963.

Červený, V. and R. Ravindra, Theory of Seismic Head Waves, University of Toronto Press, 1971.

Chapman, C. H., Seismic wave diffraction theory, PhD thesis, University of Cambridge, 1969.

Chekin, B. S., Reflection and refraction of seismic waves at a weak interface, Bull. (Izv.) Acad. Sci. USSR, Geophys. Ser. no. 1, 9-13, 1959.

Choy, G. L. and P. G. Richards, Pulse distortion and Hilbert transformation in multiple reflected and refracted body waves, Bull. Seism. Soc. Am. 65, 55-70, 1975.

Clebsch, A., Über die Reflexion and einer Kugelfläche, Crelle's Journ. für Math B.61, S. 195, 1863.

Copson, E. T., Asymptotic Expansions, Cambridge Tracts in Math. and Math. Phys. No. 55, Cambridge University Press, 1965.

Cormier, V. and P. Richards, Full wave theory applied to a discontinuous velocity increase; The inner core boundary, J. Geophys. 43, 3-31, 1977.

Duwalo, G. and J. A. Jacobs, Effects of a liquid core on the propagation of seismic waves, Can. Journ. Phys. 37, No. 2, 109-128, 1959.

Dziewonski, A. M., A. L. Hales, and E. R. Lapwood, Parametrically simple earth models consistent with geophysical data, Phys. Earth. Planet. Int. 10, 12-48, 1975.

Friedman, B., Propagation in a non-homogeneous atmosphere, in The Theory of Electromagnetic Waves, Morris Kline, ed., Dover Publications, New York, 1951.

Fuchs, K., and G. Muller, Computation of synthetic seismograms with the reflectivity method and comparison with observation, Geophys. J. Roy. Astr. Soc. 23, 417-433, 1971.

Gilbert, F. and D. V. Helmberger, Generalized ray theory for a layered sphere, Geophys. J. Roy. Astr. Soc. 27, 57-80, 1972.

Gutenberg, B. and C. Richter, On seismic waves, Gerlands Beitr. Geophys. 43, 56-133, 1934.

Helmberger, D. V., The crust-mantle transition in the Berling Sea, Bull. Seism. Soc. Am. 58, 179-214, 1968.

Hill, D. P., Phase shift and pulse distortion in body waves due to internal caustics, Bull. Seism. Soc. Am. 64, 1733-1742.

Kanamori, H., Velocity and Q of mantle waves, Phys. Earth. Planet. Int. 2, 259-275, 1970.

Kanamori, H. and J. J. Cipar, Focal process of the great Chilean earthquake, May 22, 1960, Phys. Earth. Planet. Int. 9, 128-136, 1934.

Karal, F. C. and J. B. Keller, Elastic wave propagation in homogeneous and inhomogeneous media, J. Acoust. Soc. Amer. 31, 694-705, 1959.

Langer, R. E., On the asymptotic solutions of ordinary differential equations, with an application to the Bessel functions of large order, Trans. Amer. Math. Soc. 33, 23-64, 1931.

Langer, R. E., On the asymptotic solutions of differential equations, with an application to the Bessel functions of large complex order, Trans. Am. Math. Soc. 34, 447-480, 1932.

Langer, R. E., The asymptotic solutions of ordinary differential equations of the second order, with special reference to the Stokes phenomenon, Bull. Amer. Math. Soc. 40, 545-582, 1934.

Langer, R. E., The asymptotic solutions of ordinary linear differential equations of the second order, with special reference to a turning point, Trans. Amer. Math. Soc. 67, 461-490, 1949.

Langston, C. A. and D. Helmberger, A procedure for modeling shallow dislocation sources, Geophys. J. Roy. Astr. Soc. 42, 117-130, 1975.

Langston, C. A., The February 9, 1971 San Fernando Earthquake: A study of source finiteness in teleseismic body waves, submitted to Bull. Seism. Soc. Am.

Mills, J. M. and A. L. Hales, Great circle Rayleigh wave attenuation and group velocity, Part I: Observations for periods between 150 and 600 s for seven great-circle paths, Phys. Earth Planet. Int. 14, 109-119, 1977.

Nussenzveig, H. M., High-frequency scattering by an impenetrable sphere, Annals of Physics 34, 23-95, 1965.

Olver, F.W.J., "Asymptotics and Special Functions", Academic Press, New York, 1974.

Rayleigh, L., On the propagation of waves through a stratified medium, with special reference to the question of reflection, Proc. Roy. Soc. London, Ser. A 86, 207-226, 1912.

Rial, J. A., The focusing of seismic waves at the epicenter's antipode (abstract), EOS 58, No. 12, 1191, 1977.

Rial, J. A., On the focusing of seismic body waves at the epicenter's antipode, Geophys. J. Roy. Astr. Soc. 55, 1978.

Richards, P. G., "A contribution to the theory of high frequency elastic waves with applications to the shadow boundary of the Earth's core," PhD Thesis, California Institute of Technology, 1970.

Richards, P. G., Calculation of body waves for caustics and tunnelling in core phases, Geophys. J. Roy. Astr. Soc. 35, 243-264, 1973.

Richards, P. G., On the adequacy of plane-wave reflection-transmission coefficients in the analysis of seismic body waves, Bull. Seism. Soc. Am. 66, 701-718, 1976.

Saito, M., Excitation of free oscillations and surface waves by a point source in a vertically heterogeneous earth, J. Geophys. Res. 72, 3689-3699, 1967.

Scholte, J.G.J., On seismic waves in a spherical earth, Meded. Verh. K. ned. Met. Inst. 65, 1-55, 1956.

Sommerfeld, A., "Lectures on Theoretical Physics", Optics, Vol. IV, Academic Press, 1964.

Szegö, Von G., Über einige asymptotische entwickengen der Legendreschen funktionen, Proc. Lond. Math. Soc. Series 2 36, 427-450, 1934.

Van der Pol, B. and H. Bremmer, The diffraction of electromagnetic waves from an electrical source round a finitely conducting sphere, with applications to radiotelegraphy and the theory of the rainbow, Parts I and II, Phil. Mag. 24, 141-190, 825-864, 1937.

Watson, G. N., The diffraction of electric waves by the earth, Proc. Roy. Soc. A95, 83-99, 1918.

Watson, G. N., "A Treatise on the Theory of Bessel Functions", Cambridge University Press, 1966.

APPENDIX A

A point source of irrotational character in an infinite elastic solid is represented by the Green function solution of the Helmholtz equation for the displacement potentials as

$$\phi_{PRIM} = \frac{e^{ik_1R}}{ik_1R} = \sum_{n=0}^{\infty} (2n+1)\, P_n(\cos\theta) \begin{cases} j_n(k_1b)h_n(k_1r) & r > b \\ h_n(k_1b)j_n(k_1r) & r < b \end{cases}$$

where R is the distance from source to receiver along the minimum-time ray, and the expansion in an infinite series using spherical coordinates (r,θ,ϕ) is due to Clebsch (1863), j_n and h_n are spherical Bessel and Hankel functions, respectively, k_1 is the wave number ω/α_1, b is the radius to the source, and θ is the colatitude of the receiver measured from the source axis. α_1 is the P wave velocity in the solid and it is assumed that the source is ϕ-independent.

The secondary field ϕ_s produced by scattering of ϕ_{PRIM} from a fluid sphere of radius a imbedded in the medium and centered at the origin is possibly given by

$$\phi_{sec} = \sum (2n+1)\, a_n h_n(k_1r)\, P_n(\cos\theta) \qquad r > a \qquad (A.1)$$

$$\chi = \sum (2n+1)\, c_n h_n(k_s r)\, P_n(\cos\theta) \qquad (A.2)$$

$$\phi' = \sum (2n+1)\, b_n j_n(k_2 r)\, P_n(\cos\theta) \qquad r < a \qquad (A.3)$$

with $k_2 = \omega/\alpha_2$, α_2 = P-wave velocity in the fluid

$k_s = \omega/\beta$, β = S-wave velocity in the solid

All expressions satisfy radiation conditions at infinity. The boundary conditions at r = a are used to determine the constants a_n, b_n, c_n. We require continuity of normal stresses and displacements and discontinuity of shear stresses. With a time-harmonic factor $e^{-i\omega t}$ we identify $h_n^{(1)}$ with outgoing waves and $h_1^{(2)}$ with incoming waves (from the center of the sphere). The splitting of the scattered field into an infinity of individual optical terms each of which represents a specific geometrical ray is a particular case of the rainbow expansion, the first term of which contains the analogue of the rays P direct and PcP (S and ScS), the second term the PKP (or SKS, PKS or SKP) rays, and subsequent terms contain PK^jP, etc. for $j > 1$.

For the PKP case we proceed as follows: The ingoing elementary spherical wave $h_n^{(2)}(k_1 r)\ P_n(\cos\theta)$ incident at the boundary r = a gives rise to a transmitted wave

$$T_{12}\ h_n^{(2)}(k_1 a)\ \frac{h_n^{(2)}(k_2 r)}{h_n^{(2)}(k_2 a)}\ P_n(\cos\theta)$$

that is, an ingoing wave within the fluid sphere. T_{12} is the optical transmission coefficient equal to $(\phi_n^t/\phi_n^i)_{r=a}$ where the superscripts t and i stand for transmitted and incident wave, respectively. The ratio $h_n^{(2)}(k_1 a)/h_n^{(2)}(k_2 a)$ represents conversion of the wave that now propagates in a different medium. The ingoing elementary wave

$$T_{12}\ \frac{h_n^{(2)}(k_1 a)}{h_n^{(2)}(k_2 a)}\ h_n^{(2)}(k_2 r)\ P_n(\cos\theta)$$

is transformed by "total reflection" at the origin to produce at r = a the outgoing wave

$$T_{12} \frac{h_n^{(2)}(k_1 a)}{h_n^{(2)}(k_2 a)} \; h_n^{(1)}(k_2 r) \; P_n(\cos \theta)$$

and at $r = a$ it is transmitted again through the boundary and becomes

$$T_{12}T_{21} \frac{h_n^{(2)}(k_1 a)}{h_n^{(2)}(k_2 a)} \; \frac{h_n^{(1)}(k_2 a)}{h_n^{(1)}(k_1 a)} \; h_n^{(1)}(k_1 r) \; P_n(\cos \theta) \qquad (A.4)$$

The original incoming potential is given by the sum of elementary waves

$$\sum_{n=0}^{\infty} (n+\tfrac{1}{2}) \; h_n^{(1)}(k_1 b) \; h_n^{(2)}(k_1 r) \; P_n(\cos \theta)$$

so that

$$\phi_{PKP} = \sum_{n=0}^{\infty} (n + \tfrac{1}{2}) \; h_n^{(1)}(k_1 b) \; T_{12}T_{21} \left\{ \frac{h_n^{(2)}(k_1 a)}{h_n^{(2)}(k_2 a)} \right\} \left\{ \frac{h_n^{(1)}(k_2 a)}{h_n^{(1)}(k_1 a)} \right\}$$

$$\times \; h_n^{(1)}(k_1 r) \; P_n(\cos \theta) \qquad (A.5)$$

It is simple to prove that in order to obtain the representations for subsequent terms of this group, PK^jP with $j > 1$, we simply multiply (A.5) by

$$(R_{22})^j \left\{ \frac{h_n^{(1)}(k_2 a)}{h_n^{(2)}(k_2 a)} \right\}^j$$

where R_{22} is the reflection coefficient at the underside of the boundary $r = a$.

Explicit expressions for T_{12}, T_{21}, R_{22} are given by Scholte (1956), Duwalo and Jacobs (1959) among others. The "total reflection" at the origin invoked above stems from the fact that the field within the sphere

must be represented in terms of $j_n(k_2 r)$ functions to avoid the singularity of either $h_n^{(1)}$ or $h_n^{(2)}$ at $r = 0$.

APPENDIX B

The contour C in Figure B.1 can be analyzed as follows. The x's correspond to poles of the integrand in (23). The two series ν_n and ν_n' start near the real axis where $|\nu| = k_1 a$ and $|\nu| = k_2 a$, respectively. The two contours C_3 and C_4 run along the imaginary axis. (However, depending on the behavior of the integrand at $|\nu| \to \infty$, they may be at an angle with the imaginary axis, running symmetric with respect to the origin; see for instance, Ansell, 1978).

From Figure B.1 we see that since $\int_{D_1} = \int_{D_2} = 0$ (Friedman, 1951)

$$\int_{C_1} = -\int_{C_3} + 2\pi i \sum \text{Res } \nu_n$$

$$\int_{C_2} = -\int_{C_4} + 2\pi i \sum \text{Res } \nu_n'$$

Thence

$$\int_C = \int_{C_1} + \int_{C_2} = \int_0^{i\infty} - \int_{C_4} + 2\pi i[\sum \text{Res } \nu_n + \sum \text{Res } \nu_n']$$

$$\int_C = \frac{1}{2i} \int_0^{i\infty} \frac{\nu \, d\nu}{\cos \nu\pi} \, [g(\nu - 1/2) - g(-\nu - 1/2)] P_{\nu - 1/2}(-\cos \theta)$$

$$+ 2\pi i[\sum \text{Res } \nu_n + \sum \text{Res } \nu_n']$$

where we changed ν by $-\nu$ along C_4.

A new contour analysis can be made in order to be able to cross the saddle points of the integrand on the real axis.

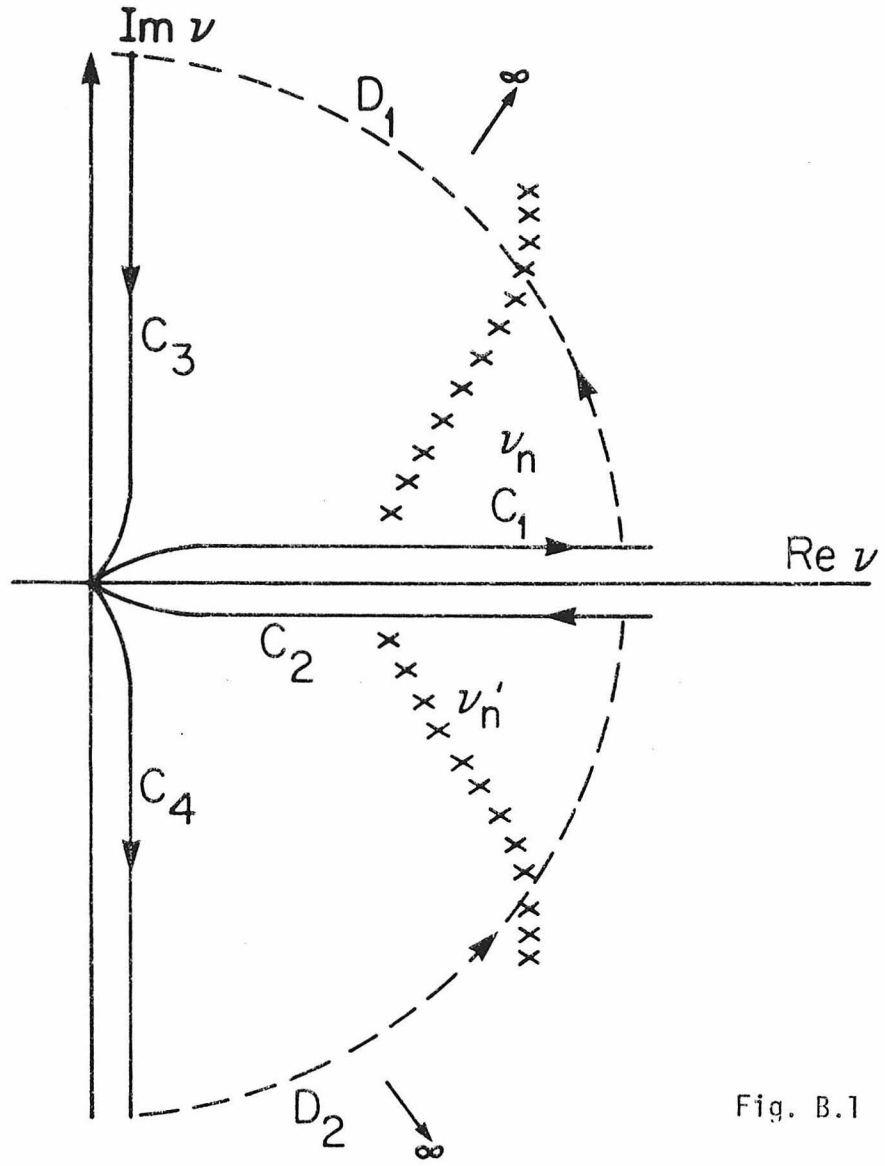

Fig. B.1

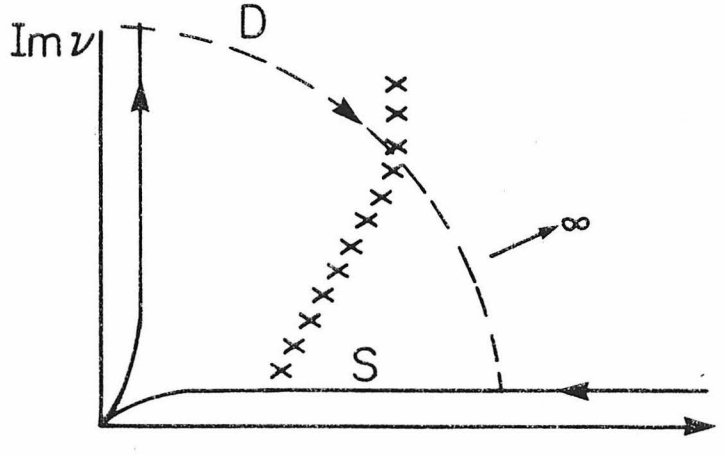

Fig. B.2

From Figure B.2, $\int_M = -\int_S - 2\pi i \sum \hat{\text{Res}}\ \nu_n$, where $\hat{\text{Res}}\ \nu_n$ refer to the residues picked up by the integrand of

$$\frac{1}{2i} \int \frac{\nu\, d\nu}{\cos \nu\pi} [g(\nu - 1/2) - g(-\nu - 1/2)]\, P_{\nu - 1/2}\ (-\cos\ \theta)$$

so

$$\int_C = \frac{1}{2i} \int_0^\infty \frac{\nu\, d\nu}{\cos\ \nu\pi} [g(\nu - 1/2) - g(-\nu - 1/2)]\, P_{\nu - 1/2}(-\cos\ \theta)$$

$$+ 2\pi i[\sum \text{Res}\ \nu_n + \sum \text{Res}\ \nu_n'] - 2\pi i \sum \hat{\text{Res}}\ \nu_n$$

In the inhomogeneous case one can start from the general series solution

$$\phi = \sum_{n=0} (n + \tfrac{1}{2})\, \xi_n^{(1)}(r)[\xi_n^{(1)}(r_s) + \xi_n^{(2)}(r_s)]\, P_n(\cos\ \theta)$$

with

$$\xi_n^{(1)}(r) \sim \frac{e^{\pm i\pi/4}}{\omega r}\ \frac{(\alpha\alpha_s)^{1/2}}{[\ ]^{1/4}}\ e^{\mp i\omega \int_{r_n}^{r} ([\ ]^{1/2}/\alpha)\, dr}$$

$$[\ ] \equiv [1 - \frac{\alpha^2 (n + 1/2)^2}{\omega^2 r^2}]$$

see Richards (1973), and obtain after applying the Watson transform

$$\phi = \frac{1}{i} \int_C \nu\, \xi_{\nu - 1/2}^{(1)}(r)\ f_{\nu - 1/2}(r_s)\ P_{\nu - 1/2}(-\cos\ \theta) \sec \nu\pi\, d\nu$$

with

$$f_{\nu - 1/2}(r_s) = \frac{1}{2} [\xi_{\nu - 1/2}^{(1)}(r_s) + \xi_{\nu - 1/2}^{(2)}(r_s)]$$

The contour C can now be deformed as before and by making the substitution

$$f_{-\nu - 1/2}(r_s) = f_{\nu - 1/2}(r_s)\, e^{-i\pi\nu} + i \sin \nu\pi\, \xi^{(1)}_{\nu - 1/2}(r_s)$$

one finds that the contributions for antipodal rays are given in general by

$$\phi \sim \frac{1}{i} \int_{\Gamma'} \nu\, d\nu\, e^{i\pi\nu}\, \xi^{(1)}_{\nu - 1/2}\, \xi^{(1)}_{\nu - 1/2}(r_s)\, J_0[\nu(\pi - \theta)]$$

from which we easily obtain equation (32).

Typical contours used in the computation of PKP and PKIKP are shown in Figure B.3. The x's represent the string of poles associated with the core-mantle boundary.

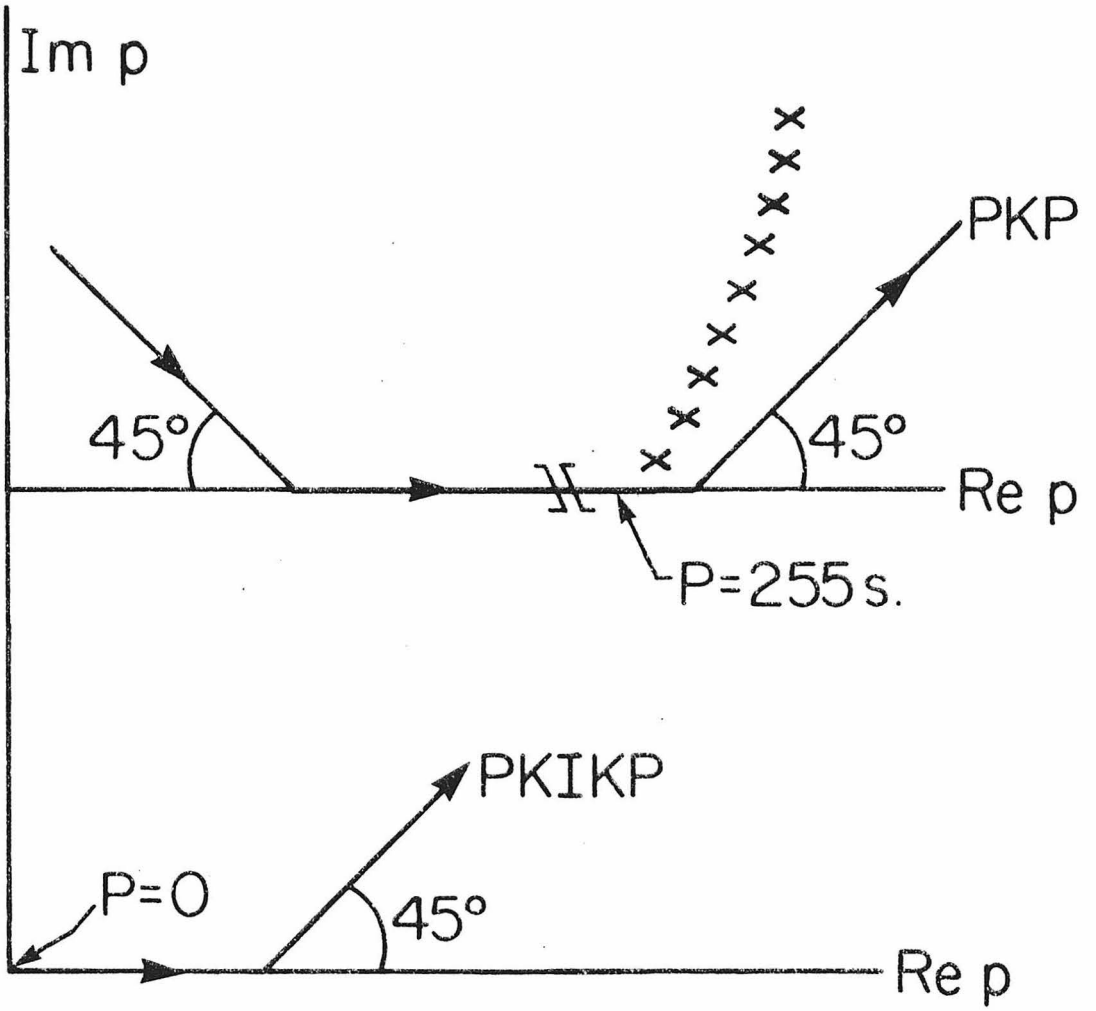

Figure B.3 Typical complex contours used in the computations. p is the complex ray parameter.

APPENDIX C - The phase shift at the antipode

Brune et al (1961) have shown how waves propagating over the surface of a sphere undergo a phase shift of $\pm\pi/2$ for every crossing of the antipode or the source regions. This argument can be used in an analogous manner for body waves that converge to the antipodal region of a sphere because they also display cylindrical symmetry and the axial caustic is a line, not a point. In Figure C.1 this situation is illustrated by using generic rays which approach the antipode of a homogeneous sphere. We arbitrarily select the phase of the least time ray as being zero (paths S) so that those rays that arrive along the longer paths L have crossed the axial caustic and suffered a $\pi/2$ phase shift that distorts the wave form as shown in points C (Hill, 1974). When the antipode A is approached the interference of the rays is seen to amplify the upswing part of the signal that results in the wave form A, whose phase shift with respect to the incident pulse S is now only $\pi/4$. Thus, at the antipode itself the phase of the pulse is $\pi/4$ shifted with respect to the first (least time) arriving pulse. This situation is seen to occur for PKP and PP waves in Figure II.9. There, the first arrival (S) of PKP is a Hilbert transform of the original phase. At the antipode the phase of PKP is then $\frac{\pi}{2} + \frac{\pi}{4} = \frac{3\pi}{4}$. Similarly, since the phase of the first PP arrival is $3\pi/2$, its phase at the antipode is $\frac{3\pi}{2} + \frac{\pi}{4} = \pi + \frac{3\pi}{4}$.

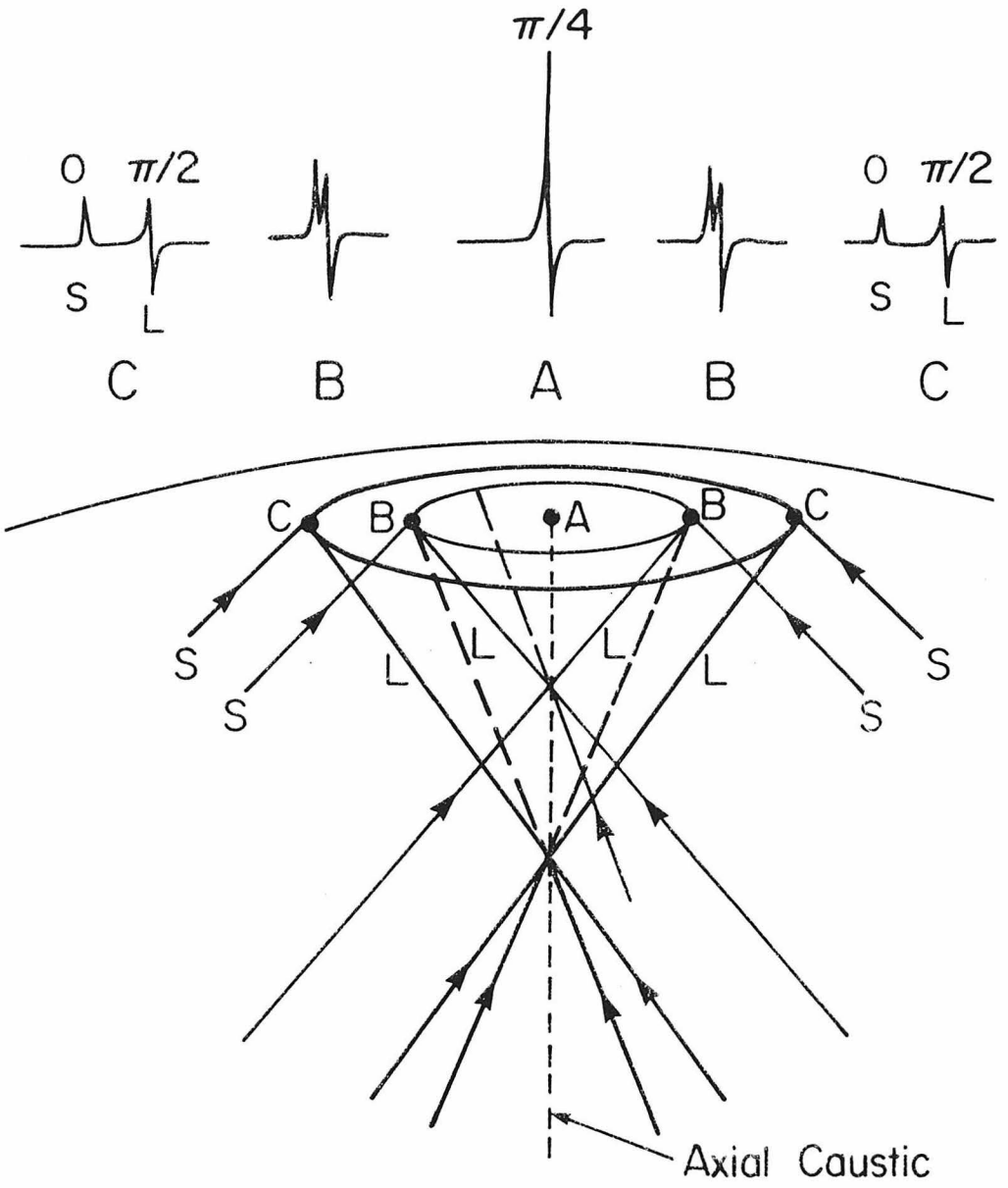

Pulse Distortion

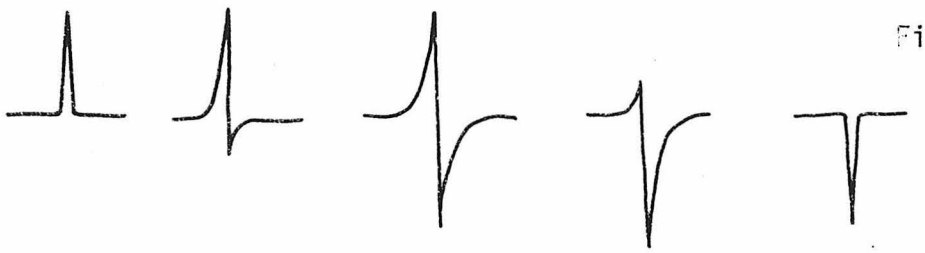

Phase 0 π/4 π/2 3π/4 π

Fig. C.1